Hierarchical reconstruction of 3D well-connected porous media from 2D exemplars using statistics-informed neural network

Jinlong Fu[a], Min Wang[b,*], Dunhui Xiao[c], Shan Zhong[a], Xiangyun Ge[a], Minglu Wu[d], Ben Evans[a]

[a]*Zienkiewicz Centre for Computational Engineering, Faculty of Science and Engineering, Swansea University, Swansea SA1 8EN, UK*
[b]*Fluid Dynamics and Solid Mechanics Group, Theoretical Division, Los Alamos National Laboratory, Los Alamos, NM 87545, USA*
[c]*School of Mathematical Sciences, Tongji University, Shanghai 200092, China*
[d]*Research Centre of Multiphase Flow in Porous Media, China University of Petroleum (East China), Qingdao 266580, China*

Abstract

The relationships between porous microstructures and transport properties are of fundamental importance in various scientific and engineering applications. Due to the intricacy, stochasticity and heterogeneity of porous media, reliable characterization and modelling of transport properties often require a complete dataset of internal microstructure samples. However, it is often an unbearable cost to acquire sufficient 3D digital microstructures by purely using microscopic imaging systems. This paper presents a machine learning-based technique to hierarchically reconstruct 3D well-connected porous microstructures from one isotropic or several anisotropic low-cost 2D exemplar(s). To compactly characterize the large-scale microstructural features, a Gaussian image pyramid is built for each 2D exemplar. Local morphology patterns are collected from the Gaussian image pyramids, and then they serve as the training data to embed the 2D morphological statistics into feed-forward neural networks at multiple length levels. By using a specially-developed morphology integration scheme, the 3D morphological statistics at different levels can be inferred from the statistics-informed neural networks. Gibbs sampling is adopted to hierarchically reconstruct 3D microstructures by using multi-level 3D morphological statistics, where the large-scale, regional and local morphological patterns are statistically generated and successively added to the same 3D random field. The proposed method is tested on a series of porous media with distinct morphologies, and the statistical equivalence between the reconstructed and the real microstructures is systematically evaluated by comparing morphological descriptors and transport properties. The results demonstrate that the proposed 2D-to-3D microstructure reconstruction method is a universal and efficient approach to generating morphologically and physically realistic samples of porous media.

Keywords: Porous microstructure; Hierarchical reconstruction; Statistics-informed neural network; Long-distance correlation; Transport property; Small data.

1. Introduction

Stochastic porous media are ubiquitously encountered in various disciplines of science and engineering [1, 2, 3, 4, 5], and typical examples are rocks, soils, concretes, membranes, electrodes, catalysts and biological tissues. Consisting of the solid skeletal frame and the void space, porous media usually possess complicated internal microstructures. It has been generally recognized that the geometry and topology of porous microstructures fundamentally govern the macroscopic behaviour, performance and properties [6, 7]. There are various types of transport phenomena occurring inside porous media, such as fluid permeation, mass diffusion, electricity transmission and heat conduction. And they all rely heavily on the configurations of pore network systems, which essentially determines corresponding transport properties including permeability [8], effective diffusivity [9], electrical conductance [10] and thermal conductivity [11].

Pore-scale imaging and modeling [12, 13, 14, 15, 16] have been developed to be a key combined technique to study structure-property relationships of porous media in a non-destructive manner. Advanced microscopic imaging techniques, such as X-ray micro-computed tomography (micro-CT) or the scanning electron microscope (SEM), are used to obtain 3D or 2D digital microstructures from physical porous media samples. Numerical

*Corresponding author
Email address: sacewangmin@gmail.com (Min Wang)

modelling can then be performed on them to simulate physical phenomena at the pore-scale, thereby evaluating the physical properties.

However, macroscopic properties of a certain porous medium can fluctuate dramatically and exhibit strong uncertainty, due to the intricacy, stochasticity and heterogeneity of porous microstructures [6, 7, 17]. Investigation of the microstructure-property linkages can be considered as a statistical learning problem, which requires a complete computational dataset that is far beyond a single porous microstructure sample. Generally, this complete computational dataset should account for the representative volume elements (RVEs) or the statistical volume elements (SVEs) with all possible configurations [18]. But it is often impractical to acquire a large number of 3D digital microstructure samples by purely using microscopic imaging techniques. On the one hand, physical samples of natural porous media (such as rock cores) are usually not easy to obtain; on the other hand, volumetric imaging systems are still technically demanding, time-consuming, and cost-intensive.

Stochastic microstructure reconstruction [18, 19, 20, 21, 22, 23, 24] provides an effective and economical way to generate numerous virtual samples with certain microstructural characteristics varying systematically. These virtual samples share some common statistical features (such as porosity, tortuosity, pore-throat size distribution, coordination number, spatial correlation function, etc.), composing a computational dataset to capture the inherent stochasticity of porous media. Besides, compared with 3D microscopy imaging, it is much cheaper and easier to acquire high-quality 2D images of representative area elements (RAEs) using surface imaging devices. A 2D-to-3D microstructure reconstruction method that can infer and synthesize 3D microstructures from the available 2D cross-sectional images by preserving statistical equivalence is very attractive [19, 20]. Roughly, stochastic microstructure reconstruction can be divided into two categories [24]: *Equidimensional reconstruction* and *Dimensionally-upgraded reconstruction*, as illustrated in Figure 1.

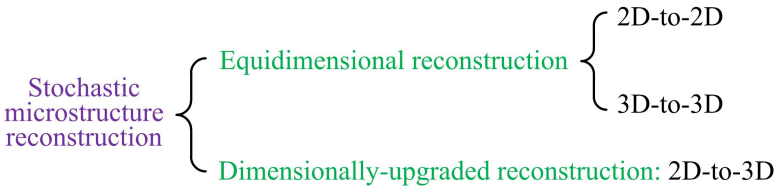

Figure 1: Categories of stochastic microstructure reconstruction.

Dimensionally-upgraded reconstruction of porous microstructures is the special focus of this study. Stochastic optimization-based reconstruction (SOR) [19, 25, 26] and Gaussian random field transformation (GRFT) [20, 27] are the typical representatives of traditional 2D-to-3D reconstruction methods. SOR is flexible in choosing the optimization objectives, which allows users to freely determine the microstructural characteristics to be preserved in the reconstructed microstructures. However, the iterative optimization procedure makes SOR extremely time-consuming and computation-intensive. GRFT treats a porous microstructure as a Gaussian random field, and it reconstructs 3D samples by truncating manually generated random fields. Although GRFT possesses a high reconstruction efficiency, it can only capture the low-order statistical information of random microstructures. Other reconstruction methods, such as process-based method [28], multiple-point statistics method [29, 30], Markov Chain Monte Carlo simulation [31], patch-based method [32], texture synthesis method [33], descriptor-based methodology [34] and packing algorithm [35] are frequently used in some specific fields. But these methods can rarely provide a universal way to rapidly generate 3D well-connected porous microstructures when pore geometry information is limited to 2D thin sections.

Recently, various types of machine/deep learning algorithms have been applied to stochastically reconstruct 3D random microstructures from 2D thin sections, such as support vector machine [36], convolutional neural network (CNN) [37], generative adversarial network (GAN) [38, 39], transfer learning [40], feed-forward neural network [24], hybrid deep learning [41], variational auto-encoder (VAE) [42], and recurrent neural network (RNN) [43]. These machine/deep learning-based reconstruction methods usually pay much attention to capturing and preserving morphological details of random microstructures, therefore, they are usually powerful in generating morphologically-similar microstructure samples. However, few of these methods pay special attention to the large-range microstructural metrics of porous media. Many deep learning-based reconstruction methods (including CNN [37], GAN [38, 39], transfer learning [40] with pretrained CNN, hybrid deep learning [41], VAE [42] and RNN [43]) use convolutional layers to characterize microstructures and then form the feature maps that summarize the presence of detected features. The kernels (convolution windows) used to extract local features are usually of small size (such as 3×3 or 5×5), which may not be large enough to capture the internal connections

and the relative spatial relationships between components. It is still not clear how many large-sized features beyond the kernel's range are considered during the processes of microstructure characterization and reconstruction. In recent studies [21, 22, 24], decision tree (DT) and feed-forward neural network (FNN) have been incorporated into statistical characterization and stochastic reconstruction of random microstructures, and these methods exhibit excellent performance to reproduce morphologically-similar microstructure samples. Due to the adoption of the Markov random field (MRF) assumption [21, 22, 24] to model random microstructures, these methods also have limitations in capturing large-sized microstructural features, although the scopes of MRF can be set with large sizes. Furthermore, global microstructural characteristics (such as long-distance connectivity, large-range correlation, and topological information) also pose a huge challenge for the convolution window-based or MRF-based feature extraction to completely cover them.

Generally, stochastic reconstruction of porous microstructures should pay special attention to long-distance connectivity and large-range correlations [28, 29], because transport properties are primarily dominated by the global percolation of porous media [6, 12, 44]. In this study, a hierarchical strategy is used to overcome the inherent limitations of MRF-based characterization/reconstruction [21, 22, 24] in capturing/preserving large-range microstructural metrics. Its basic idea is to hierarchically characterize local, regional and large- range microstructural metrics by separately training multiple sets of FNN models, based on which the morphology patterns at different scales are stochastically reproduced through a multi-level reconstruction approach. To demonstrate the effectiveness of this hierarchical strategy, it is initially applied to 2D-to-2D reconstruction for random microstructures with long-distance correlations, and the results are compared with that of the decision tree-based method [21]. As shown in Figure 2, the hierarchically reconstructed microstructures satisfactorily preserve the large-range correlations and long-distance connectivity existing in the original microstructures, while the reconstructed microstructures from the decision tree-based method failed to maintain the large-sized features exceeding the scope of MRF. Besides, this hierarchical strategy has already been applied to 3D-to-3D microstructure reconstruction in our previous study [18], and it also exhibits great advantages over the decision tree-based method [22] in capturing and maintaining long-distance connectivity and transport properties of porous media.

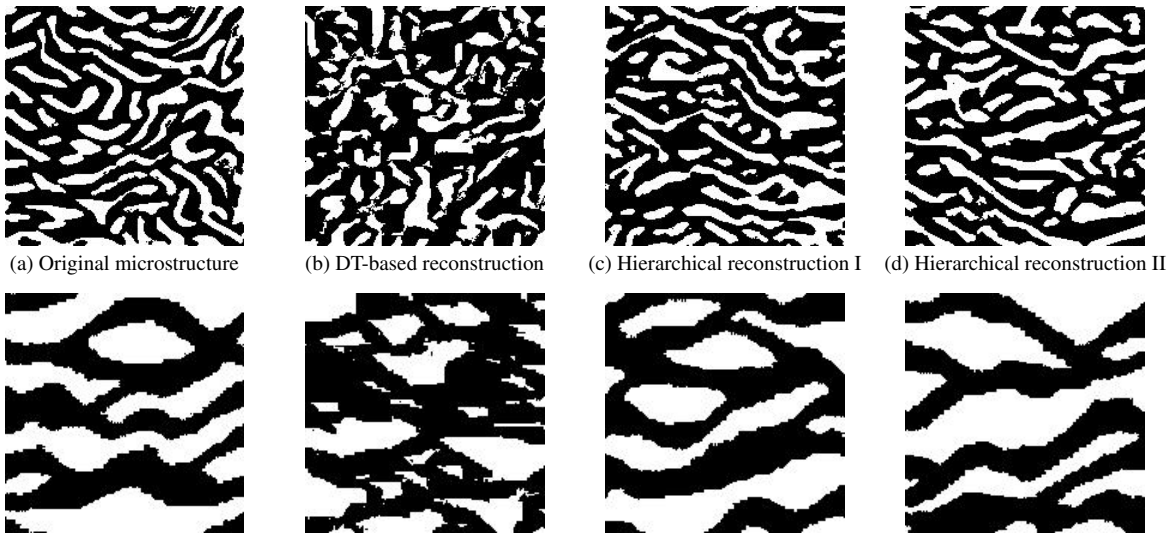

(a) Original microstructure (b) DT-based reconstruction (c) Hierarchical reconstruction I (d) Hierarchical reconstruction II

(e) Original microstructure (f) DT-based reconstruction (g) Hierarchical reconstruction I (f) Hierarchical reconstruction II

Figure 2: Comparison between the decision tree-based (DT-based) method and the proposed hierarchical method, to highlight the effectiveness of the latter in capturing and preserving large-range correlations and long-distance connectivity.

Following this hierarchical strategy, a machine learning-based technique is specially developed for 2D-to-3D microstructure reconstruction in this work, aiming to stochastically generate 3D well-connected porous microstructures of arbitrary sizes from one (isotropic) or several (anisotropic) low-cost 2D exemplar(s). The proposed 2D-to-3D reconstruction method distinguishes itself from existing methods in the following aspects: (1) It is biased toward the large-range correlations and long-distance connectivity of porous microstructures, by developing a hierarchical characterization approach and a multi-level reconstruction approach; (2) Local, regional and large-scale microstructural metrics are hierarchically captured and statistically characterized by training a set of feed-forward neural networks; (3) Training a feed-forward neural network model only requires one or several 2D exemplar(s) with representative significance to serve as the training image(s); (4) The 2D morphological statistics

at different scales are embedded in the feed-forward neural networks, and they are of good interpretability and referred to as *statistics-informed neural networks (SINNs)*; (5) A morphology integration scheme is developed to derive 3D morphological statistics from the 2D morphological statistics embedded in SINNs; (6) Large-scale, regional and local morphology patterns are statistically generated and successively added to the same 3D random field via Gibbs sampling; (7) The reconstruction procedure is highly efficient, and the balance between reconstruction speed and memory requirement can be made by adjusting the sampling ratio; (8) Various morphological descriptors are used to quantify the long-distance connectivity and large-range correlations of reconstructed microstructures, and different transport properties are numerically evaluated to verify the physical equivalence.

The remainder of this paper is organized as follows: Section 2 explains the novel methodology to statistically characterize the 2D cross-sectional image(s) of porous media by training *statistics-informed neural network (SINN)* models at multiple length levels; Section 3 describes the hierarchical procedure to reconstruct 3D porous microstructures by using the 3D morphological statistics derived from the trained SINN models; In Section 4, the proposed method is tested on a series of porous media with distinctive morphologies, and the microstructure reconstruction results are compared with that of the GAN-based reconstruction method [39], where various morphological descriptors are used to quantitatively assess microstructure reconstruction quality; In Section 5, transport properties of the reconstructed and the real microstructures are numerically computed to further evaluate the physical equivalence between them; Section 6 discusses the strengths and weaknesses of the proposed method, and the main contributions of this study are briefly summarized as well.

2. Statistical microstructure characterization

After acquiring 2D thin sections from microscopic imaging systems, image segmentation is performed on them to separate the pore space from the solid skeleton, allowing subsequent studies including microstructural analysis and pore-scale simulation, as illustrated in Figure 3. As shown in Figure 3c, porous microstructures usually exhibit great disorder and strong randomness, and thus statistical characterization of the 2D planar sections is the first key step to constructing equivalent 3D microstructure samples.

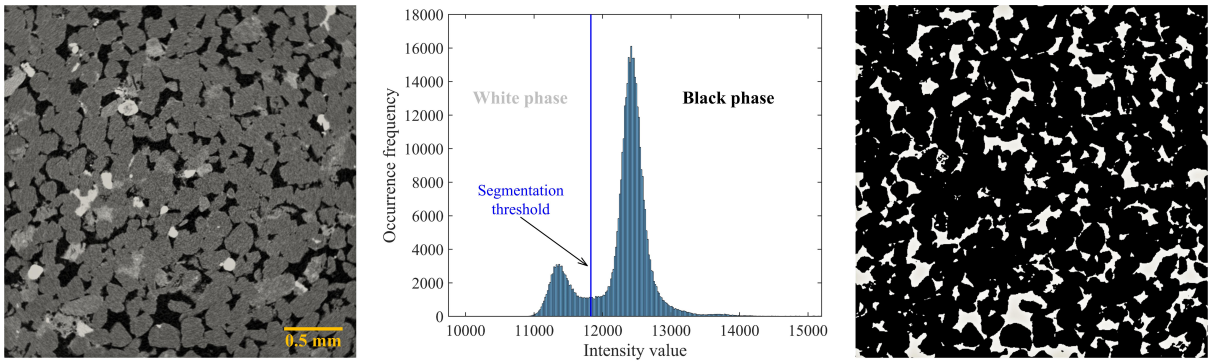

(a) (b) (c)

Figure 3: Illustration of image segmentation: (a) A 2D slice of the micro-CT image of a Berea sandstone sample, where the pore space is shown in dark; (b) The histogram of pixel intensity values, based on which the segmentation threshold is determined; and (c) The binary image with two distinct phases, where the white phase denotes the pore space and the black phase represents the solid matrix.

Consider a 2D regular lattice of size $l \times w$, in which each site (i, j) is associated with a random variable $X_{ij} \in \mathbb{Q}$, forming a random field $\boldsymbol{X}$, given by:

$$\boldsymbol{X} = \{X_{ij} : 1 \leq i \leq l,\ 1 \leq j \leq w\} \tag{1}$$

where $i \in \mathbb{Z}^+$ and $j \in \mathbb{Z}^+$ are the indexes of rows and columns. Filling a pixel value X_{ij} into each site (i, j) of this 2D lattice yields a 2D digital image $\boldsymbol{X}$. Generally, a 2D digital microstructure $\boldsymbol{X}$ in the binary format (as shown in Figure 3c) can be represented by the indicator function as follows:

$$X_{ij} = \begin{cases} 1, & \text{if } (i, j) \text{ is located at pore space (white phase);} \\ 0, & \text{if } (i, j) \text{ is located at solid matrix (black phase).} \end{cases} \tag{2}$$

2.1. Markov random field

Here, a digital microstructure $\boldsymbol{X}$ is assumed as a realization of a particular random process. Since the pixel variables at different sites are statistically dependent, the full joint probability distribution function (PDF) of pixel variables is an ideal statistical model to characterize $\boldsymbol{X}$. The full joint PDF, denoted by $Pr(\boldsymbol{X})$ or $Pr(X_{11}, X_{12}, ..., X_{ij}, ...)$, represents the probability that an image $\boldsymbol{X}$ is assigned with a certain configuration of all pixel values. Without knowing any prior knowledge, deriving the full joint PDF $Pr(\boldsymbol{X})$ requires enumerating all possible configurations of pixel variables. Such a task is fiendishly intractable because of the extremely high dimensionality ($W \times L$) of pixel variables. In this study, the Markov random field (MRF) theory [45] is adopted to reduce the complexity of image modelling problems. Essentially, MRF treats a digital microstructure as a realization sampling from the underlying full joint PDF. The major advantage of MRF is that it allows for deriving a global microstructure description by specifying the local statistical characteristics.

Let $\boldsymbol{N}_{ij}$ represent a set of pixels adjacent to a central pixel X_{ij} within a certain range, a 2D digital microstructure $\boldsymbol{X}$ can be considered to be a Markov random field, if the following relation holds for each pixel X_{ij}:

$$Pr\left(X_{ij}\middle|\boldsymbol{X}^{(-ij)}\right) = Pr\left(X_{ij}\middle|\boldsymbol{N}_{ij}\right) \tag{3}$$

where $\boldsymbol{X}^{(-ij)}$ denotes the remaining pixels in the 2D image $\boldsymbol{X}$ excluding X_{ij}. This condition is called the *Markov property*, and it indicates that the pixel value at any site is only dependent on its neighborhood within a certain range. Compared to the full joint PDF $Pr(\boldsymbol{X})$ or $Pr(X_{11}, X_{12}, ..., X_{ij}, ...)$, the conditional probability distribution function (CPDF) $Pr\left(X_{ij}\middle|\boldsymbol{N}_{ij}\right)$ has a much lower dimensionality of pixel variables, allowing the derivation of $Pr\left(X_{ij}\middle|\boldsymbol{N}_{ij}\right)$ through enumerating all possible configurations.

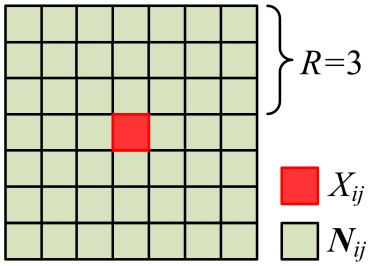

Figure 4: The square-shaped data template to model local statistical characteristics of an image $\boldsymbol{X}$ (X_{ij} denotes a central pixel, N_{ij} denotes the neighboring pixels, and the radius R is used to measure the neighborhood range).

To model the local statistical characteristics of a digital microstructure, the first step is to specify the geometry of the neighborhood region. As illustrated in Figure 4, the dependence between a central pixel and its neighboring pixels is considered within a square-shaped region measured by its radius R, and this square-shaped region is called a data template. The data template DT can be used to scan the digital image $\boldsymbol{X}$ to collect local morphology patterns for the derivation of $Pr\left(X_{ij}\middle|\boldsymbol{N}_{ij}\right)$, as illustrated in Figure 6. Here, the observation of a local morphology pattern $(X_{ij}, \boldsymbol{N}_{ij})$ is called as a data event, and the CPDF $Pr\left(X_{ij}\middle|\boldsymbol{N}_{ij}\right)$ can be estimated from the occurrence frequencies as follows:

$$Pr(X_{ij}, \boldsymbol{N}_{ij}) = \frac{O(X_{ij}, \boldsymbol{N}_{ij})}{\sum_i \sum_j O(X_{ij}, \boldsymbol{N}_{ij})} = \frac{O(X_{ij}, \boldsymbol{N}_{ij})}{O_{\text{all}}} \tag{4}$$

$$Pr\left(\boldsymbol{N}_{ij}\right) = \frac{O(\boldsymbol{N}_{ij})}{\sum_i \sum_j O(\boldsymbol{N}_{ij})} = \frac{O(\boldsymbol{N}_{ij})}{O_{\text{all}}} \tag{5}$$

where $O(X_{ij}, \boldsymbol{N}_{ij})$ and $O(\boldsymbol{N}_{ij})$ are the occurrence times of the data events $(X_{ij}, \boldsymbol{N}_{ij})$ and $(\boldsymbol{N}_{ij})$ respectively, and O_{all} denotes the total number of all data events.

The core of statistical microstructure characterization is to determine the CPDF $Pr\left(X_{ij}\middle|\boldsymbol{N}_{ij}\right)$ in Eq. (3), based on which the full joint PDF $Pr(\boldsymbol{X})$ can be recovered through Gibbs sampling (as explained in Section 3). According to probability theory, the conditional PDF $Pr\left(X_{ij}\middle|\boldsymbol{N}_{ij}\right)$ can be derived from the ratio between the local PDFs $Pr\left(X_{ij}, \boldsymbol{N}_{ij}\right)$ and $Pr\left(\boldsymbol{N}_{ij}\right)$:

$$Pr\left(X_{ij}\middle|\boldsymbol{N}_{ij}\right) = \frac{Pr(X_{ij}, \boldsymbol{N}_{ij})}{Pr(\boldsymbol{N}_{ij})} = \frac{O(X_{ij}, \boldsymbol{N}_{ij})}{O(\boldsymbol{N}_{ij})} \tag{6}$$

where CPDF $Pr\left(X_{ij}|\mathbf{N}_{ij}\right)$ defines the probability of a pixel's phase value equal to 1 or 0, given the phase values of its neighboring pixels $\mathbf{N}_{ij}$.

2.2. 2D microstructure characterization via statistics-informed neural network

Despite the MRF assumption, it is still intractable to build an accurate probability dictionary for the CPDF $Pr\left(X_{ij}|\mathbf{N}_{ij}\right)$ by using Eq. (6), especially for porous microstructures with highly complicated geometry. In this study, we approximate the CPDF $Pr\left(X_{ij}|\mathbf{N}_{ij}\right)$ by embedding it into a feed-forward neural network, called *statistics-informed neural network (SINN)*, and the methodology is graphically illustrated in Figure 6. For a 2D digital microstructure in the binary format (as shown in Figure 3c), the pixel value at any site of it can only be 1 (pore space) or 0 (solid matrix), as defined by the indicator function in Eq. (2). Therefore, the CPDF $Pr\left(X_{ij}|\mathbf{N}_{ij}\right)$ can be considered as the class probability of a binary classification problem, where the central pixel value X_{ij} corresponds to the classification category and the neighboring pixel pattern $\mathbf{N}_{ij}$ is treated as the classification feature.

Machine learning is good at solving classification problems by assigning the input feature to a predefined category. The data events $(X_{ij}, \mathbf{N}_{ij})$ here are paired observations, which comprise a perfect training dataset for fitting a classifier in the supervised learning paradigm. As illustrated in Figure 6, data events $(X_{ij}, \mathbf{N}_{ij})$ can be quickly collected from the 2D exemplars by using the predesigned data template to scan it in the raster scanning order [24]. By minimizing the misclassification chance, the class probabilities stored in the classifier will be an accurate approximation of the CPDF $Pr\left(X_{ij}|\mathbf{N}_{ij}\right)$. The common machine learning algorithms [46] used for classification include logic regression, decision tree, support vector machine, naive Bayes model, and feed-forward neural network. By comparisons, we found that the feed-forward neural network is particularly suitable to solve the nonlinear classification problem for image modeling.

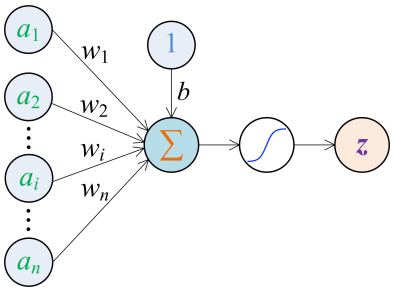

Figure 5: Graphic illustration of a basic neuron.

As illustrated in Figure 6, a feed-forward neural network with a shallow architecture consists of an input layer, 1 or 2 hidden layer(s), and an output layer. Each layer contains a number of interconnected neurons, which are the basic computational units possessing a certain degree of learning ability. A cohesive combination of many neuron units forms a neural network that possesses a powerful learning performance. As illustrated in Figure 5, a neuron generates a response z by acting a non-linear activation function $f(\cdot)$ on the weighted sum of the input data a_i, given by:

$$z = f\left(\sum_{i=1}^{n} w_i a_i + b\right) \tag{7}$$

where w_i is the weight, b is the bias, and n denotes the number of inputs.

In this study, the hyperbolic tangent function and sigmoid function are adopted as the activation functions for training the neural network. The hyperbolic tangent function $\tanh(h)$ transforms a continuous data h output from a hidden layer to the value between -1 and 1, which is mathematically expressed as follows:

$$\tanh(h) = \frac{e^{h} - e^{-h}}{e^{h} + e^{-h}} \tag{8}$$

The sigmoid function $\sigma(h)$ is connected to the output layer to transform a continuous data h to the probability between 0 and 1, which is mathematically expressed as follows:

$$\sigma(h) = \frac{1}{1 + e^{-h}} \tag{9}$$

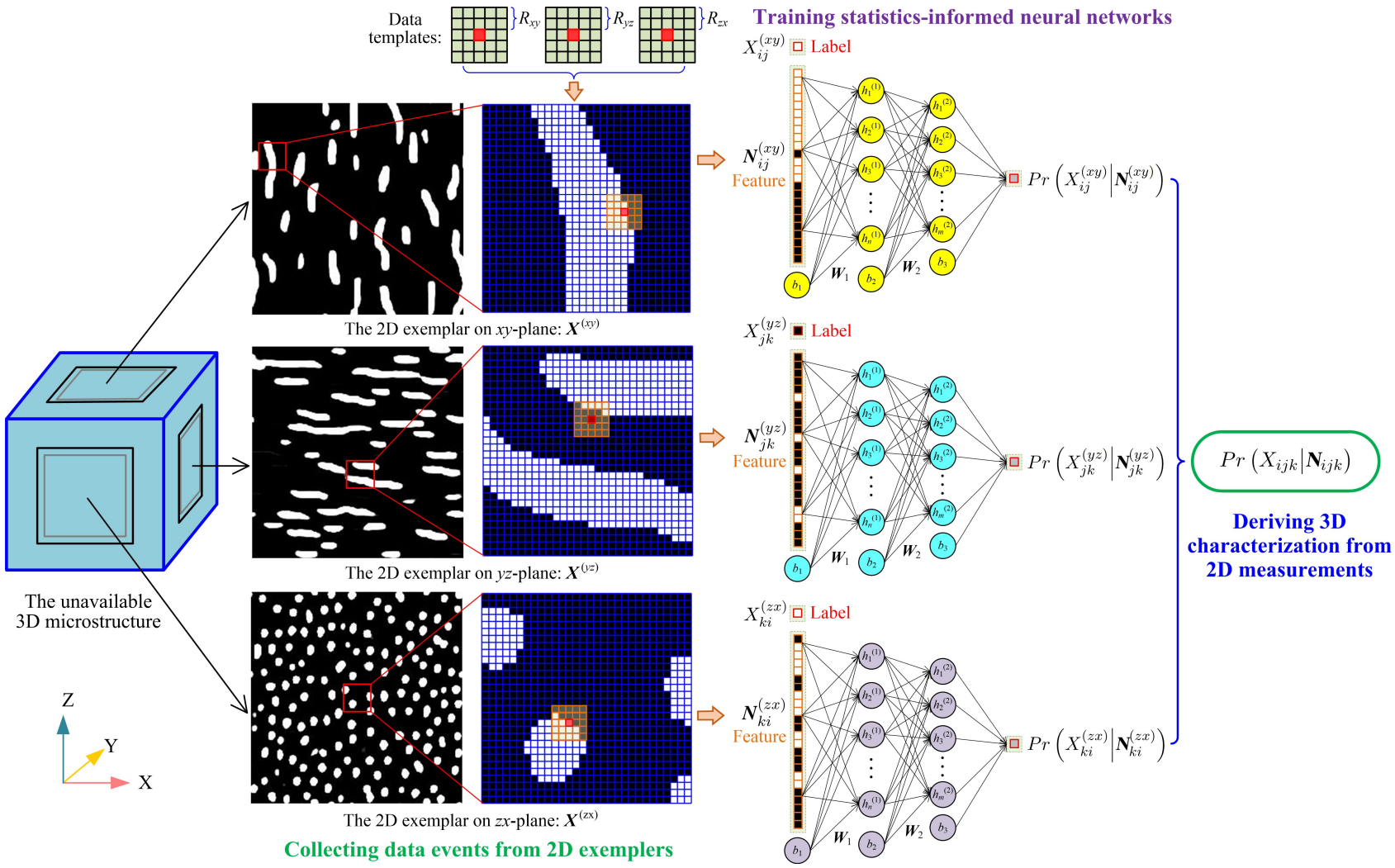

Figure 6: Graphic illustration of the methodology to statistically characterize random microstructures by training statistics-informed neural networks (SINNs). For anisotropic microstructures, the 2D exemplars on three orthogonal planes are required for statistical characterization; Data events are collected from these 2D exemplars by using different data templates to scan them in the raster scanning order; Three SINN models are separately trained by using the collected data events; The SINN models are the implicit representations of 2D morphological statistics, and such statistical information can be integrated together to be the morphological statistics in 3D space ($Pr\left(X_{ijk}\middle|\boldsymbol{N}_{ijk}\right)$).

Obviously, the data events $(X_{ij}, \boldsymbol{N}_{ij})$ collected from the 2D training image $\boldsymbol{X}$ are paired observations. To fit a feed-forward neural network (FNN) model for classification, the neighborhood pattern $\boldsymbol{N}_{ij}$ is treated as the classification feature (input), and the central pixel value X_{ij} acts as the classification category (output). It is noted that $\boldsymbol{N}_{ij}$ is reshaped to be a vector before inputting it to the FNN, as illustrated in Figure 6. The input feature vector is passed to the hidden layers, and the final output $\widehat{X}_{ij}$ can be computed through a series of forward-propagation equations, given by:

$$\begin{cases} \text{Input layer :} & \boldsymbol{H}^{(0)} = \boldsymbol{N}_{ij} \\ \text{1st hidden layer :} & \boldsymbol{H}^{(1)} = \tanh\left(\boldsymbol{W}_1^{\mathrm{T}}\boldsymbol{H}^{(0)} + b_1\right) \\ \text{2nd hidden layer :} & \boldsymbol{H}^{(2)} = \tanh\left(\boldsymbol{W}_2^{\mathrm{T}}\boldsymbol{H}^{(1)} + b_2\right) \\ \text{Output layer :} & \widehat{X}_{ij} = \boldsymbol{H}^{(\infty)} = \sigma\left(\boldsymbol{W}_3^{\mathrm{T}}\boldsymbol{H}^{(2)} + b_3\right) \end{cases} \tag{10}$$

where $\boldsymbol{H}^{(0)}$, $\boldsymbol{H}^{(1)}$, $\boldsymbol{H}^{(2)}$ and $\boldsymbol{H}^{(\infty)}$ denote the outputs from the input layer, the 1st hidden layer, the 2nd hidden layer and the output layer, respectively.

In essence, the fitted FNN model is a vector-valued surrogate to approximate the $\boldsymbol{N}_{ij}$-X_{ij} mapping for the training image $\boldsymbol{X}$, which can be mathematically expressed as follows:

$$\mathcal{FNN}\left(\boldsymbol{N}_{ij}; \boldsymbol{W}, \boldsymbol{b}\right): \ \boldsymbol{N}_{ij} \in \mathbb{R}^{d_N} \rightarrow X_{ij} \in \mathbb{R}^{d_X} \tag{11}$$

where $\mathcal{FNN}(\,\cdot\,)$ denotes the approximation function of the FNN model; $d_N = R^2 - 1$ and $d_X = 1$ denote the dimensions of the input data and the output data, respectively; R is the radius of the data template in Figure 4.

The training process of FNN is to minimize the discrepancy between the targets X_{ij} and the predictions $\widehat{X}_{ij}$ by iteratively adjusting the weight matrices $\boldsymbol{W}$ and bias vector $\boldsymbol{b}$. This optimization problem can be mathematically expressed as follows:

$$\begin{aligned} \underset{\boldsymbol{W},\boldsymbol{b}}{\arg\min} \ \mathcal{L}\left(X_{ij}, \boldsymbol{N}_{ij}; \boldsymbol{W}, \boldsymbol{b}\right) &= \frac{1}{m}\sum\left(X_{ij} - \widehat{X}_{ij}\right)^2 + \lambda\left\|\boldsymbol{W}\right\|_F^2 \\ &= \frac{1}{m}\sum\left[X_{ij} - \mathcal{FNN}(\boldsymbol{N}_{ij}; \boldsymbol{W}, \boldsymbol{b})\right]^2 + \lambda\left\|\boldsymbol{W}\right\|_F^2 \end{aligned} \tag{12}$$

where $\mathcal{L}(X_{ij}, \boldsymbol{N}_{ij}; \boldsymbol{W}, \boldsymbol{b})$ is the loss function of the neural network, m is the number of training data points, and λ is the weight regulation constant. The first term $\frac{1}{m}\sum\left(X_{ij} - \widehat{X}_{ij}\right)^2$ of the loss function is the mean squared error to represent the discrepancy between targets and predictions. The second term $\lambda\left\|\boldsymbol{W}\right\|_F^2$ is the L_2 weight regulation term, also called weight decay, which can force the network response to be smoother and thus reduce overfitting.

Once the FNN model is properly trained, it is able to predict the response $\widehat{X}_{ij}$ for an arbitrary input feature $\boldsymbol{N}_{ij}$. As explained in Eq. (10), the final response $\widehat{X}_{ij}$ of FNN is outputted from the sigmoid function (Eq. (9)), so the value of $\widehat{X}_{ij}$ is between 0 and 1. In essence, $\widehat{X}_{ij}$ is equivalent to the class probability stored in the fitted FNN classier, based on which the CPDF $Pr\left(X_{ij}\middle|\boldsymbol{N}_{ij}\right)$ can be accurately approximated:

$$Pr\left(X_{ij}\middle|\boldsymbol{N}_{ij}\right) = \begin{cases} Pr\left(X_{ij} = 1\middle|\boldsymbol{N}_{ij}\right) \approx \widehat{X}_{ij} = \mathcal{FNN}(\boldsymbol{N}_{ij}; \boldsymbol{W}, \boldsymbol{b}) \\ \\ Pr\left(X_{ij} = 0\middle|\boldsymbol{N}_{ij}\right) \approx 1 - \widehat{X}_{ij} = 1 - \mathcal{FNN}(\boldsymbol{N}_{ij}; \boldsymbol{W}, \boldsymbol{b}) \end{cases} \tag{13}$$

Therefore, the FNN model fitted by the data events $\left(X_{ij}, \boldsymbol{N}_{ij}\right)$ can be considered as an implicit representation of the CPDF $Pr\left(X_{ij}\middle|\boldsymbol{N}_{ij}\right)$, and it is referred to *statistics-informed neural network (SINN)* in this work.

In this study, the scaled conjugate gradient algorithm [47] is adopted to train SINN models with shallow architectures. Usually, a SINN model with one or two hidden layer(s) is able to capture the statistical characteristics of porous microstructures. The training process iteratively adjusts the weights and biases of the neural network, forcing it to evolve into the optimal state that best represents the CPDF $Pr\left(X_{ij}\middle|\boldsymbol{N}_{ij}\right)$ for the training image $\boldsymbol{X}$. Besides, cross-validation [48] is required to reduce the risk of overfitting the SINN models, so as to improve the generalization capacity for unseen data. More information about network training can be found in relevant references [46, 47, 48, 49].

2.3. 3D microstructure characterization from 2D measurements

The above subsections explain the methodology to statistically characterize 2D cross-sections by training *statistics-informed neural networks (SINNs)*. However, the 2D morphological statistics embedded in the set of SINN models cannot be directly used for the stochastic construction of 3D microstructures. To bridge the gap between 2D characterization and 3D reconstruction, it is necessary to infer 3D statistical characterization from 2D measurements.

As graphically illustrated in Figure 6, a morphology integration scheme is specially developed to derive 3D morphological statistics from 2D statistical characteristics. Generally, a 3D digital microstructure of porous media can be assumed as a 3D Markov random field, where the phase value of a voxel X_{ijk} at any site only depends on its neighboring voxels $\mathbf{N}_{ijk}$ within a certain range, so the flowing relation holds:

$$Pr\left(X_{ijk}\middle|\boldsymbol{X}^{(-ijk)}\right) = Pr\left(X_{ijk}\middle|\mathbf{N}_{ijk}\right) \tag{14}$$

where $\boldsymbol{X}^{(-ijk)}$ denotes the remaining pixels in the 3D image $\boldsymbol{X}$ excluding X_{ijk}. In this work, the above MRF assumption is further simplified to be that the phase value of a voxel X_{ijk} is only related to its neighboring voxels on three orthogonal planes: xy-, yz- and zx-plane within a sufficiently large range, give by:

$$Pr\left(X_{ijk}\middle|\mathbf{N}_{ijk}\right) = Pr\left[X_{ijk}\middle|\left(\mathbf{N}_{ijk}^{(xy)} \cup \mathbf{N}_{ijk}^{(yz)} \cup \mathbf{N}_{ijk}^{(zx)}\right)\right] \tag{15}$$

where $\mathbf{N}_{ijk}^{(xy)}$, $\mathbf{N}_{ijk}^{(yz)}$ and $\mathbf{N}_{ijk}^{(zx)}$ represent the neighboring voxels on xy-, yz- and zx-plane, respectively.

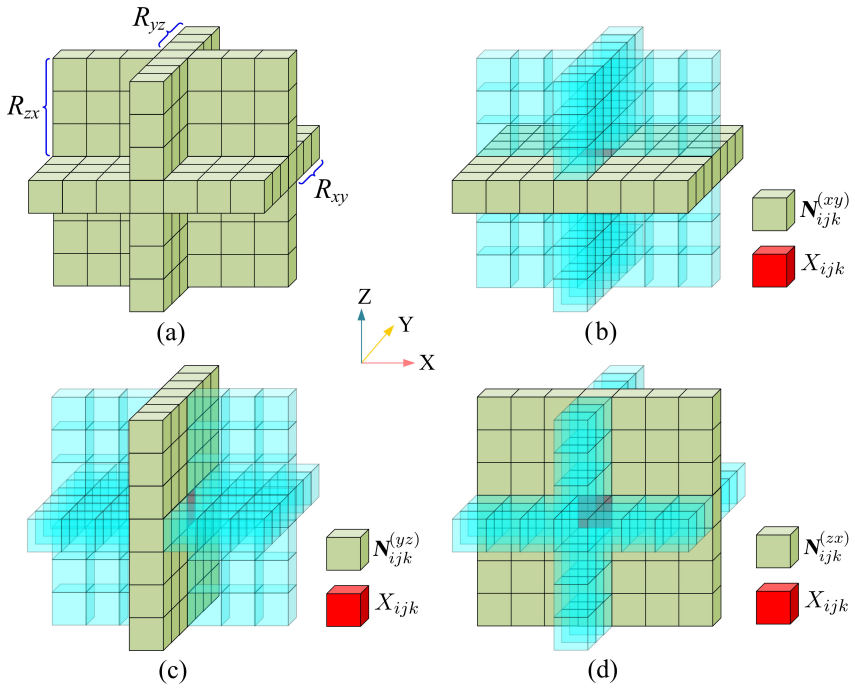

Figure 7: Graphic illustration of the 3D data template consisting of three 2D data templates on orthogonal planes: (a) The radii R of the neighborhood ranges on three orthogonal planes; (b) The neighboring voxels on xy-plane; (c) The neighboring voxels on yz-plane; and (d) The neighboring voxels on zx-plane.

As shown in Figure 7, a 3D data template is specially designed by combining three 2D square-shaped data templates (as shown in Figure 4) on orthogonal planes. Here, the *morphology-consistency assumption* is introduced to establish the relationship between 2D and 3D morphological statistics, which is mathematically expressed as follows:

$$Pr\left(X_{ijk}\middle|\mathbf{N}_{ijk}\right) = Pr\left(X_{ijk}\middle|\mathbf{N}_{ijk}^{(xy)}\right) = Pr\left(X_{ijk}\middle|\mathbf{N}_{ijk}^{(yz)}\right) = Pr\left(X_{ijk}\middle|\mathbf{N}_{ijk}^{(zx)}\right) \tag{16}$$

where the CPDFs $Pr\left(X_{ijk}\middle|\mathbf{N}_{ijk}\right)$, $Pr\left(X_{ijk}\middle|\mathbf{N}_{ijk}^{(xy)}\right)$, $Pr\left(X_{ijk}\middle|\mathbf{N}_{ijk}^{(yz)}\right)$ and $Pr\left(X_{ijk}\middle|\mathbf{N}_{ijk}^{(zx)}\right)$ statistically characterize the primary morphological features in 3D space and on three orthogonal planes, respectively. The above equation states

that the morphology patterns on three orthogonal planes are completely consistent with the morphological characteristics in 3D space. Despite the above statistical equivalence between CPDFs, the neighboring vectors $\boldsymbol{N}_{ijk}$, $\boldsymbol{N}_{ijk}^{(xy)}$, $\boldsymbol{N}_{ijk}^{(yz)}$ and $\boldsymbol{N}_{ijk}^{(zx)}$ can be greatly different from each other. In the extreme case where $R_{xy} = R_{yz} = R_{zx} = 0$, the flowing relation holds:

$$\begin{cases} Pr\left(X_{ijk}=1\right) = Pr\left(X_{ijk}^{(xy)}=1\right) = Pr\left(X_{ijk}^{(yz)}=1\right) = Pr\left(X_{ijk}^{(zx)}=1\right) = \phi \\ \\ Pr\left(X_{ijk}=0\right) = Pr\left(X_{ijk}^{(xy)}=0\right) = Pr\left(X_{ijk}^{(yz)}=0\right) = Pr\left(X_{ijk}^{(zx)}=0\right) = 1-\phi \end{cases} \tag{17}$$

where ϕ denotes the volume fraction of pore space (porosity). As to the other extreme case when $R_{xy} = R_{yz} = R_{zx} = +\infty$, the flowing relation can be obtained:

$$Pr\left(X_{ijk}\middle|\boldsymbol{N}_{ijk}\right) = Pr\left(X_{ijk}\middle|\boldsymbol{N}_{ijk}^{(xy)}\right) = Pr\left(X_{ijk}\middle|\boldsymbol{N}_{ijk}^{(yz)}\right) = Pr\left(X_{ijk}\middle|\boldsymbol{N}_{ijk}^{(zx)}\right) = 1 \text{ or } 0 \tag{18}$$

Considering this *morphology-consistency assumption*, the CPDF $Pr\left(X_{ijk}\middle|\boldsymbol{N}_{ijk}\right)$ in 3D space can be inferred from the 2D CPDFs on three orthogonal planes through an average operation:

$$Pr\left(X_{ijk}\middle|\boldsymbol{N}_{ijk}\right) = \frac{1}{3}\cdot\left[Pr\left(X_{ijk}\middle|\boldsymbol{N}_{ijk}^{(xy)}\right) + Pr\left(X_{ijk}\middle|\boldsymbol{N}_{ijk}^{(yz)}\right) + Pr\left(X_{ijk}\middle|\boldsymbol{N}_{ijk}^{(zx)}\right)\right] \tag{19}$$

where $Pr\left(X_{ijk}\middle|\boldsymbol{N}_{ijk}^{(xy)}\right)$, $Pr\left(X_{ijk}\middle|\boldsymbol{N}_{ijk}^{(yz)}\right)$ and $Pr\left(X_{ijk}\middle|\boldsymbol{N}_{ijk}^{(zx)}\right)$ are the 2D CPDFs to statistically characterize the primary morphological features existing the cross-sectional images on xy-, yz- and zx-plane, respectively. In this morphology integration scheme, equal weight is given to three orthogonal planes. It means that the phase value of a voxel will be codetermined by comparing three orthogonal planes centred at this voxel with the given 2D exemplars, during the process of microstructure reconstruction.

With the availability of 2D exemplars on three orthogonal planes, three SINN models can be separately trained to represent the 2D morphological statistics, and they are denoted by $\mathcal{FNN}_{xy}$, $\mathcal{FNN}_{yz}$ and $\mathcal{FNN}_{zx}$ respectively. As explained by Eq. (13), these SINN models are the implicit representations of the 2D CPDFs $Pr\left(X_{ijk}^{(xy)}\middle|\boldsymbol{N}_{ijk}^{(xy)}\right)$, $Pr\left(X_{ijk}^{(yz)}\middle|\boldsymbol{N}_{ijk}^{(yz)}\right)$ and $Pr\left(X_{ijk}^{(zx)}\middle|\boldsymbol{N}_{ijk}^{(zx)}\right)$ respectively. And the 3D CPDF $Pr\left(X_{ijk}\middle|\boldsymbol{N}_{ijk}\right)$ can then be accurately approximated from these SINN models according to Eq. (19), given by:

$$Pr\left(X_{ijk}\middle|\boldsymbol{N}_{ijk}\right) = \begin{cases} Pr\left(X_{ijk}=1\middle|\boldsymbol{N}_{ijk}\right) \approx \frac{1}{3}\cdot\left[\mathcal{FNN}_{xy}\left(\boldsymbol{N}_{ijk}^{(xy)}\right) + \mathcal{FNN}_{yz}\left(\boldsymbol{N}_{ijk}^{(yz)}\right) + \mathcal{FNN}_{zx}\left(\boldsymbol{N}_{ijk}^{(zx)}\right)\right] \\ \\ Pr\left(X_{ijk}=0\middle|\boldsymbol{N}_{ijk}\right) \approx 1-\frac{1}{3}\cdot\left[\mathcal{FNN}_{xy}\left(\boldsymbol{N}_{ijk}^{(xy)}\right) + \mathcal{FNN}_{yz}\left(\boldsymbol{N}_{ijk}^{(yz)}\right) + \mathcal{FNN}_{zx}\left(\boldsymbol{N}_{ijk}^{(zx)}\right)\right] \end{cases} \tag{20}$$

where $\mathcal{FNN}_{xy}(\cdot)$, $\mathcal{FNN}_{yz}(\cdot)$ and $\mathcal{FNN}_{zx}(\cdot)$ denote the approximation functions of the SINN models to statistically characterize the 2D exemplars on xy-, yz- and zx-plane, respectively.

For isotropic microstructures, the morphological features on different planes can be considered equivalent. Therefore, the cross-sectional images in one direction can be used as the only 2D exemplars to train the SINN model. The fitted SINN model is the implicit representations of both $Pr\left(X_{ijk}\middle|\boldsymbol{N}_{ijk}^{(xy)}\right)$, $Pr\left(X_{ijk}\middle|\boldsymbol{N}_{ijk}^{(yz)}\right)$ and $Pr\left(X_{ijk}\middle|\boldsymbol{N}_{ijk}^{(zx)}\right)$, from which the 3D morphological statistics can be inferred. As to anisotropic microstructures, the morphological patterns in different directions can be greatly distinct from each other. Therefore, the 2D slices on three orthogonal planes are all required to capture the microstructural anisotropy, which means the SINN models $\mathcal{FNN}_{xy}(\cdot)$, $\mathcal{FNN}_{yz}(\cdot)$ and $\mathcal{FNN}_{zx}(\cdot)$ should be trained separately.

It should be noted that only the 2D measurements on three principle planes are used to interpret the 3D microstructure in the above derivation process. Actually, the 2D exemplars on diagonal planes can also be involved in the morphology integration scheme, to provide a better characterization of the 3D microstructure, as illustrated in Figure 8. In this case, the 3D morphological statistics $Pr\left(X_{ijk}\middle|\boldsymbol{N}_{ijk}\right)$ can be estimated as the weighted average of the 2D CPDFs on nine planes, given by:

$$\begin{aligned} Pr\left(X_{ijk}\middle|\boldsymbol{N}_{ijk}\right) &= Pr\left[X_{ijk}\middle|\left(\boldsymbol{N}_{ijk}^{(xy)} \cup \boldsymbol{N}_{ijk}^{(yz)} \cup \boldsymbol{N}_{ijk}^{(zx)} \cup \boldsymbol{N}_{ijk}^{(xy\pm45)} \cup \boldsymbol{N}_{ijk}^{(yz\pm45)} \cup \boldsymbol{N}_{ijk}^{(zx\pm45)}\right)\right] \\ &= \frac{1}{9}\cdot\left[Pr\left(X_{ijk}\middle|\boldsymbol{N}_{ijk}^{(xy)}\right) + Pr\left(X_{ijk}\middle|\boldsymbol{N}_{ijk}^{(yz)}\right) + Pr\left(X_{ijk}\middle|\boldsymbol{N}_{ijk}^{(zx)}\right)\right. \\ &\quad \left. + Pr\left(X_{ijk}\middle|\boldsymbol{N}_{ijk}^{(xy\pm45)}\right) + Pr\left(X_{ijk}\middle|\boldsymbol{N}_{ijk}^{(yz\pm45)}\right) + Pr\left(X_{ijk}\middle|\boldsymbol{N}_{ijk}^{(zx\pm45)}\right)\right] \end{aligned} \tag{21}$$

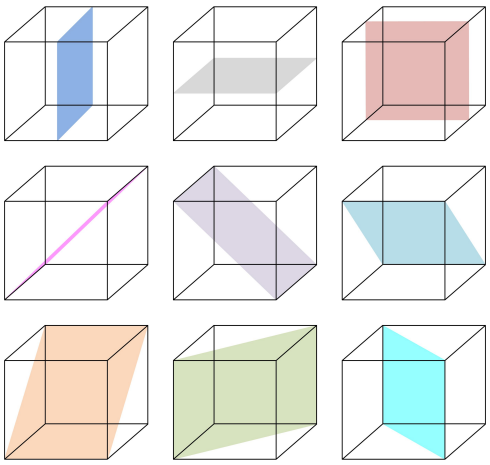

Figure 8: The 2D measurements on both principal and diagonal planes can be involved in the 3D microstructure characterization.

where the 2D CPFDs $Pr\left(X_{ijk}\middle|\boldsymbol{N}_{ijk}^{(xy\pm45)}\right)$, $Pr\left(X_{ijk}\middle|\boldsymbol{N}_{ijk}^{(yz\pm45)}\right)$ and $Pr\left(X_{ijk}\middle|\boldsymbol{N}_{ijk}^{(zx\pm45)}\right)$ denote the statistical characteristics of the 2D exemplars on six diagonal planes. This morphology integration scheme gives equal weight to nine different planes. It means that the phase value of a voxel will be codetermined by comparing the nine planes centred at this voxel with the given 2D exemplars, during the microstructure reconstruction process.

As explained by Eq. (13), these 2D CPDFs on different planes are implicitly represented by the pretrained SINN models, and the 3D morphological statistics $Pr\left(X_{ijk}\middle|\boldsymbol{N}_{ijk}\right)$ can be derived from these SINN models, given by:

$$Pr\left(X_{ijk}\middle|\boldsymbol{N}_{ijk}\right)=\begin{cases} Pr\left(X_{ijk}=1\middle|\boldsymbol{N}_{ijk}\right)\approx\frac{1}{9}\cdot\Big[\mathcal{FNN}_{xy}\left(\boldsymbol{N}_{ijk}^{(xy)}\right)+\mathcal{FNN}_{yz}\left(\boldsymbol{N}_{ijk}^{(yz)}\right)+\mathcal{FNN}_{zx}\left(\boldsymbol{N}_{ijk}^{(zx)}\right) \\ \qquad\qquad +\mathcal{FNN}_{xy\pm45}\left(\boldsymbol{N}_{ijk}^{(xy\pm45)}\right)+\mathcal{FNN}_{yz\pm45}\left(\boldsymbol{N}_{ijk}^{(yz\pm45)}\right)+\mathcal{FNN}_{zx\pm45}\left(\boldsymbol{N}_{ijk}^{(zx\pm45)}\right)\Big] \\ Pr\left(X_{ijk}=0\middle|\boldsymbol{N}_{ijk}\right)\approx1-\frac{1}{9}\cdot\Big[\mathcal{FNN}_{xy}\left(\boldsymbol{N}_{ijk}^{(xy)}\right)+\mathcal{FNN}_{yz}\left(\boldsymbol{N}_{ijk}^{(yz)}\right)+\mathcal{FNN}_{zx}\left(\boldsymbol{N}_{ijk}^{(zx)}\right) \\ \qquad\qquad +\mathcal{FNN}_{xy\pm45}\left(\boldsymbol{N}_{ijk}^{(xy\pm45)}\right)+\mathcal{FNN}_{yz\pm45}\left(\boldsymbol{N}_{ijk}^{(yz\pm45)}\right)+\mathcal{FNN}_{zx\pm45}\left(\boldsymbol{N}_{ijk}^{(zx\pm45)}\right)\Big] \end{cases} \tag{22}$$

where $\mathcal{FNN}_{xy\pm45}(\cdot)$, $\mathcal{FNN}_{yz\pm45}(\cdot)$ and $\mathcal{FNN}_{zx\pm45}(\cdot)$ denote the approximation functions of the SINN models to statistically characterize the 2D exemplars on different diagonal planes. For an anisotropic microstructure, a total of nine SINN models are required to represent these 2D CPDFs on different planes; while for an isotropic microstructure, the 2D morphological features on different planes can be considered equivalent, and thus only one SINN model is required to be trained.

2.4. Hierarchical microstructure characterization

Section 2.2 and Section 2.3 describe the procedures of a single-level characterization approach to deriving 3D statistical characteristics from 2D measurements by training SINN models. Generally, the data template size (as shown in Figure 4) should be sufficiently large to cover the primary microstructural characteristics of random media. This single-level characterization approach may work well for random microstructures with short-distance correlations [18]. However, the large-range correlations and the long-distance connectivity of porous microstructures are often global characteristics throughout the whole domain, which is usually beyond the capacity of the single-level characterization approach to cover. Crudely increasing the data template size can bring an unbearable computation burden, because it will dramatically increase the computational complexity and the memory requirement of training SINN models. Besides, important local features can be also diluted, due to the particular emphasis on global features.

To overcome the limitation of this single-level characterization approach, we further developed a hierarchical approach to separately characterize the local, regional and large-scale microstructural metrics by training multiple sets of SINN models, from which 3D morphology statistics at multiple length scales can be derived. The methodology of this hierarchical characterization approach is graphically explained in Figure 9, where a typical

anisotropic microstructure is used as the illustrative example. Besides, its algorithmic workflow is also concisely summarized in Algorithm 1. The procedure of this hierarchical characterization approach is as follows:

- **Step 1:** Gaussian image pyramids [50] with three levels are separately built for the original 2D exemplars $\boldsymbol{X}$ on different planes. The image pyramids from low level to high level are denoted by $\boldsymbol{X}^{(\text{low})}$, $\boldsymbol{X}^{(\text{middle})}$ and $\boldsymbol{X}^{(\text{high})}$ respectively. Gaussian image pyramids allow us to separately characterize the large-scale, regional and local microstructural metrics in different steps, and the large-scale microstructural metrics can be captured by using a relatively small data template.

- **Step 2:** The 2D low-level images denoted by $\boldsymbol{X}^{(\text{low})}$ are statistically characterized by training three independent SINN models, as explained in Section 2.2 and Section 2.3. According to Eq. (19), the 3D morphological statistics $Pr\left(X_{ijk}^{(\text{low})}\middle|\boldsymbol{N}_{ijk}^{(\text{low})}\right)$ at the low level can be inferred from the 2D CPDFs on three orthogonal planes, given by:

$$\begin{aligned} Pr\left(X_{ijk}^{(\text{low})}\middle|\boldsymbol{N}_{ijk}^{(\text{low})}\right) &= Pr\left[X_{ijk}^{(\text{low})}\middle|\left(\boldsymbol{N}_{ijk}^{(\text{low: }xy)} \cup \boldsymbol{N}_{ijk}^{(\text{low: }yz)} \cup \boldsymbol{N}_{ijk}^{(\text{low: }zx)}\right)\right] \\ &= \frac{1}{3}\cdot\left[Pr\left(X_{ijk}^{(\text{low})}\middle|\boldsymbol{N}_{ijk}^{(\text{low: }xy)}\right) + Pr\left(X_{ijk}^{(\text{low})}\middle|\boldsymbol{N}_{ijk}^{(\text{low: }yz)}\right) + Pr\left(X_{ijk}^{(\text{low})}\middle|\boldsymbol{N}_{ijk}^{(\text{low: }zx)}\right)\right] \end{aligned} \tag{23}$$

where $\boldsymbol{N}_{ijk}^{(\text{low: }xy)}$, $\boldsymbol{N}_{ijk}^{(\text{low: }yz)}$ and $\boldsymbol{N}_{ijk}^{(\text{low: }zx)}$ represent the neighboring voxels on xy-, yz- and zx-plane, respectively. The 2D CPDFs $Pr\left(X_{ijk}^{(\text{low})}\middle|\boldsymbol{N}_{ijk}^{(\text{low: }xy)}\right)$, $Pr\left(X_{ijk}^{(\text{low})}\middle|\boldsymbol{N}_{ijk}^{(\text{low: }yz)}\right)$ and $Pr\left(X_{ijk}^{(\text{low})}\middle|\boldsymbol{N}_{ijk}^{(\text{low: }zx)}\right)$ can be obtained from the pretrained SINN models according to Eq. (13). And the 3D CPDF $Pr\left(X_{ijk}^{(\text{low})}\middle|\boldsymbol{N}_{ijk}^{(\text{low})}\right)$ can then be approximated as follows:

$$Pr\left(X_{ijk}^{(\text{low})}\middle|\boldsymbol{N}_{ijk}^{(\text{low})}\right) = \begin{cases} Pr\left(X_{ijk}^{(\text{low})} = 1\middle|\boldsymbol{N}_{ijk}^{(\text{low})}\right) \approx \frac{1}{3}\cdot\left[\mathcal{FNN}_{xy}^{(\text{low})}\left(\boldsymbol{N}_{ijk}^{(\text{low: }xy)}\right)\right. \\ \qquad\qquad \left. +\mathcal{FNN}_{yz}^{(\text{low})}\left(\boldsymbol{N}_{ijk}^{(\text{low: }yz)}\right) + \mathcal{FNN}_{zx}^{(\text{low})}\left(\boldsymbol{N}_{ijk}^{(\text{low: }zx)}\right)\right] \\ Pr\left(X_{ijk}^{(\text{low})} = 0\middle|\boldsymbol{N}_{ijk}^{(\text{low})}\right) \approx 1 - \frac{1}{3}\cdot\left[\mathcal{FNN}_{xy}^{(\text{low})}\left(\boldsymbol{N}_{ijk}^{(\text{low: }xy)}\right)\right. \\ \qquad\qquad \left. +\mathcal{FNN}_{yz}^{(\text{low})}\left(\boldsymbol{N}_{ijk}^{(\text{low: }yz)}\right) + \mathcal{FNN}_{zx}^{(\text{low})}\left(\boldsymbol{N}_{ijk}^{(\text{low: }zx)}\right)\right] \end{cases} \tag{24}$$

where $\mathcal{FNN}_{xy}^{(\text{low})}(\cdot)$, $\mathcal{FNN}_{yz}^{(\text{low})}(\cdot)$ and $\mathcal{FNN}_{zx}^{(\text{low})}(\cdot)$ denote the approximation functions of the SINN models to statistically characterize the low-level 2D exemplars on xy-, yz- and zx-plane, respectively.

- **Step 3:** The 2D middle-level images $\boldsymbol{X}^{(\text{middle})}$ are used together with the 2D low-level images $\boldsymbol{X}^{(\text{low})}$ to train another set of SINN models for the statistical characterization at the middle level. It should be noted that the classification feature (input) contains the voxel values of $\boldsymbol{N}_{ijk}^{(\text{middle})}$, $X_{ijk}^{(\text{low})}$ and $\boldsymbol{N}_{ijk}^{(\text{low})}$, and the classification category (output) is the voxel value of $X_{ijk}^{(\text{middle})}$. This operation is not only to learn statistical informatics from $\boldsymbol{X}^{(\text{middle})}$, but also to learn the correlations between $\boldsymbol{X}^{(\text{middle})}$ and $\boldsymbol{X}^{(\text{low})}$, such as the feature consistency and the morphology continuity between adjacent levels. According to and Eq. (19), the 3D morphological statistics $Pr\left[X_{ijk}^{(\text{middle})}\middle|\left(\boldsymbol{N}_{ijk}^{(\text{middle})} \cup X_{ijk}^{(\text{low})} \cup \boldsymbol{N}_{ijk}^{(\text{low})}\right)\right]$ at the middle level can be derived from the 2D CPDFs on three orthogonal planes, given by:

$$\begin{aligned} Pr\left[X_{ijk}^{(\text{middle})}\middle|\left(\boldsymbol{N}_{ijk}^{(\text{middle})} \cup X_{ijk}^{(\text{low})} \cup \boldsymbol{N}_{ijk}^{(\text{low})}\right)\right] = \frac{1}{3}\cdot\left\{Pr\left[X_{ijk}^{(\text{middle})}\middle|\left(\boldsymbol{N}_{ijk}^{(\text{middle: }xy)} \cup X_{ijk}^{(\text{low})} \cup \boldsymbol{N}_{ijk}^{(\text{low: }xy)}\right)\right]\right. \\ +Pr\left[X_{ijk}^{(\text{middle})}\middle|\left(\boldsymbol{N}_{ijk}^{(\text{middle: }yz)} \cup X_{ijk}^{(\text{low})} \cup \boldsymbol{N}_{ijk}^{(\text{low: }yz)}\right)\right] \\ \left.+Pr\left[X_{ijk}^{(\text{middle})}\middle|\left(\boldsymbol{N}_{ijk}^{(\text{middle: }zx)} \cup X_{ijk}^{(\text{low})} \cup \boldsymbol{N}_{ijk}^{(\text{low: }zx)}\right)\right]\right\} \end{aligned} \tag{25}$$

where $\boldsymbol{N}_{ijk}^{(\text{middle: }xy)}$, $\boldsymbol{N}_{ijk}^{(\text{middle: }yz)}$ and $\boldsymbol{N}_{ijk}^{(\text{middle: }zx)}$ represent the neighboring voxels on xy-, yz- and zx-plane of the middle-level image $\boldsymbol{X}^{(\text{middle})}$, respectively. The 2D CPDFs $Pr\left[X_{ijk}^{(\text{middle})}\middle|\left(\boldsymbol{N}_{ijk}^{(\text{middle: }xy)} \cup X_{ijk}^{(\text{low})} \cup \boldsymbol{N}_{ijk}^{(\text{low: }xy)}\right)\right]$,

$Pr\Big[X_{ijk}^{(\text{middle})}\Big|\Big(\boldsymbol{N}_{ijk}^{(\text{middle: }yz)}\cup X_{ijk}^{(\text{low})}\cup\boldsymbol{N}_{ijk}^{(\text{low: }yz)}\Big)\Big]$ and $Pr\Big[X_{ijk}^{(\text{middle})}\Big|\Big(\boldsymbol{N}_{ijk}^{(\text{middle: }zx)}\cup X_{ijk}^{(\text{low})}\cup\boldsymbol{N}_{ijk}^{(\text{low: }zx)}\Big)\Big]$ can be obtained from the pretrained SINN models, as explained by Eq. (13). And the 3D CPDF $Pr\Big[X_{ijk}^{(\text{middle})}\Big|\Big(\boldsymbol{N}_{ijk}^{(\text{middle})}\cup X_{ijk}^{(\text{low})}\cup\boldsymbol{N}_{ijk}^{(\text{low})}\Big)\Big]$ can then be approximated as follows:

$$Pr\left[X_{ijk}^{(\text{middle})}\Big|\Big(\boldsymbol{N}_{ijk}^{(\text{middle})}\cup X_{ijk}^{(\text{low})}\cup\boldsymbol{N}_{ijk}^{(\text{low})}\Big)\right]=\begin{cases}Pr\left[X_{ijk}^{(\text{middle})}=1\Big|\Big(\boldsymbol{N}_{ijk}^{(\text{middle})}\cup X_{ijk}^{(\text{low})}\cup\boldsymbol{N}_{ijk}^{(\text{low})}\Big)\right]\\ \approx\frac{1}{3}\cdot\Big[\mathcal{FNN}_{xy}^{(\text{middle})}\Big(\boldsymbol{N}_{ijk}^{(\text{middle: }xy)}\cup X_{ijk}^{(\text{low})}\cup\boldsymbol{N}_{ijk}^{(\text{low: }xy)}\Big)\\ \quad+\mathcal{FNN}_{yz}^{(\text{middle})}\Big(\boldsymbol{N}_{ijk}^{(\text{middle: }yz)}\cup X_{ijk}^{(\text{low})}\cup\boldsymbol{N}_{ijk}^{(\text{low: }yz)}\Big)\\ \quad+\mathcal{FNN}_{zx}^{(\text{middle})}\Big(\boldsymbol{N}_{ijk}^{(\text{middle: }zx)}\cup X_{ijk}^{(\text{low})}\cup\boldsymbol{N}_{ijk}^{(\text{low: }zx)}\Big)\Big]\\ Pr\left[X_{ijk}^{(\text{middle})}=0\Big|\Big(\boldsymbol{N}_{ijk}^{(\text{middle})}\cup X_{ijk}^{(\text{low})}\cup\boldsymbol{N}_{ijk}^{(\text{low})}\Big)\right]\\ \approx 1-\frac{1}{3}\cdot\Big[\mathcal{FNN}_{xy}^{(\text{middle})}\Big(\boldsymbol{N}_{ijk}^{(\text{middle: }xy)}\cup X_{ijk}^{(\text{low})}\cup\boldsymbol{N}_{ijk}^{(\text{low: }xy)}\Big)\\ \quad+\mathcal{FNN}_{yz}^{(\text{middle})}\Big(\boldsymbol{N}_{ijk}^{(\text{middle: }yz)}\cup X_{ijk}^{(\text{low})}\cup\boldsymbol{N}_{ijk}^{(\text{low: }yz)}\Big)\\ \quad+\mathcal{FNN}_{zx}^{(\text{middle})}\Big(\boldsymbol{N}_{ijk}^{(\text{middle: }zx)}\cup X_{ijk}^{(\text{low})}\cup\boldsymbol{N}_{ijk}^{(\text{low: }zx)}\Big)\Big]\end{cases}\tag{26}$$

where $\mathcal{FNN}_{xy}^{(\text{middle})}(\cdot)$, $\mathcal{FNN}_{yz}^{(\text{middle})}(\cdot)$ and $\mathcal{FNN}_{zx}^{(\text{middle})}(\cdot)$ denote the approximation functions of the SINN models to statistically characterize the middle-level 2D exemplars on *xy*-, *yz*- and *zx*-plane, respectively.

- **Step 4:** The 2D high-level images $\boldsymbol{X}^{(\text{high})}$ and the 2D middle-level images $\boldsymbol{X}^{(\text{middle})}$ are used jointly to train a new set of SINN models, where the input feature vectors contain the voxel values of $\boldsymbol{N}_{ijk}^{(\text{high})}$, $X_{ijk}^{(\text{middle})}$ and $\boldsymbol{N}_{ijk}^{(\text{middle})}$. Similarly, this characterization manner is not only to learn statistical informatics from $\boldsymbol{X}^{(\text{high})}$, but also to learn the correlations between $\boldsymbol{X}^{(\text{high})}$ and $\boldsymbol{X}^{(\text{middle})}$, thereby maintaining the feature consistency and the morphology continuity between adjacent levels. According to Eq. (19), the 3D morphological statistics $Pr\Big[X_{ijk}^{(\text{high})}\Big|\Big(\boldsymbol{N}_{ijk}^{(\text{high})}\cup X_{ijk}^{(\text{middle})}\cup\boldsymbol{N}_{ijk}^{(\text{middle})}\Big)\Big]$ at the high level can be approximated from the 2D CPDFs on three orthogonal planes, given by:

$$\begin{aligned}Pr\left[X_{ijk}^{(\text{high}}\Big|\Big(\boldsymbol{N}_{ijk}^{(\text{high})}\cup X_{ijk}^{(\text{middle})}\cup\boldsymbol{N}_{ijk}^{(\text{middle})}\Big)\right]=\frac{1}{3}\cdot\Bigg\{&Pr\left[X_{ijk}^{(\text{high})}\Big|\Big(\boldsymbol{N}_{ijk}^{(\text{high: }xy)}\cup X_{ijk}^{(\text{middle})}\cup\boldsymbol{N}_{ijk}^{(\text{middle: }xy)}\Big)\right]\\&+Pr\left[X_{ijk}^{(\text{high})}\Big|\Big(\boldsymbol{N}_{ijk}^{(\text{high: }yz)}\cup X_{ijk}^{(\text{middle})}\cup\boldsymbol{N}_{ijk}^{(\text{middle: }yz)}\Big)\right]\\&+Pr\left[X_{ijk}^{(\text{high})}\Big|\Big(\boldsymbol{N}_{ijk}^{(\text{high: }zx)}\cup X_{ijk}^{(\text{middle})}\cup\boldsymbol{N}_{ijk}^{(\text{middle: }zx)}\Big)\right]\Bigg\}\end{aligned}\tag{27}$$

where $\boldsymbol{N}_{ijk}^{(\text{high: }xy)}$, $\boldsymbol{N}_{ijk}^{(\text{high: }yz)}$ and $\boldsymbol{N}_{ijk}^{(\text{high: }zx)}$ denote the neighboring voxels on *xy*-, *yz*- and *zx*-plane of the high-level image $\boldsymbol{X}^{(\text{high})}$, respectively. The 2D CPDFs $Pr\Big[X_{ijk}^{(\text{high})}\Big|\Big(\boldsymbol{N}_{ijk}^{(\text{high: }xy)}\cup X_{ijk}^{(\text{middle})}\cup\boldsymbol{N}_{ijk}^{(\text{middle: }xy)}\Big)\Big]$, $Pr\Big[X_{ijk}^{(\text{high})}\Big|\Big(\boldsymbol{N}_{ijk}^{(\text{high: }yz)}\cup X_{ijk}^{(\text{middle})}\cup\boldsymbol{N}_{ijk}^{(\text{middle: }yz)}\Big)\Big]$ and $Pr\Big[X_{ijk}^{(\text{high})}\Big|\Big(\boldsymbol{N}_{ijk}^{(\text{high: }zx)}\cup X_{ijk}^{(\text{middle})}\cup\boldsymbol{N}_{ijk}^{(\text{middle: }zx)}\Big)\Big]$ can be obtained from the pretrained SINN models, as illustrated by Eq. (13). And the 3D PDF $Pr\Big[X_{ijk}^{(\text{high}}\Big|\Big(\boldsymbol{N}_{ijk}^{(\text{high})}\cup X_{ijk}^{(\text{middle})}\cup\boldsymbol{N}_{ijk}^{(\text{middle})}\Big)\Big]$ can then

be approximated as follows:

$$Pr\left[X_{ijk}^{(\text{high})}\middle|\left(\boldsymbol{N}_{ijk}^{(\text{high})}\cup X_{ijk}^{(\text{middle})}\cup\boldsymbol{N}_{ijk}^{(\text{middle})}\right)\right]=\begin{cases}Pr\left[X_{ijk}^{(\text{high})}=1\middle|\left(\boldsymbol{N}_{ijk}^{(\text{high})}\cup X_{ijk}^{(\text{middle})}\cup\boldsymbol{N}_{ijk}^{(\text{middle})}\right)\right]\\ \approx\frac{1}{3}\cdot\left[\mathcal{FNN}_{xy}^{(\text{high})}\left(\boldsymbol{N}_{ijk}^{(\text{high: }xy)}\cup X_{ijk}^{(\text{middle})}\cup\boldsymbol{N}_{ijk}^{(\text{middle: }xy)}\right)\right.\\ \quad+\mathcal{FNN}_{yz}^{(\text{high})}\left(\boldsymbol{N}_{ijk}^{(\text{high: }yz)}\cup X_{ijk}^{(\text{middle})}\cup\boldsymbol{N}_{ijk}^{(\text{middle: }yz)}\right)\\ \quad\left.+\mathcal{FNN}_{zx}^{(\text{high})}\left(\boldsymbol{N}_{ijk}^{(\text{high: }zx)}\cup X_{ijk}^{(\text{middle})}\cup\boldsymbol{N}_{ijk}^{(\text{middle: }zx)}\right)\right]\\ \\ Pr\left[X_{ijk}^{(\text{high})}=0\middle|\left(\boldsymbol{N}_{ijk}^{(\text{high})}\cup X_{ijk}^{(\text{middle})}\cup\boldsymbol{N}_{ijk}^{(\text{middle})}\right)\right]\\ \approx 1-\frac{1}{3}\cdot\left[\mathcal{FNN}_{xy}^{(\text{high})}\left(\boldsymbol{N}_{ijk}^{(\text{high: }xy)}\cup X_{ijk}^{(\text{middle})}\cup\boldsymbol{N}_{ijk}^{(\text{middle: }xy)}\right)\right.\\ \quad+\mathcal{FNN}_{yz}^{(\text{high})}\left(\boldsymbol{N}_{ijk}^{(\text{high: }yz)}\cup X_{ijk}^{(\text{middle})}\cup\boldsymbol{N}_{ijk}^{(\text{middle: }yz)}\right)\\ \quad\left.+\mathcal{FNN}_{zx}^{(\text{high})}\left(\boldsymbol{N}_{ijk}^{(\text{high: }zx)}\cup X_{ijk}^{(\text{middle})}\cup\boldsymbol{N}_{ijk}^{(\text{middle: }zx)}\right)\right]\end{cases}\tag{28}$$

where $\mathcal{FNN}_{xy}^{(\text{high})}(\cdot)$, $\mathcal{FNN}_{yz}^{(\text{high})}(\cdot)$ and $\mathcal{FNN}_{zx}^{(\text{high})}(\cdot)$ denote the approximation functions of the SINN models to statistically characterize the high-level 2D exemplars on *xy*-, *yz*- and *zx*-plane, respectively.

In summary, this hierarchical characterization approach yields multiple sets of SINN models, and they are the implicit representations of the 2D morphological statistics at multiple levels. The 3D morphological statistics including $Pr\left(X_{ijk}^{(\text{low})}\middle|\boldsymbol{N}_{ijk}^{(\text{low})}\right)$, $Pr\left[X_{ijk}^{(\text{middle})}\middle|\left(\boldsymbol{N}_{ijk}^{(\text{middle})}\cup X_{ijk}^{(\text{low})}\cup\boldsymbol{N}_{ijk}^{(\text{low})}\right)\right]$ and $Pr\left[X_{ijk}^{(\text{high}}\middle|\left(\boldsymbol{N}_{ijk}^{(\text{high})}\cup X_{ijk}^{(\text{middle})}\cup\boldsymbol{N}_{ijk}^{(\text{middle})}\right)\right]$ can then be derived from these pretrained SINN models, which statistically characterize the microstructural metrics at different length scales. Specifically, large-scale correlations and long-distance connectivity are compactly captured in the low-level characterization step by using a relatively small data template. The regional features and local details are then captured in the middle-level and high-level characterizations steps respectively.

Generally, the level number of this hierarchical microstructure characterization is up to the microstructural complexities. To improve the accuracy of 3D microstructure interpretation, the 2D measurements on diagonal planes can also be involved in this hierarchical characterization approach, as explained in Figure 8 and Eq. (21). What's more, the obtained 3D CPDFs (including $Pr\left(X_{ijk}^{(\text{low})}\middle|\boldsymbol{N}_{ijk}^{(\text{low})}\right)$, $Pr\left[X_{ijk}^{(\text{middle})}\middle|\left(\boldsymbol{N}_{ijk}^{(\text{middle})}\cup X_{ijk}^{(\text{low})}\cup\boldsymbol{N}_{ijk}^{(\text{low})}\right)\right]$ and $Pr\left[X_{ijk}^{(\text{high}}\middle|\left(\boldsymbol{N}_{ijk}^{(\text{high})}\cup X_{ijk}^{(\text{middle})}\cup\boldsymbol{N}_{ijk}^{(\text{middle})}\right)\right]$) can be directly used to generate 3D microstructure samples by preserving the statistical equivalence, and more details about stochastic microstructure reconstruction are provided in the next section.

Algorithm 1: Hierarchical microstructure characterization via statistics-informed neural networks

Image data: Select representative 2D slices as the 2D exemplars on the xy-, yz- and zx-plane, which are denoted by $\boldsymbol{X}^{(xy)}$, $\boldsymbol{X}^{(yz)}$ and $\boldsymbol{X}^{(zx)}$ respectively.

(1) Gaussian image pyramids:

Compute the Gaussian image pyramid with multiple (three) levels for the 2D exemplar $\boldsymbol{X}^{(xy)}$, and the results from low level to high level are denoted by $\boldsymbol{X}^{(\text{low: } xy)}$, $\boldsymbol{X}^{(\text{middle: } xy)}$ and $\boldsymbol{X}^{(\text{high: } xy)}$ respectively;

Apply the same operation to the other two 2D exemplars $\boldsymbol{X}^{(yz)}$ and $\boldsymbol{X}^{(zx)}$;

Determine the sizes of 2D data templates for $\boldsymbol{X}^{(\text{low: } xy)}$, $\boldsymbol{X}^{(\text{middle: } xy)}$ and $\boldsymbol{X}^{(\text{high: } xy)}$, and the data templates are denote by $DT_{xy}^{(\text{low})}$, $DT_{xy}^{(\text{middle})}$ and $DT_{xy}^{(\text{high})}$ with the radii equal to $R_{xy}^{(\text{low})}$, $R_{xy}^{(\text{middle})}$ and $R_{xy}^{(\text{high})}$ respectively;

Apply the same operation to the other two sets of Gaussian image pyramids.

(2) Statistical microstructure characterization at the low level:

for $R_{xy}^{(\text{low})} + 1 \le i \le H_{xy}^{(\text{low})} - R_{xy}^{(\text{low})}$ **do**

  for $R_{xy}^{(\text{low})} + 1 \le j \le W_{xy}^{(\text{low})} - R_{xy}^{(\text{low})}$ **do**

    Collect the data event $\left(X_{ij}^{(\text{low: } xy)}, \boldsymbol{N}_{ij}^{(\text{low: } xy)}\right)$ from $\boldsymbol{X}^{(\text{low: } xy)}$ by using the 2D data template $DT_{xy}^{(\text{low})}$;

    Rearrange the neighboring data $\boldsymbol{N}_{ij}^{(\text{low: } xy)}$ into a feature vector;

    Move the 2D data template $DT_{xy}^{(\text{low})}$ to the next position in the raster scan order: $j = j + 1$;

  end

  Move the 2D data template $DT_{xy}^{(\text{low})}$ to the next line: $i = i + 1$;

end

Train a SINN model $\mathcal{FNN}_{xy}^{(\text{low})}$ by using the collected data events $\left(X_{ij}^{(\text{low: } xy)}, \boldsymbol{N}_{ij}^{(\text{low: } xy)}\right)$ as the training data;

Repeat the above procedures, and then the 2D exemplars $\boldsymbol{X}^{(\text{low: } yz)}$ and $\boldsymbol{X}^{(\text{low: } zx)}$ on yz- and zx-plane can be statistically characterized by training two SINN models denoted by $\mathcal{FNN}_{yz}^{(\text{low})}$ and $\mathcal{FNN}_{zx}^{(\text{low})}$ respectively;

The 3D CPDF $Pr\left(X_{ijk}^{(\text{low})} \middle| \boldsymbol{N}_{ijk}^{(\text{low})}\right)$ can be derived from relevant 2D CPDFs (the pretrained SINN models), according to Eq. (24).

(3) Statistical microstructure characterization at the middle level:

Resize $\boldsymbol{X}^{(\text{low: } xy)}$ to the same dimension as $\boldsymbol{X}^{(\text{middle: } xy)}$;

for $R_{xy}^{(\text{middle})} + 1 \le i \le H_{xy}^{(\text{middle})} - R_{xy}^{(\text{middle})}$ **do**

  for $R_{xy}^{(\text{middle})} + 1 \le j \le W_{xy}^{(\text{middle})} - R_{xy}^{(\text{middle})}$ **do**

    Collect the combined data event $\left(X_{ij}^{(\text{middle: } xy)}, \boldsymbol{N}_{ij}^{(\text{middle: } xy)} \cup X_{ij}^{(\text{low: } xy)} \cup \boldsymbol{N}_{ij}^{(\text{low: } xy)}\right)$ from $\boldsymbol{X}^{(\text{middle: } xy)}$ and $\boldsymbol{X}^{(\text{low: } xy)}$ by using the 2D data template $DT_{xy}^{(\text{middle})}$;

    Rearrange the combined data $\boldsymbol{N}_{ij}^{(\text{middle: } xy)} \cup X_{ij}^{(\text{low: } xy)} \cup \boldsymbol{N}_{ij}^{(\text{low: } xy)}$ into a feature vector;

    Move the 2D data template $DT_{xy}^{(\text{middle})}$ to the next position in the raster scan order: $j = j + 1$;

  end

  Move the 2D data template $DT_{xy}^{(\text{middle})}$ to the next line: $i = i + 1$;

end

Train a SINN model $\mathcal{FNN}_{xy}^{(\text{middle})}$ by using the combined data events $\left(X_{ij}^{(\text{middle: } xy)}, \boldsymbol{N}_{ij}^{(\text{middle: } xy)} \cup X_{ij}^{(\text{low: } xy)} \cup \boldsymbol{N}_{ij}^{(\text{low: } xy)}\right)$;

Repeat the above procedures, and then the 2D exemplars $\boldsymbol{X}^{(\text{middle: } yz)}$ and $\boldsymbol{X}^{(\text{middel: } zx)}$ on yz- and zx-plane can be statistically characterized by training two SINN models denoted by $\mathcal{FNN}_{yz}^{(\text{middle})}$ and $\mathcal{FNN}_{zx}^{(\text{middle})}$ respectively;

The 3D CPDF $Pr\left[X_{ijk}^{(\text{middle})} \middle| \left(\boldsymbol{N}_{ijk}^{(\text{middle})} \cup X_{ijk}^{(\text{low})} \cup \boldsymbol{N}_{ijk}^{(\text{low})}\right)\right]$ can be inferred from relevant 2D CPDFs, according to Eq. (26).

(4) Statistical microstructure characterization at the high level:

Resize $\boldsymbol{X}^{(\text{middle: } xy)}$ to the same dimension as $\boldsymbol{X}^{(\text{high: } xy)}$;

for $R_{xy}^{(\text{high})} + 1 \le i \le H_{xy}^{(\text{high})} - R_{xy}^{(\text{high})}$ **do**

  for $R_{xy}^{(\text{high})} + 1 \le j \le W_{xy}^{(\text{high})} - R_{xy}^{(\text{high})}$ **do**

    Collect the combined data event $\left(X_{ij}^{(\text{high: } xy)}, \boldsymbol{N}_{ij}^{(\text{high: } xy)} \cup X_{ij}^{(\text{low: xy})} \cup \boldsymbol{N}_{ij}^{(\text{middle: } xy)}\right)$ from $\boldsymbol{X}^{(\text{high: } xy)}$ and $\boldsymbol{X}^{(\text{middle: } xy)}$ by using the 2D data template $DT_{xy}^{(\text{high})}$;

    Rearrange the combined data $\boldsymbol{N}_{ij}^{(\text{high: } xy)} \cup X_{ij}^{(\text{middle: } xy)} \cup \boldsymbol{N}_{ij}^{(\text{middle: } xy)}$ into a feature vector;

    Move the 2D data template $DT_{xy}^{(\text{high})}$ to the next position in the raster scan order: $j = j + 1$;

  end

  Move the 2D data template $DT_{xy}^{(\text{high})}$ to the next line: $i = i + 1$;

end

Train a SINN model $\mathcal{FNN}_{xy}^{(\text{high})}$ by using the combined data events $\left(X_{ij}^{(\text{high: } xy)}, \boldsymbol{N}_{ij}^{(\text{high: } xy)} \cup X_{ij}^{(\text{middle: } xy)} \cup \boldsymbol{N}_{ij}^{(\text{middle: } xy)}\right)$;

Repeat the above procedures, and then the 2D exemplars $\boldsymbol{X}^{(\text{high: } yz)}$ and $\boldsymbol{X}^{(\text{high: } zx)}$ on yz- and zx-plane can be statistically characterized by training two SINN models denoted by $\mathcal{FNN}_{yz}^{(\text{high})}$ and $\mathcal{FNN}_{zx}^{(\text{high})}$ respectively;

The 3D CPDF $Pr\left[X_{ijk}^{(\text{high})} \middle| \left(\boldsymbol{N}_{ijk}^{(\text{high})} \cup X_{ijk}^{(\text{middle})} \cup \boldsymbol{N}_{ijk}^{(\text{middle})}\right)\right]$ can be derived from relevant 2D CPDFs, according to Eq. (28).

Return: Multiple (three) sets of SINN models that statistically characterize the microstructural metrics at different length scales.

(Note: $H_{xy}^{(\text{low})}$ and $W_{xy}^{(\text{low})}$ are the height and width of $\boldsymbol{X}^{(\text{low: } xy)}$ respectively; Similarly, $H_{xy}^{(\text{middle})}$, $W_{xy}^{(\text{middle})}$, $H_{xy}^{(\text{high})}$ and $W_{xy}^{(\text{high})}$ denote the sizes of $\boldsymbol{X}^{(\text{middle: } xy)}$ and $\boldsymbol{X}^{(\text{high: } xy)}$ respectively.)

3. Stochastic microstructure reconstruction

In Section 2, a hierarchical characterization approach is developed to statistically characterize 2D exemplars by training SINN models, from which 3D morphological statistics can be inferred at multiple length scales. The core issue here is how to make efficient use of this machine learning-based characterization to reconstruct statistically equivalent 3D microstructures. In this section, a multi-level reconstruction approach is developed to generate 3D microstructure samples by using the hierarchical 3D CPDFs, where the Gibbs sampler is adapted to construct and iteratively update the 3D realization towards the target distribution. As shown in Figure 9, the methodology of the multi-level microstructure reconstruction approach is graphically illustrated.

3.1. Gibbs sampling

Without knowing the full joint probability distribution, it is difficult to generate observations of multivariate random variables through direct sampling. Given the knowledge of conditional probability distributions, Gibbs sampling [51] is able to generate a sequence of observations that closely approximate the target multivariate probability distribution. According to Eq. (20), the 3D CPDF $Pr(Y_{ijk}|\boldsymbol{N}_{ijk})$ can be quickly derived from the pretrained SINN models, based on which Gibbs sampler is able to construct a 3D Markov random field (MRF). Gibbs sampling is used to iteratively update this 3D MRF from one state to another state by using the CPDFs. After enough iterations, the 3D MRF will converge to the stationary state that closely approximates the target full joint PDF, no matter what the initial state is. The 3D MRF obtained at the state of equilibrium can be treated as a reconstructed 3D microstructure sample that is statically equivalent to the 2D exemplars.

Algorithm 2: Gibbs sampling

Data: A 3D lattice grid of size $I \times J \times K$.
Initialization: Assign binary white noise to the 3D lattice grid as the initial state $\boldsymbol{Y}_0$.
while The convergence criterion is not satisfied **do**
  Pick an order for the $I \times J \times K$ voxel variables;
  for Each voxel Y_{ijk} **do**
    Generate a new voxel value $Y_{ijk}^{(\text{new})}$ by probability sampling from the CPDF $Pr\left(Y_{ijk}|\boldsymbol{N}_{ijk}\right)$;
    Update the voxel value Y_{ijk} by using $Y_{ijk}^{(\text{new})}$.
  end
end
Return: A constructed 3D Markov random field $\boldsymbol{Y}_{\text{new}}$ that closely approximates the target full joint PDF $Pr(\boldsymbol{Y})$.

In summary, Gibbs sampling achieves the full joint PDF $Pr(\boldsymbol{Y})$ by iteratively updating the initial 3D MRF $\boldsymbol{Y}_0$ based on the CPDF $Pr\left(Y_{ijk}|\boldsymbol{N}_{ijk}\right)$. The 3D MRF can be specified by three factors, which are the initial probability $Pr(\boldsymbol{Y}_0)$, the transition probability $Pr(Y_{ijk}|\boldsymbol{N}_{ijk})$ and the stationary probability $Pr(\boldsymbol{Y})$. The iterative process of Gibbs sampling can be expressed as follows:

$$Pr(\boldsymbol{Y}_0)\prod Pr\left(Y_{ijk}|\boldsymbol{N}_{ijk}\right) \rightarrow Pr(\boldsymbol{Y}) \tag{29}$$

And the pseudo-code of Gibbs sampling is given in Algorithm 2.

3.2. Multi-level microstructure reconstruction

As explained in Section 2.4, a set of 3D CPDFs can be derived from the available 2D exemplars by training SINN models at multiple levels. In essence, these 3D CPDFs including $Pr\left(X_{ijk}^{(\text{low})}|\boldsymbol{N}_{ijk}^{(\text{low})}\right)$, $Pr\left[X_{ijk}^{(\text{middle})}|\left(\boldsymbol{N}_{ijk}^{(\text{middle})} \cup X_{ijk}^{(\text{low})} \cup \boldsymbol{N}_{ijk}^{(\text{low})}\right)\right]$ and $Pr\left[X_{ijk}^{(\text{high})}|\left(\boldsymbol{N}_{ijk}^{(\text{high})} \cup X_{ijk}^{(\text{middle})} \cup \boldsymbol{N}_{ijk}^{(\text{middle})}\right)\right]$ statistically characterize the microstructural metrics at different length scales. To make full use of this multi-scale characterization, a multi-level reconstruction approach is specially developed to generate statistically equivalent 3D microstructure samples, as illustrated in Figure 9. During the reconstruction process, the pretrained SINN models are used as the dictionaries of conditional probabilities for Gibbs sampling. The workflow of this multi-level reconstruction approach is concisely summarized in Algorithm 3.

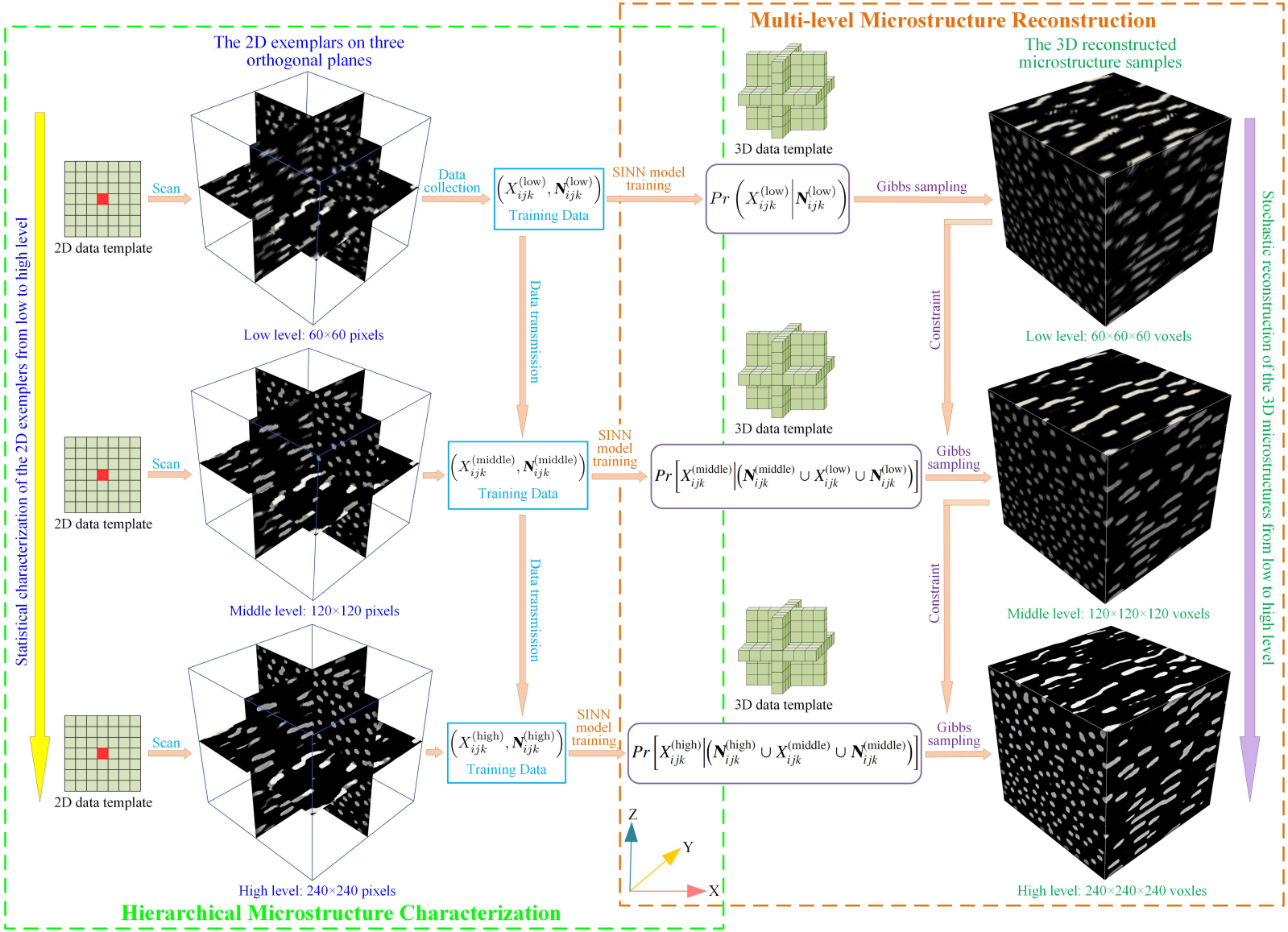

Figure 9: Graphic illustration of statistical characterization and stochastic reconstruction of random microstructures in a hierarchical manner.

Algorithm 3: Multi-level reconstruction of 3D random microstructures by using the hierarchical SINN-based characterization

SINN models: The pretrained SINN models are the implicit representations of 2D CPDFs at hierarchical length scales: $\mathcal{FNN}_{xy}^{(\text{low})}$, $\mathcal{FNN}_{yz}^{(\text{low})}$ and $\mathcal{FNN}_{zx}^{(\text{low})}$; $\mathcal{FNN}_{xy}^{(\text{middle})}$, $\mathcal{FNN}_{yz}^{(\text{middle})}$ and $\mathcal{FNN}_{zx}^{(\text{middle})}$; $\mathcal{FNN}_{xy}^{(\text{high})}$, $\mathcal{FNN}_{yz}^{(\text{high})}$ and $\mathcal{FNN}_{zx}^{(\text{high})}$.

Data templates: The 3D data templates $DT^{(\text{low})}$, $DT^{(\text{middle})}$ and $DT^{(\text{high})}$ are used for multi-level reconstruction, and their sizes are consistent with the 2D data templates used for hierarchical machine learning-based characterization.

(1) Stochastic microstructure reconstruction at the low level:
Generate a 3D lattice grid of size $I \times J \times K$, and assign binary white noise to it as the initial state $\mathbf{Y}_0^{(\text{low})}$;
while The convergence criterion is not satisfied **do**
  Add periodic boundaries to $\mathbf{Y}_0^{(\text{low})}$; Randomly select an order for the $I \times J \times K$ voxel variables in $\mathbf{Y}_0^{(\text{low})}$;
  for Each voxel $Y_{ijk}^{(\text{low})}$ in $\mathbf{Y}_0^{(\text{low})}$ **do**
    Extract the neighboring data $\mathbf{N}_{ijk}^{(\text{low})}$ from $\mathbf{Y}_0^{(\text{low})}$ by using the 3D data template $DT^{(\text{low})}$;
    Rearrange and split $\mathbf{N}_{ijk}^{(\text{low})}$ into three feature vectors for $\mathcal{FNN}_{xy}^{(\text{low})}$, $\mathcal{FNN}_{yz}^{(\text{low})}$ and $\mathcal{FNN}_{zx}^{(\text{low})}$ respectively;
    Compute the 3D CPDF $Pr\left(Y_{ijk}^{(\text{low})} \middle| \mathbf{N}_{ijk}^{(\text{low})}\right)$ from the above SINN models, according to Eq. (24);
    Gibbs sampler: Generate a new voxel value $Y_{ijk}^{(\text{low: new})}$ by probability sampling from the 3D CPDF $Pr\left(Y_{ijk}^{(\text{low})} \middle| \mathbf{N}_{ijk}^{(\text{low})}\right)$;
    Update the voxel value $Y_{ijk}^{(\text{low})}$ by using $Y_{ijk}^{(\text{low: new})}$.
  end
end
Return: The low-level constructed 3D microstructure sample $\mathbf{Y}_{\text{new}}^{(\text{low})}$.

(2) Stochastic microstructure reconstruction at the middle level:
Generate a 3D lattice grid of size $2I \times 2J \times 2K$, and assign binary white noise to it as the initial state $\mathbf{Y}_0^{(\text{middle})}$;
Resize the low-level reconstruction result $\mathbf{Y}_{\text{new}}^{(\text{low})}$ to $2I \times 2J \times 2K$, and still denote it as $\mathbf{Y}_{\text{new}}^{(\text{low})}$;
while The convergence criterion is not satisfied **do**
  Add periodic boundaries to both $\mathbf{Y}_0^{(\text{middle})}$ and $\mathbf{Y}_{\text{new}}^{(\text{low})}$;
  Randomly select an order for the $2I \times 2J \times 2K$ voxel variables in $\mathbf{Y}_0^{(\text{middle})}$;
  for Each voxel $Y_{ijk}^{(\text{middle})}$ in $\mathbf{Y}_0^{(\text{middle})}$ **do**
    Extract the neighboring data $\mathbf{N}_{ijk}^{(\text{middle})}$ from $\mathbf{Y}_0^{(\text{middle})}$ by using the 3D data template $DT^{(\text{middle})}$;
    Extract the data event $\left(Y_{ijk}^{(\text{low})}, \mathbf{N}_{ijk}^{(\text{low})}\right)$ from $\mathbf{Y}_{\text{new}}^{(\text{low})}$ by using the 3D data template $DT^{(\text{middle})}$;
    Rearrange and split the combined data $\mathbf{N}_{ijk}^{(\text{middle})} \cup Y_{ijk}^{(\text{low})} \cup \mathbf{N}_{ijk}^{(\text{low})}$ into three feature vectors for $\mathcal{FNN}_{xy}^{(\text{middle})}$, $\mathcal{FNN}_{yz}^{(\text{middle})}$ and $\mathcal{FNN}_{zx}^{(\text{middle})}$ respectively;
    Compute the 3D CPDF $Pr\left[Y_{ijk}^{(\text{middle})} \middle| \left(\mathbf{N}_{ijk}^{(\text{middle})} \cup Y_{ijk}^{(\text{low})} \cup \mathbf{N}_{ijk}^{(\text{low})}\right)\right]$ from the above SINN models, according to Eq. (26).
    Gibbs sampler: Generate a new voxel value $Y_{ijk}^{(\text{middle: new})}$ by sampling from $Pr\left[Y_{ijk}^{(\text{middle})} \middle| \left(\mathbf{N}_{ijk}^{(\text{middle})} \cup Y_{ijk}^{(\text{low})} \cup \mathbf{N}_{ijk}^{(\text{low})}\right)\right]$;
    Update the voxel value $Y_{ijk}^{(\text{middle})}$ by using $Y_{ijk}^{(\text{middle: new})}$.
  end
end
Return: The middle-level constructed 3D microstructure sample $\mathbf{Y}_{\text{new}}^{(\text{middle})}$.

(3) Stochastic microstructure reconstruction at the high level:
Generate a 3D lattice grid of size $4I \times 4J \times 4K$, and assign binary white noise to it as the initial state $\mathbf{Y}_0^{(\text{high})}$;
Resize the middle-level reconstruction result $\mathbf{Y}_{\text{new}}^{(\text{middle})}$ to $4I \times 4J \times 4K$, and still denote it as $\mathbf{Y}_{\text{new}}^{(\text{middle})}$;
while The convergence criterion is not satisfied **do**
  Add periodic boundaries to both $\mathbf{Y}_0^{(\text{high})}$ and $\mathbf{Y}_{\text{new}}^{(\text{middle})}$;
  Randomly select an order for the $4I \times 4J \times 4K$ voxel variables in $\mathbf{Y}_0^{(\text{high})}$;
  for Each voxel $Y_{ijk}^{(\text{high})}$ in $\mathbf{Y}_0^{(\text{high})}$ **do**
    Extract the neighboring data $\mathbf{N}_{ijk}^{(\text{high})}$ from $\mathbf{Y}_0^{(\text{high})}$ by using the 3D data template $DT^{(\text{high})}$;
    Extract the data event $\left(Y_{ijk}^{(\text{middle})}, \mathbf{N}_{ijk}^{(\text{middle})}\right)$ from $\mathbf{Y}_{\text{new}}^{(\text{middle})}$ by using the 3D data template $DT^{(\text{high})}$;
    Rearrange and split the combined data $\mathbf{N}_{ijk}^{(\text{high})} \cup Y_{ijk}^{(\text{middle})} \cup \mathbf{N}_{ijk}^{(\text{middle})}$ into three feature vectors for $\mathcal{FNN}_{xy}^{(\text{high})}$, $\mathcal{FNN}_{yz}^{(\text{high})}$ and $\mathcal{FNN}_{zx}^{(\text{high})}$ respectively;
    Compute the 3D CPDF $Pr\left[Y_{ijk}^{(\text{high})} \middle| \left(\mathbf{N}_{ijk}^{(\text{high})} \cup Y_{ijk}^{(\text{middle})} \cup \mathbf{N}_{ijk}^{(\text{middle})}\right)\right]$ from the above SINN models, according to Eq. (28).
    Gibbs sampler: Generate a new voxel value $Y_{ijk}^{(\text{high: new})}$ by sampling from $Pr\left[Y_{ijk}^{(\text{high})} \middle| \left(\mathbf{N}_{ijk}^{(\text{high})} \cup Y_{ijk}^{(\text{middle})} \cup \mathbf{N}_{ijk}^{(\text{middle})}\right)\right]$;
    Update the voxel value $Y_{ijk}^{(\text{high})}$ by using $Y_{ijk}^{(\text{high: new})}$.
  end
end
Return: The high-level constructed 3D microstructure sample $\mathbf{Y}_{\text{new}}^{(\text{high})}$ (the final reconstruction result $\mathbf{Y}_{\text{new}}$).

In the low-level construction step, large-scale microstructural characteristics (such as long-distance connectivity) are compactly preserved in the 3D constructed sample. The middle-level construction process is constrained by the low-level reconstruction result, where regional microstructural metrics are added to the 3D sample inherited from the low-level step. Such an operation can maintain morphology consistency and continuity between the 3D samples constructed at two different levels. As to the high-level construction, local microstructural details are mingled in the 3D constructed sample, in order to make it morphologically close to the real microstructure. In summary, the large-scale, regional and local morphological patterns are statistically generated and successively added to the same 3D random field via Gibbs sampling, where the required 3D CPDFs are quickly derived from the pretrained SINN models that implicitly represent the 2D morphological statistics at multiple scales.

3.3. Parameter settings

There are several important parameters in the proposed hierarchical microstructure reconstruction approach, such as data template size, boundary condition, sampling ratio and convergence tolerance. These parameter settings should be carefully determined, because they can bring a great influence on both the accuracy and efficiency of microstructure reconstruction.

3.3.1. Data template size

As explained in Section 2.4 and Section 3.2, data template size is a critical parameter for both statistical characterization and stochastic reconstruction. The size of a data template is measured by the radius of its neighboring pixel/voxel zone, as shown in Figure 4 and Figure 7. Generally, the template size should be large enough to cover the primary microstructural features. To seamlessly connect stochastic microstructure reconstruction to statistical SINN-based characterization, the dimensions of the 3D template should be consistent with the radii of the previously used 2D templates.

In our previous study [18], a determination method of data template size R has already been developed for different microstructures, and it can be directly adopted here. The minimum value of R can be estimated from the two-point correlation function (TPCF) [7] of the 2D training image. Considering the difference between the data templates used in these two studies, the correlation length a provides a reference value for $2R$ in this study, which can be computed by fitting the TPCF curve with an exponential function as defined below:

$$S_2(d) = (\phi - \phi^2)\exp(-\frac{3d}{a}) + \phi^2 \tag{30}$$

where $S_2(d)$ denotes TPCF, ϕ is the volume fraction of the calculated phase, and d is the distance between two pixel/voxel points.

3.3.2. Boundary condition

During the microstructure reconstruction process, the border voxels do not have enough neighborhoods to play as the feature vectors for the pretrained SINN models, and thus their voxel values can not be updated. To overcome this problem, the periodic or reflective boundary is added to the intermediate constructed MRF, and then the original "border voxels" become inner voxels that can be updated during the construction process. The thickness of the periodic or reflective boundary should be consistent with the dimension of the 3D data template used for microstructure reconstruction. Also, the periodic or reflective boundary should be reset after each round of Gibbs sampling, until the constructed microstructure becomes stable. More details about periodic or reflective boundaries can be found in relevant references [18, 33].

3.3.3. Sampling ratio

During the microstructure reconstruction process (as explained in Algorithm 3), voxel values are generated and updated one by one in random order through Gibbs sampling. Such a voxel update process could be time-consuming, because the Markov chain is usually a very long sequence with millions even billions of voxels. According to the MRF assumption illustrated in Section 2.1, two pixels/voxels are assumed to be irrelevant when the distance between them is sufficiently long. In other words, two voxels can be considered independent of each other if they cannot be covered by the predefined 3D data template (as shown in Fig 7). Therefore, the phase values of these independent voxels can be generated and updated simultaneously through Gibbs sampling, which will significantly speed up the reconstruction process.

Here, the proportion between the sampling voxel number at each time and the total voxel number inside the reconstructed microstructure is defined as the sampling ratio. It is a key parameter that controls microstructure

reconstruction efficiency. In an extreme case, this sampling ratio can be set to 1.00, which means all of the voxel values will be generated and updated at the same time through probability sampling. Although direct sampling of all voxel values does not exactly conform to Gibbs sampling, the reconstruction process can be significantly accelerated. In general, selecting a proper sampling ratio is to make a balance between computation efficiency, reconstruction accuracy, and computer performance (such as memory requirement).

3.3.4. Convergence criterion

As illustrated in Algorithm 3, Gibbs sampling runs continuously until the steady state of the constructed sample is reached. The reconstruction process is assumed to be stable if the deviation of the constructed samples between two adjacent iterations falls below a certain tolerance value. Here, the convergence criterion of microstructure reconstruction is mathematically expressed as follows:

$$\varepsilon_i = \frac{\|\mathbf{Y}_i - \mathbf{Y}_{i-1}\|_2}{\|\mathbf{Y}_{i-1}\|_2} \leq \eta \tag{31}$$

where ε_i is the relative L_2-norm error measuring the discrepancy between the constructed samples $\mathbf{Y}_i$ and $\mathbf{Y}_{i-1}$; i denotes the iteration number; $\eta \lesssim 1$ is a user-specified tolerance with small value.

4. Examples and results

To verify the effectiveness of this hierarchical 2D-to-3D microstructure reconstruction method, we test it on a series of porous media with distinct morphology patterns. In each testing case, a group of thirty 3D microstructure samples is generated by using the proposed method. For the 4th and 5th testing case, the developed SINN-based method is systematically compared with the GAN-based method [39], in terms of microstructure reconstruction quality and speed. More details about the GAN-based method can be found in relevant references [38, 39]. To demonstrate the statistical equivalence between the 3D reconstructed and the real microstructures, a variety of morphological descriptors are used to quantitatively characterize these porous microstructures. More details about morphological descriptors can be found in relevant references [7, 52, 53]. It should be noted that all the morphological descriptors are computed for the pore space (white phase). In this work, reconstruction error Δf is measured by the relative $\mathcal{L}_2$-norm, given by:

$$\Delta f = \frac{\left\| \widehat{f(d)} - f(d) \right\|_2}{\|f(d)\|_2} \tag{32}$$

where $f(d)$ and $\widehat{f(d)}$ denote the morphological descriptors extracted from the reference and the reconstructed microstructures respectively.

Table 1: The parameters of hierarchical microstructure reconstruction for different testing cases

Test case	Level	Data template size (voxel)	Training *statistics-informed neural networks (SINNs)*				Sampling ratio
			Learning rate	Epoch number	Number of neurons		
					Hidden layer 1	Hidden layer 2	
Case 1	Low:	$R_{xy} = R_{yz} = R_{zx} = 2$	0.00001	200	24	– –	100%
	Middle:	$R_{xy} = R_{yz} = R_{zx} = 4$	0.00001	500	48	– –	100%
	High:	$R_{xy} = R_{yz} = R_{zx} = 8$	0.00001	500	96	– –	100%
Case 2	Low:	$R_{xy} = 2, R_{yz} = 6, R_{zx} = 6$	0.00001	1000	30	– –	100%
	Middle:	$R_{xy} = 4, R_{yz} = 10, R_{zx} = 10$	0.00001	500	40	– –	100%
	High:	$R_{xy} = 8, R_{yz} = 15, R_{zx} = 15$	0.00001	300	60	– –	100%
Case 3	Low:	$R_{xy} = R_{yz} = R_{zx} = 7$	0.00001	200	10	10	100%
	Middle:	$R_{xy} = R_{yz} = R_{zx} = 12$	0.00001	500	20	20	100%
	High:	$R_{xy} = R_{yz} = R_{zx} = 16$	0.00001	500	30	30	100%
Case 4	Low:	$R_{xy} = R_{yz} = R_{zx} = 8$	0.00001	500	60	– –	100%
	Middle:	$R_{xy} = R_{yz} = R_{zx} = 16$	0.00001	500	120	– –	100%
Case 5	Low:	$R_{xy} = R_{yz} = R_{zx} = 7$	0.00001	500	15	15	100%
	Middle:	$R_{xy} = R_{yz} = R_{zx} = 12$	0.00001	500	30	30	100%
	High:	$R_{xy} = R_{yz} = R_{zx} = 16$	0.00001	200	50	50	100%

As mentioned in Section 2.2, the scaled conjugate gradient algorithm is adopted to train neural networks for the statistical characterization of 2D exemplars. To reduce the risk of overfitting the SINN models, the data events collected from the available 2D exemplars are randomly split into the training dataset (80%) and the validation dataset (20%). The model hyper-parameters and the algorithm hyper-parameters of SINN model training for different testing cases are summarized in Table 1. As to 3D microstructure reconstruction, the sampling ratio has a great influence on reconstruction efficiency, its value for each testing case is listed in Table 1 as well.

4.1. Case 1: Porous ceramic with spherical pores

The first case is a porous lead zirconate titanate (PZT) ceramic, which was prepared by sintering compacts that consist of PZT and pore former. The physical properties of porous PZT ceramics were investigated as functions of pore shape and porosity [54]. As shown in Figure 10, the pores (white phase) inside this porous ceramic are isolated spheres, and pore space only occupies 4.25% of the bulk volume. Although the microstructural characteristics of this porous ceramic are simple, the extremely low porosity can bring a huge challenge to the proposed microstructure reconstruction method, because the informatics of pore space can be overwhelmed by that of the solid matrix during the process of machine learning-based characterization. Obviously, this porous microstructure is isotropic, but we still select 9 representative slices on three principal planes and six diagonal planes as the 2D exemplars for 3D microstructure reconstruction. Here, only the 2D exemplars on three principle planes are shown in the rightmost column in Figure 10.

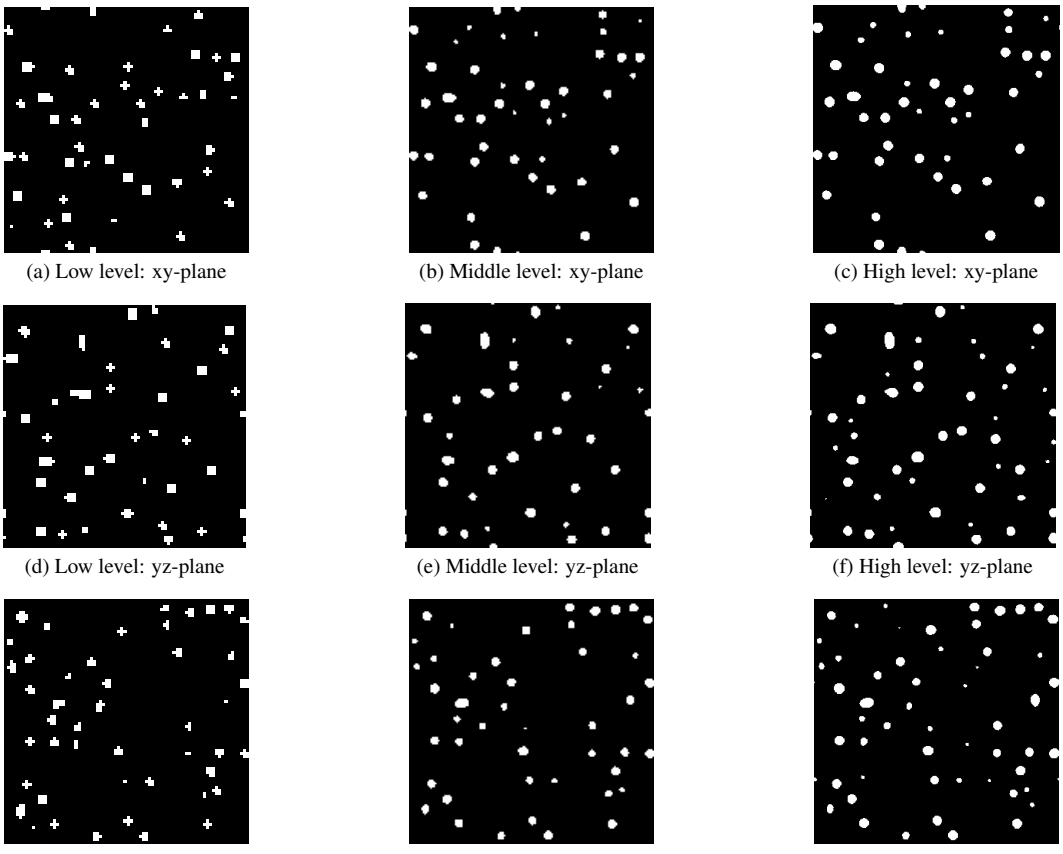

(a) Low level: xy-plane (b) Middle level: xy-plane (c) High level: xy-plane

(d) Low level: yz-plane (e) Middle level: yz-plane (f) High level: yz-plane

(g) Low level: zx-plane (h) Middle level: zx-plane (i) High level: zx-plane

Figure 10: Gaussian image pyramids with three levels: (a), (d) and (g) are the low-level images (80×80 pixels); (b), (e) and (h) are the middle-level images (160×160 pixels); (c), (f) and (i) are the high-level images (the original 2D exemplars with 320×320 pixels).

To investigate the necessity of hierarchical characterization and reconstruction, we first apply the single-level approach for microstructure characterization and reconstruction, where the original 2D exemplars are directly used as the training images to train SINN models (more details can be found in Section 2.2 and Section 2.3). As shown in Figure 11, 3D microstructures are scholastically generated by the single-level approach, where data templates of varying sizes are used. However, these 3D reconstructed microstructures don't preserve the morphology patterns existing in the given 2D examples. For the single-level approach, data templates must be set with large radii, in

order to cover the primary microstructural features. The large neighborhood areas can make it difficult to let the 2D-to-3D morphology integration evolve into the optimal state where the morphological patterns of 3D relations are consistent with that of the 2D exemplars. By contrast, the proposed hierarchical approach allows for compact characterization and generation of the large-sized morphology by using a small data template, which can greatly simplify the 2D-to-3D morphology integration.

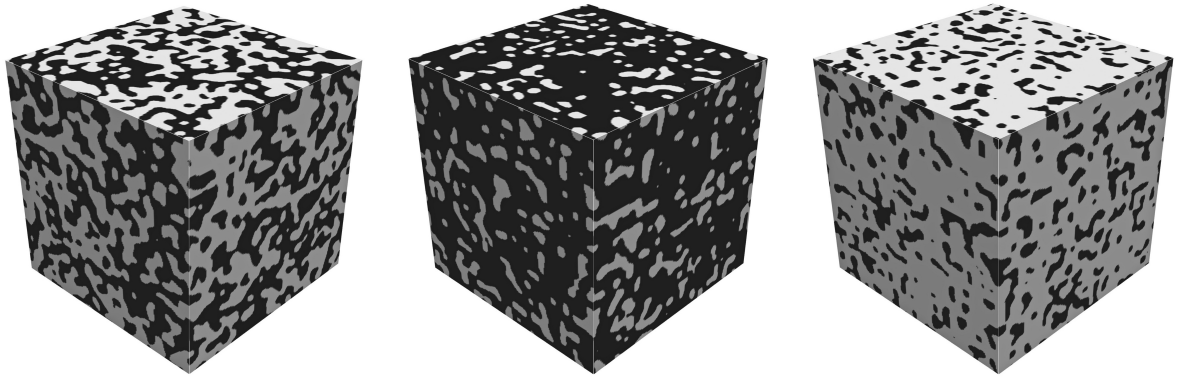

(a) $R_{xy} = R_{yz} = R_{zx} = 8$ voxels (b) $R_{xy} = R_{yz} = R_{zx} = 10$ voxels (c) $R_{xy} = R_{yz} = R_{zx} = 12$ voxels

Figure 11: Single-level microstructure reconstruction (240×240×240 voxels) by using the data templates with varying radii.

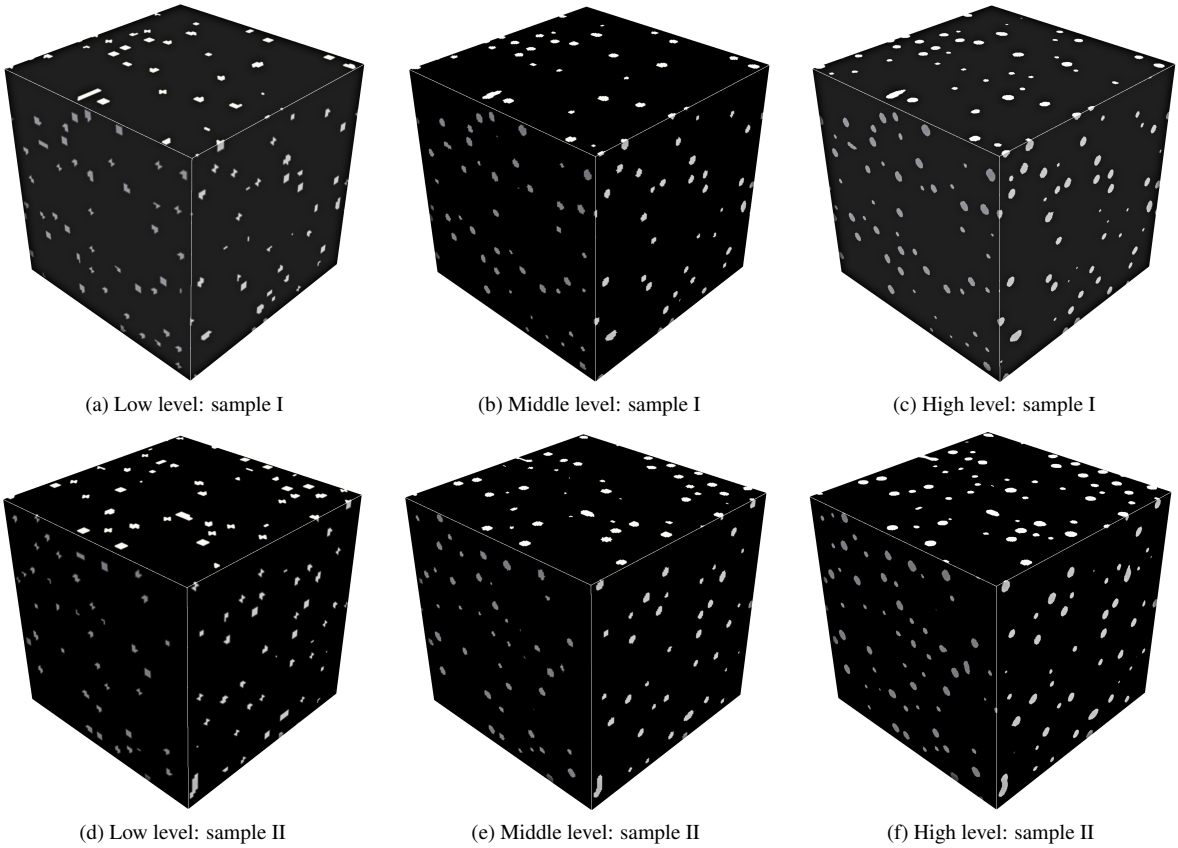

(a) Low level: sample I (b) Middle level: sample I (c) High level: sample I

(d) Low level: sample II (e) Middle level: sample II (f) High level: sample II

Figure 12: Hierarchical microstructure reconstruction with three levels: (a) and (d) are the low-level reconstruction results (80×80×80 voxels); (b) and (e) are the middle-level reconstruction results (160×160×160 voxels); (c) and (f) are the high-level reconstruction results (the final 3D reconstructed samples with 320×320×320 voxels).

In other words, the proposed hierarchical approach decomposes the microstructural morphology into large-sized, regional and detailed features, and then separately characterizes or reproduces these morphological features

step by step. This hierarchical strategy can greatly reduce the difficulty of 2D-to-3D morphology integration. In contrast, the single-level approach attempts to capture or generate all morphological features in one step, which greatly increases the difficulty of 2D-to-3D morphology integration. Even for the simple example in Case 1, the single-level approach is not able to generate 3D morphologically-similar microstructure samples. Therefore, the hierarchical strategy is the only choice for the proposed method that uses non-casual data templates to characterize and reconstruct porous microstructures.

The proposed hierarchical approach is then carried out to reconstruct 3D microstructures from the 2D exemplars. For each 2D exemplar, a Gaussian image pyramid with three levels is built for it, as shown in Figure 10. Following the procedure explained in Algorithm 1, SINN-based microstructure characterization is conducted to approximate the 3D morphological statistics at multiple scales. And then, 3D microstructure samples are hierarchically generated by using this multi-level characterization, as explained in Algorithm 3. The parameter setting of hierarchical characterization and multi-level reconstruction are summarized in Table 1. A group of thirty 3D samples is produced, and representative reconstruction results are shown in Figure 12. Obviously, the reconstructed microstructures become more and more visually appealing from the low level to the high level.

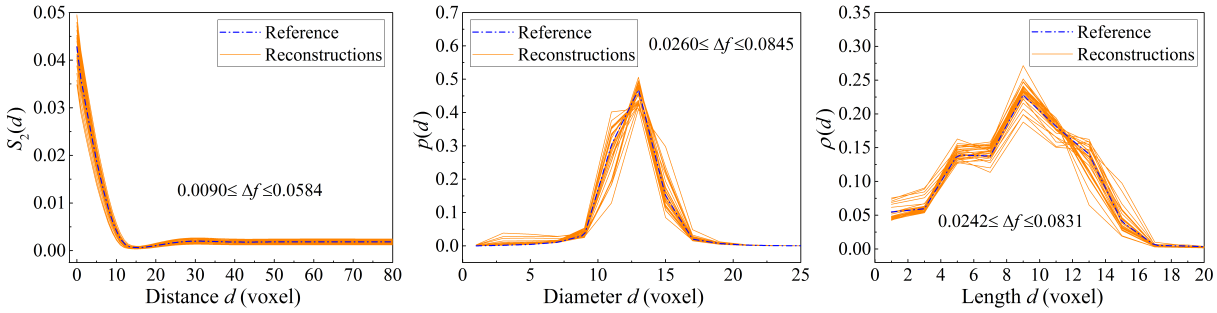

(a) Two-point correlation function (b) Pore size distribution (c) Chord length distribution

Figure 13: Comparisons of morphological descriptors between the reference and the reconstructed microstructures.

The reconstruction quality is assessed by comparing morphological descriptors extracted from the reference and reconstructed microstructures. The results of two-point correlation function $S_2(d)$, pore size distribution $p(d)$ and chord length distribution $\rho(d)$ are provided in Figure 13, which quantitatively measure random microstructures in aspects of statistical characteristics, pore size and pore connectivity, respectively. It is understandable for stochastic microstructure reconstruction that the descriptor curves of reconstructed samples fluctuate around the reference curve. The average reconstruction errors (measured by Δf in Eq. (31)) are all less than 5.00%, which confirms the statistical equivalence between the reference and reconstructed microstructures. Both the low porosity and the regular pore geometry exiting in the 2D exemplars are well preserved by the 3D reconstructed microstructure samples. What's more, the large-scale correlations (see Figure 13 a) that far exceed the scope of data templates (see Table 1) are also accurately captured, which demonstrates the effectiveness of the proposed hierarchical method in 2D-to-3D microstructure reconstruction.

4.2. Case 2: Porous ceramic with orientated cylindrical pores

The second case is a porous alumina ceramic produced by an extrusion method. As can be seen in Figure 14, there are oriented cylindrical pores inside this ceramic with pore space taking up around 17.50% of the bulk volume. It is well-known that pore geometry is an important factor in the preparation of porous ceramics with satisfactory properties [55]. Generally, it is very challenging to reconstruct 3D anisotropic microstructures from 2D exemplars, because parameter settings (such as the data template size) for different directions are needed to be carefully determined. To capture the anisotropic property of this porous ceramic, representative cross-sections on three orthogonal planes are selected as the 2D exemplars for 3D microstructure reconstruction, as shown in the rightmost column in Figure 14.

To compactly characterize this anisotropic microstructure, Gaussian image pyramids with three levels are built for these 2D exemplars in Figure 14, based on which three sets of SINN models are trained to learn morphological statistics at different length scales. Following the procedures explained in Algorithm 3, 3D microstructure samples are generated in a three-level reconstruction manner by using the hierarchical SINN-based characterization. As shown in Figure 15, two representative reconstruction results are provided. As more morphology details are added

to the 3D constructed samples from the low level to the high level, the reconstruction results become more and more visually close to the original 2D exemplars.

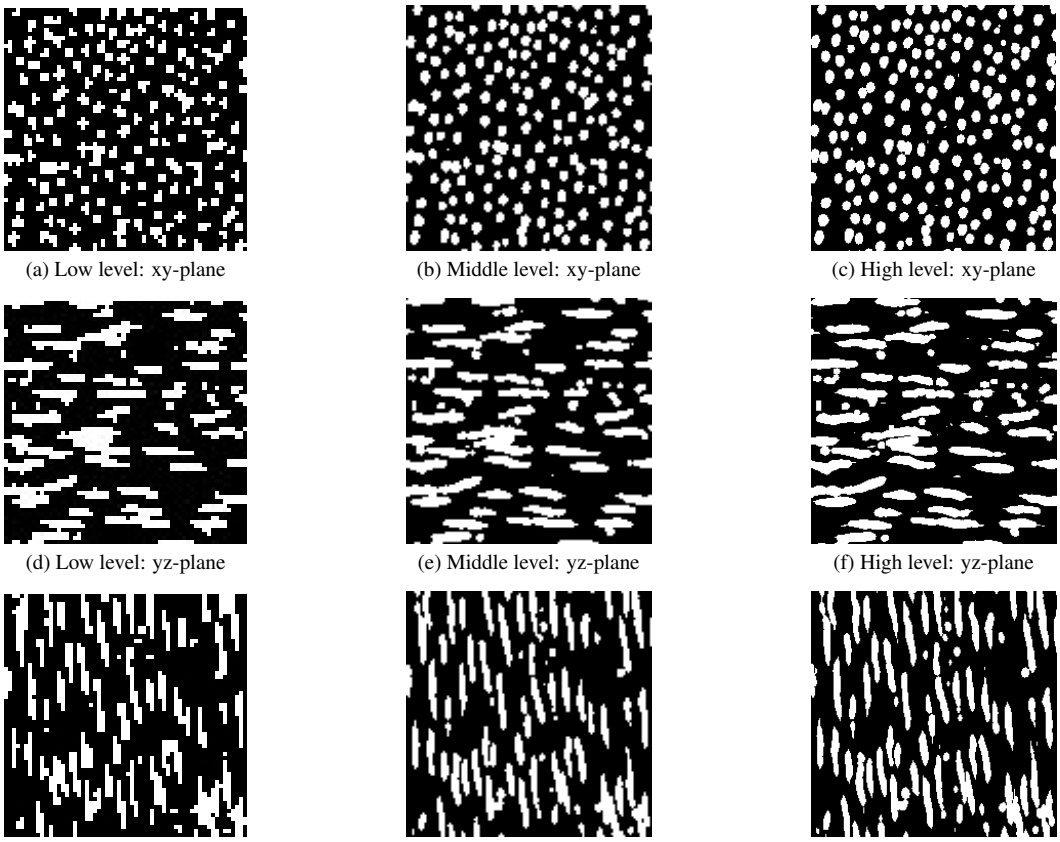

(a) Low level: xy-plane (b) Middle level: xy-plane (c) High level: xy-plane

(d) Low level: yz-plane (e) Middle level: yz-plane (f) High level: yz-plane

(g) Low level: zx-plane (h) Middle level: zx-plane (i) High level: zx-plane

Figure 14: Gaussian image pyramids with three levels: (a), (d) and (g) are the low-level images (60×60 pixels); (b), (e) and (h) are the middle-level images (120×120 pixels); (c), (f) and (i) are the high-level images (the original 2D exemplars with 240×240 pixels).

Morphological descriptors are used to quantify the discrepancy between the reference and the reconstructed microstructures, as shown in Figure 16. To characterize microstructural anisotropy, two-point correlation functions $S_2(d)$ are computed separately in different directions, as can be seen in Figure 16 a-c respectively. Besides, lineal path function $L(d)$, chord length distribution $\rho(d)$ and pore size distribution $p(d)$ are also used to assess reconstruction quality in terms of pore size, pore shape and pore connectivity, and the results are plotted in Figure 16 e-g respectively. For all these morphological descriptors, the reference curves are located at the centers of the variation ranges of reconstruction curves, with average errors Δf less than 5.00%. Therefore, the 3D reconstructed samples can be considered statistically equivalent to the reference microstructure in aspects of pore anisotropy and pore geometry.

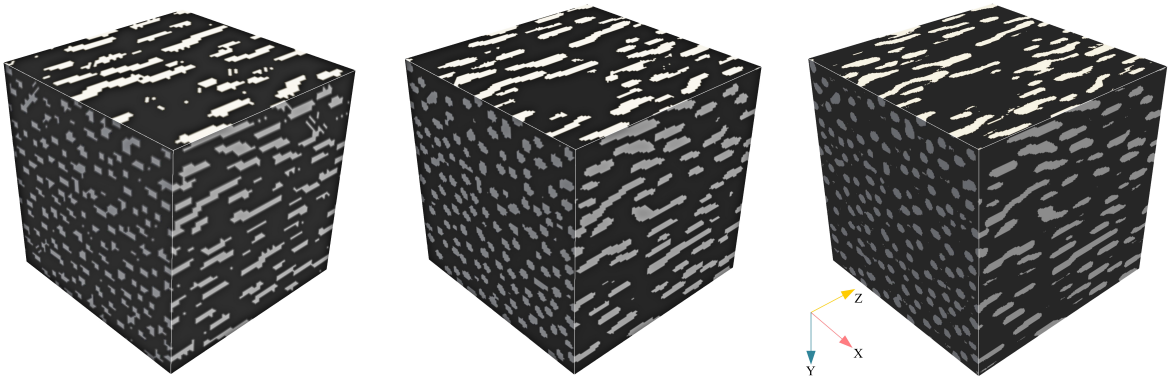

(a) Low level: sample I (b) Middle level: sample I (c) High level: sample I

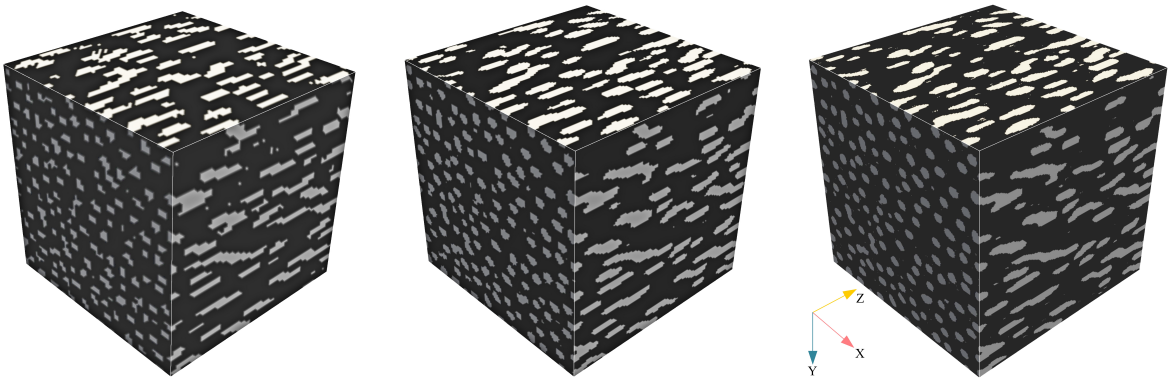

(d) Low level: sample II (e) Middle level: sample II (f) High level: sample II

Figure 15: Hierarchical microstructure reconstruction with three levels: (a) and (c) are the low-level results (60×60×60 voxels); (b) and (e) are the middle-level results (120×120× 120 voxels); (c) and (f) are the high-level results (the final 3D reconstructed samples with 240×240×240 voxels).

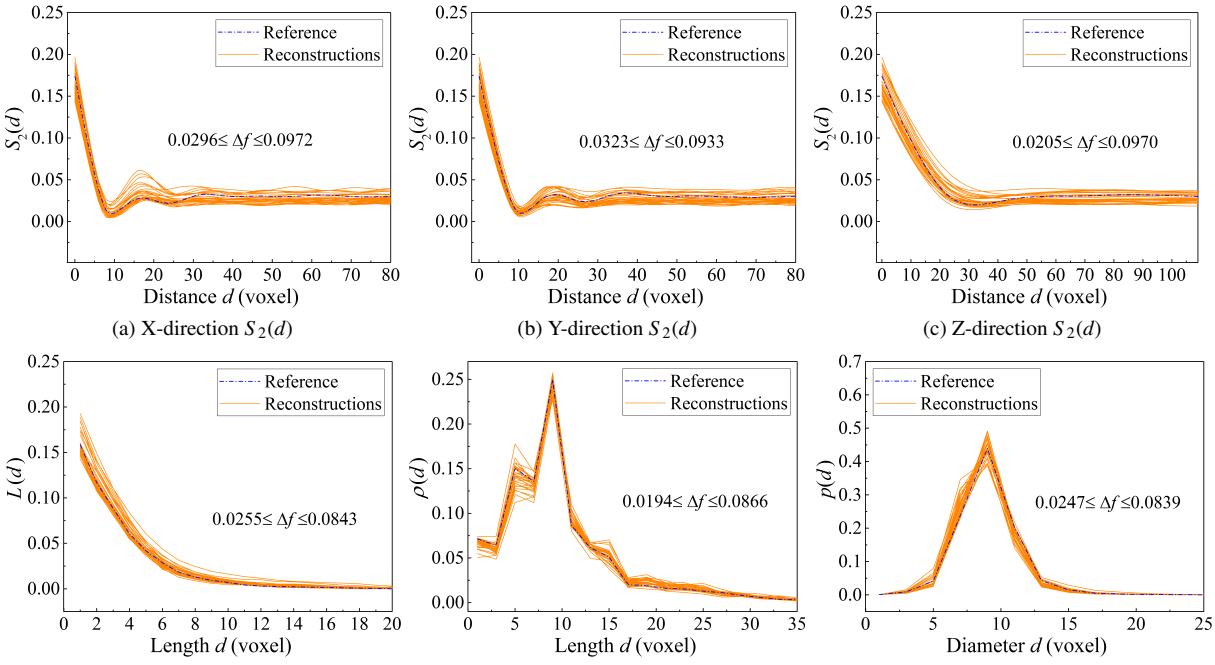

(a) X-direction $S_2(d)$ (b) Y-direction $S_2(d)$ (c) Z-direction $S_2(d)$

(d) Lineal path function (e) Chord length distribution (d) Pore size distribution

Figure 16: Comparisons of morphological descriptors between the reference and reconstructed microstructures.

4.3. Case 3: Mesoporous silica with isotropic pore system

Mesoporous silica with an isotropic pore system is selected as the third testing case. The pore space and the solid silica occupy around 42.50% and 57.50% of the entire volume respectively. The available 2D slices have a small size, so we select four representative slices and stitch them together as the only 2D exemplar for 3D microstructure reconstruction, as shown in Figure 17c. The high porosity, complicated pore geometry and long-distance pore connectivity of this typical porous medium can pose a huge challenge to the proposed hierarchical 2D-to-3D reconstruction method.

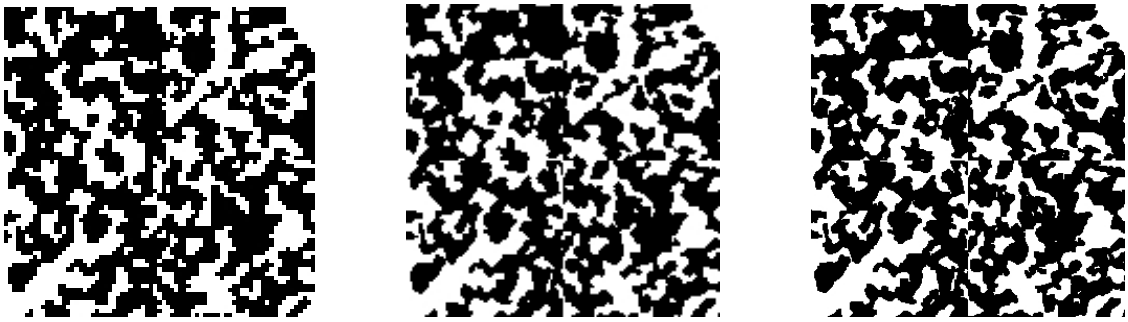

(a) Low-level image (b) Middle-level image (c) High-Level image

Figure 17: A Gaussian image pyramid with three levels: (a) The low-level image (75×75 pixels); (b) The middle-level image (150×150 pixels); (c) The high-level image (the original 2D exemplar with 300×300 pixels).

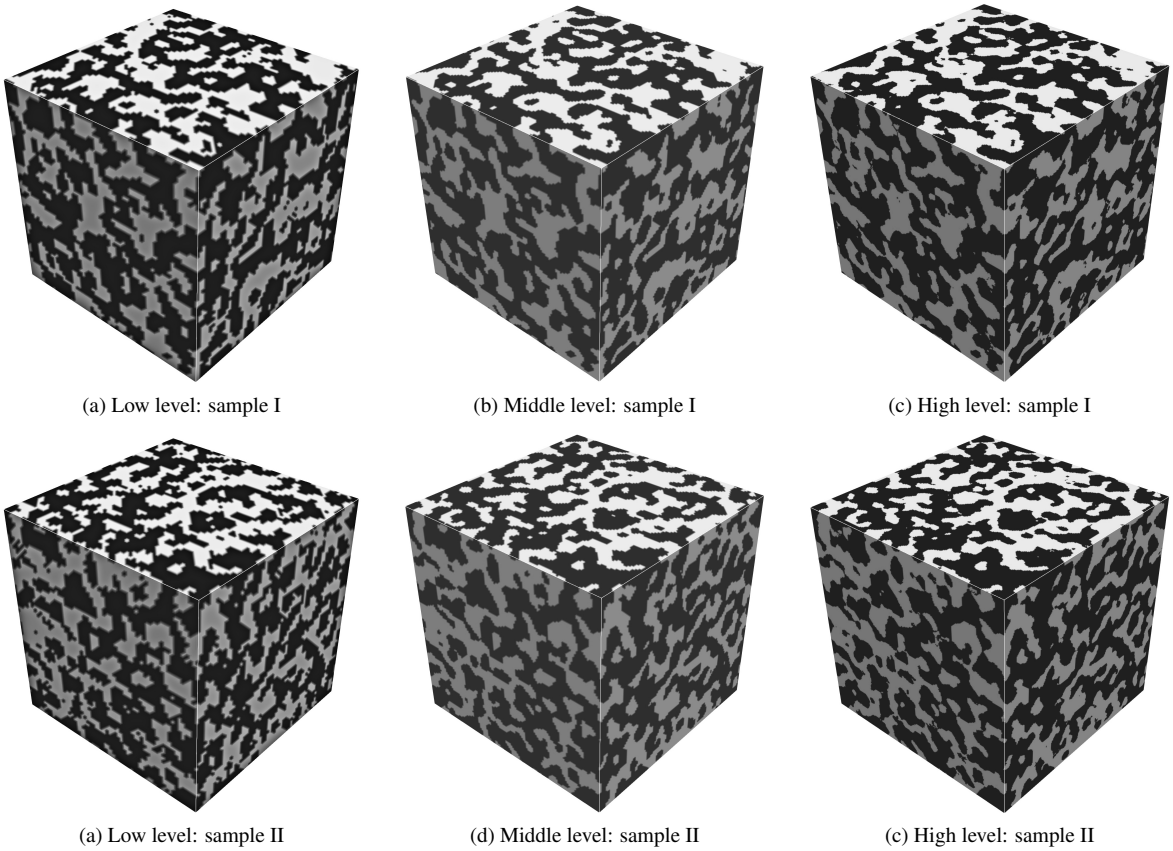

(a) Low level: sample I (b) Middle level: sample I (c) High level: sample I

(a) Low level: sample II (d) Middle level: sample II (c) High level: sample II

Figure 18: Hierarchical microstructure reconstruction with three levels: (a) and (d) are the low-level reconstruction results (60×60×60 voxels); (b) and (e) are the middle-level reconstruction results (120×120×120 voxels); (c) and (f) are the high-level reconstruction results (the final 3D reconstructed samples with 240×240×240 voxels).

Due to the isotropic property of this porous silica, the 2D morphological statistics on different planes can be assumed equivalent. Therefore, only one set of SINN models is trained to statistically characterize the 2D image

pyramids in Figure 17. The obtained machine learning-based characterization is sufficient for 3D microstructure reconstruction by using the proposed method. Two representative reconstruction results are given in Figure 18, from which one can see that the 3D reconstructed microstructures become morphologically close to the 2D exemplar as more microstructural details are added to the reconstruction.

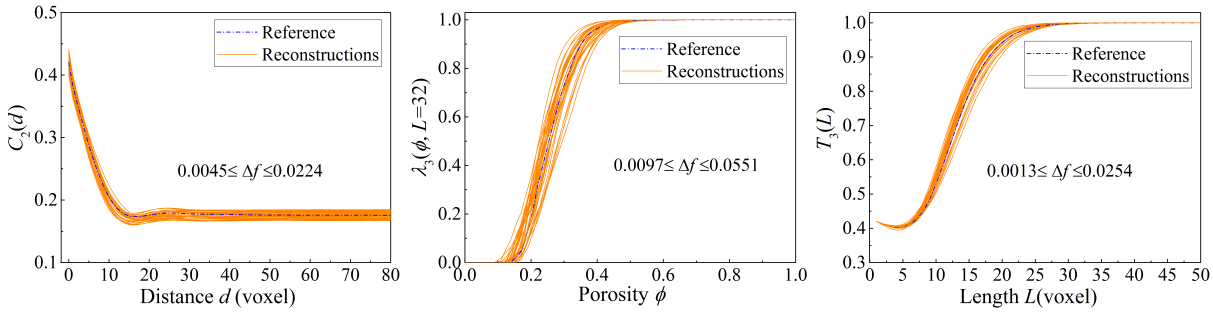

(a) Two-point cluster correlation function (b) Local percolation probabilities (c) Total fraction of percolation cells

Figure 19: Comparisons of morphological descriptors between the reference and reconstructed microstructures.

To evaluate the reconstruction quality, morphological descriptors are computed for the reference and reconstructed microstructures, including two-point cluster correlation function $C_2(d)$, local percolation probability $\lambda_3(\phi, L = 32)$ and total fraction of percolating cells $T_3(L)$. These descriptors are the common indicators to measure pore geometry and pore connectedness inside porous media, and the results are plotted in Figure 19. By comparison, each reference descriptor curve lies in the middle of the varying region of the reconstruction descriptors, and the average reconstruction errors measured by Δf are all less than 3.50%. More importantly, the reference and reconstruction descriptors also well match each other in long distances or at large length scales, as shown in Figure 19 a and c. These results demonstrate that the proposed hierarchical reconstruction method is able to generate well-connected porous microstructures from a few 2D thin sections.

4.4. Case 4: Mesoporous silica with anisotropic pore system

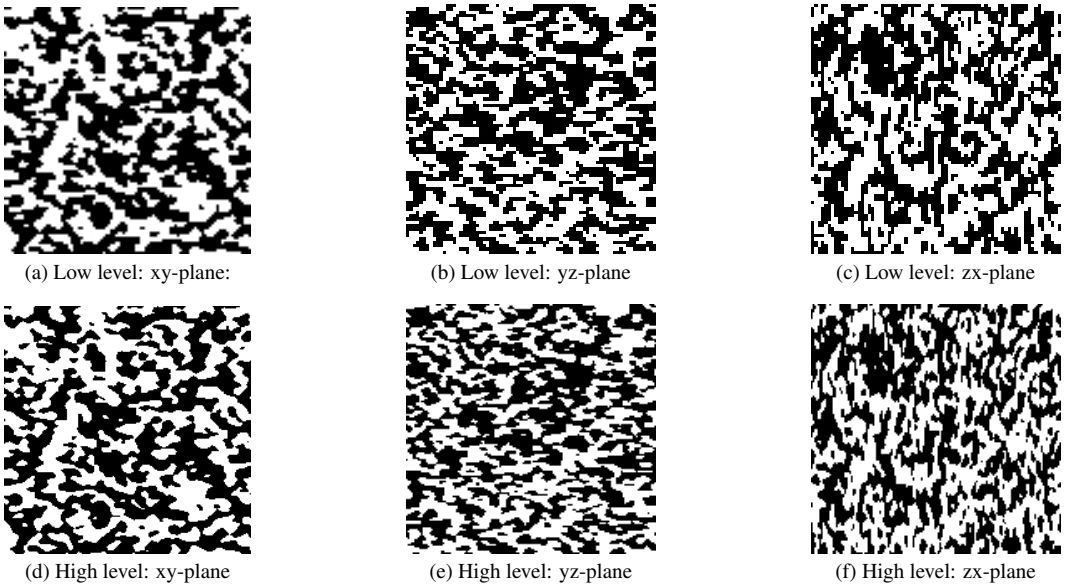

(a) Low level: xy-plane: (b) Low level: yz-plane (c) Low level: zx-plane

(d) High level: xy-plane (e) High level: yz-plane (f) High level: zx-plane

Figure 20: Gaussian image pyramids with two levels: (a), (b) and (c) are the low-level images (100×100 pixels); (d), (e) and (f) are the high-level images (the original 2D exemplars with 200×200 pixels).

Mesoporous silica with an anisotropic pore system is selected as the fourth typical case to test the proposed method. The pore space takes up approximately 51.00% of the bulk volume. Its pore network system is well-connected over a long distance, and the microstructural characteristics in different directions are greatly distinct

from each other. This testing case can pose a huge challenge to the proposed 2D-to-3D microstructure reconstruction method in capturing anisotropic characteristics and long-distance pore connectivity. As shown in the bottom line in Figure 20, representative cross-sectional images on three orthogonal planes are chosen as the 2D exemplars for 3D microstructure reconstruction.

The original 2D exemplars have a relatively low resolution, so Gaussian image pyramids with two levels are built for them, as shown in Figure 20. Following the procedure described in Algorithm 1, SINN models are separately trained to statistically characterize the 2D morphology patterns in different directions. The parameters of statistical characterization and stochastic reconstruction are listed in Table 1. A group of thirty 3D microstructure samples is generated by using the SINN-based characterization, and three representative samples are shown in Figure 21. The high-level reconstructed samples inherit the microstructural features from the low-level results, and they become morphologically realistic as more microstructural details are added to them.

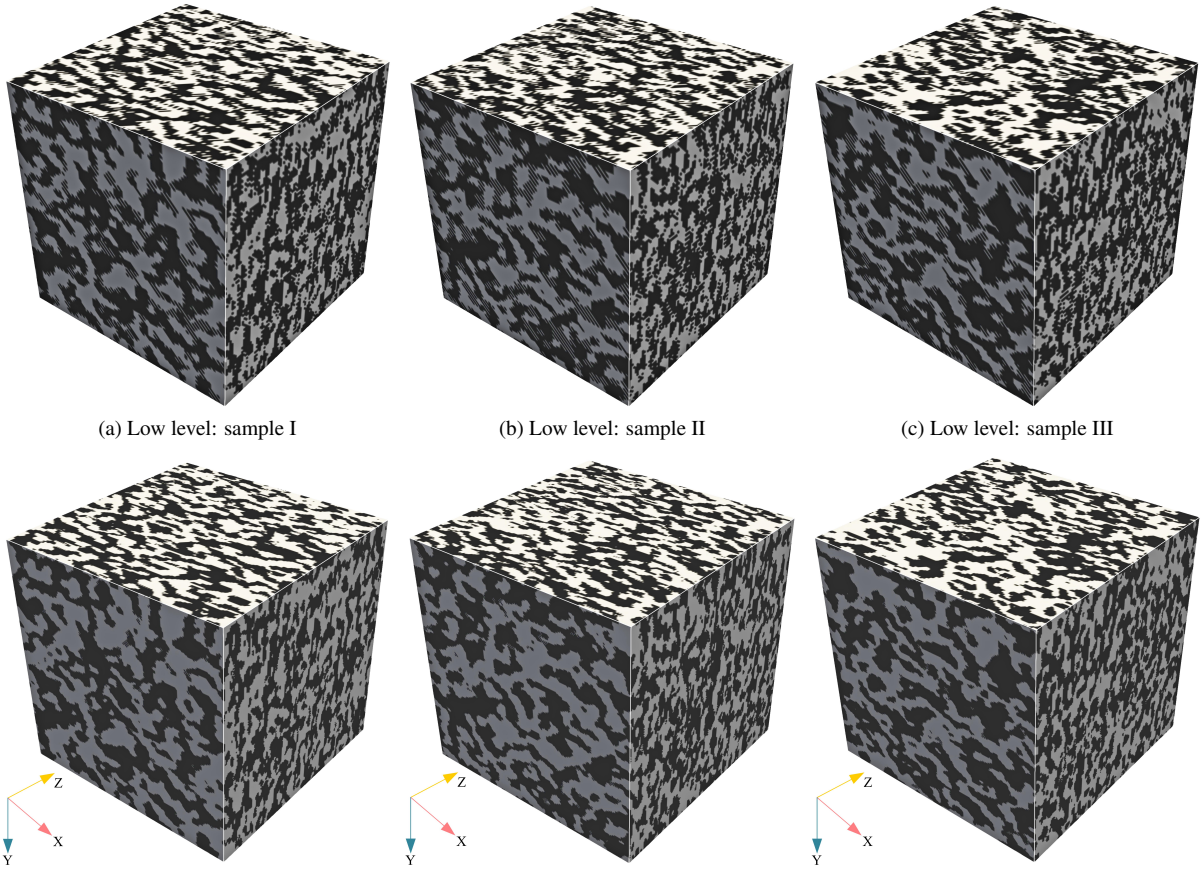

(a) Low level: sample I (b) Low level: sample II (c) Low level: sample III

(d) High level: sample I (e) High level: sample II (f) High level: sample III

Figure 21: The SINN-based hierarchical microstructure reconstruction with two levels: (a), (b) and (c) are the low-level reconstruction results (100×100×100 voxels); (d), (e) and (f) are the middle-level reconstruction results (the final 3D reconstructed samples with 200×200×200 voxels).

To evaluate the reconstruction quality, morphological descriptors are extracted from the 3D reference and reconstructed microstructures, including the total fraction of percolation fraction $T(L)$ and geometrical tortuosity τ_g. As the commonly used indicators of pore percolation degree, both $T(L)$ and τ_g can be separately computed in three orthogonal directions, and the results are provided in Figure 22. The reconstruction descriptor values just fluctuate around the reference descriptors with small errors (measured by Δf in Eq. (32)), which is normal for stochastic microstructure reconstruction. The good matches between the descriptors extracted from the reconstructed and reference microstructures indicate that both the long-distance pore connectivity and the anisotropic characteristics are well captured by the proposed 2D-to-3D microstructure reconstruction method.

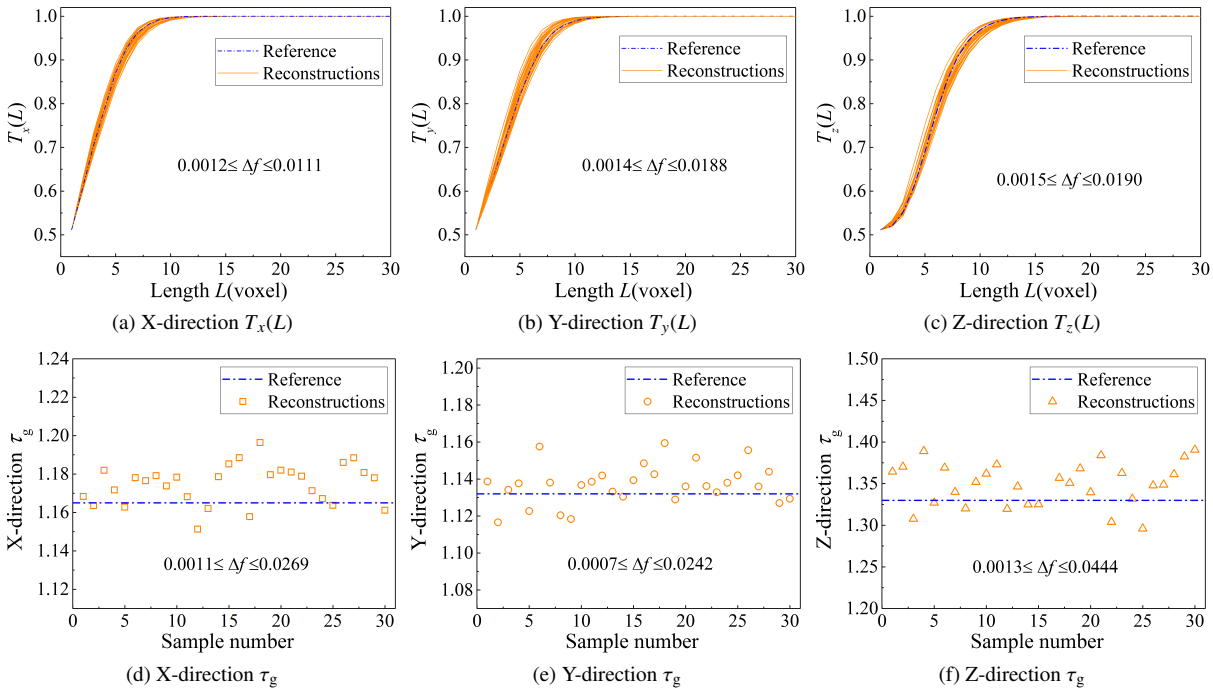

(a) X-direction $T_x(L)$ (b) Y-direction $T_y(L)$ (c) Z-direction $T_z(L)$

(d) X-direction τ_g (e) Y-direction τ_g (f) Z-direction τ_g

Figure 22: Comparisons of morphological descriptors between the reference and the SINN-based reconstructed microstructures.

As shown in Figure 23, the GAN-based method [39] is adopted to generate 3D microstructures from 2D cross-sectional images. It should be noted that only the high-level 2D images in Figure 20 are used as the training images. Appearance inspection shows that the 3D reconstructed microstructures are morphologically similar to the 2D exemplars. Morphological descriptors are then extracted for quantitative assessment of reconstruction quality, and the results are plotted in Figure 24. Both $T(L)$ and τ_g are effective descriptors to represent pore percolation degree, and they are separately computed in three axial directions to characterize microstructural anisotropy. On the whole, the GAN-based method exhibits good performance in capturing long-distance connectivity and anisotropic characteristics of the pore network system. Compared to the SINN-based method, it seems that the GAN-based method tends to generate porous microstructure samples with a smaller variance. However, the microstructures generated by the GAN-based method are not completely equivalent to the real ones, which can be seen from the slightly lower curves of $T_x(L)$ and $T_z(L)$ in Figure 23, as well as the slightly higher values of Y-direction τ_g and Z-direction τ_g.

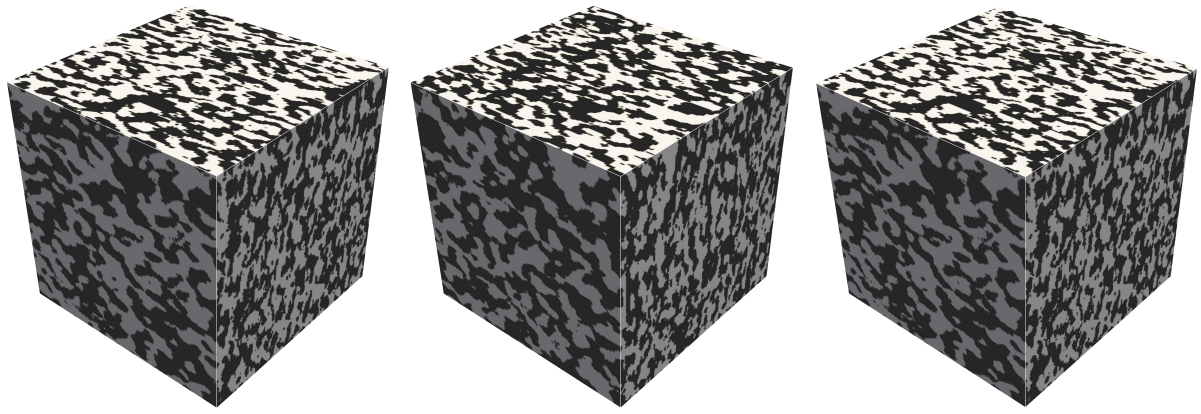

(a) Reconstructed sample I (b) Reconstructed sample II (c) Reconstructed sample III

Figure 23: The GAN-based microstructure reconstruction (200×200×200 voxels).

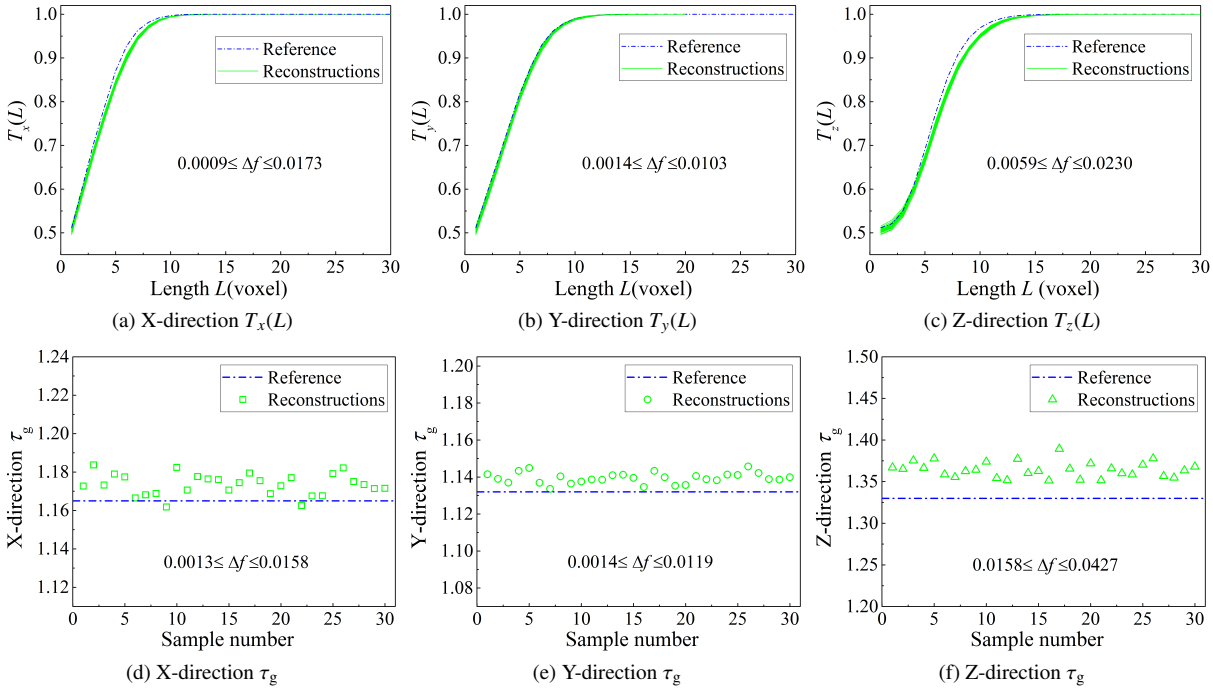

(a) X-direction $T_x(L)$ (b) Y-direction $T_y(L)$ (c) Z-direction $T_z(L)$

(d) X-direction τ_g (e) Y-direction τ_g (f) Z-direction τ_g

Figure 24: Comparisons of morphological descriptors between the reference and the GAN-based reconstructed microstructures.

Computational cost is an important index to assess the effectiveness of microstructure reconstruction methods. Here, both the proposed SINN-based method and the GAN-based method are run on the same desktop computer (CPU: Intel(R) Core(TM) i7-6700 3.41GHz; Memory: 64.0 GB). The average time cost to train a set of SINN models is around 36.5 minutes, while it takes about 1889.8 minutes to train a reliable GAN model. As to the reconstruction speed, the GAN-based method can rapidly generate a 3D microstructure sample with a size of 200×200×200 in 18.9 seconds, but the proposed SINN-based method needs to spend 762.8 seconds to accomplish this task. Both the properly trained SINN model and GAN model can be stored for repeated usage, but the former is completely free to generate the 3D microstructure samples of arbitrary sizes. Besides, the SINN models possess good interpretability by integrating morphological statistics into neural networks, while the GAN model works in a black-box manner.

4.5. Case 5: Porous rock with long-distance pore connectivity

The final case is a natural porous rock called Fontainebleau sandstone, which is often used as the benchmark for porous media research [56]. The porosity of this Fontainebleau sandstone sample is around 24.50%, and pore bodies with irregular geometry are connected to form a long-range percolating network. As shown in the rightmost column in Figure 25, representative 2D thin sections on three orthogonal planes are selected as the 2D exemplars for 3D microstructure reconstruction. Due to the irregular pore geometry and the long-distance pore connectivity, it is challenging for the proposed method to reproduce 3D microstructure samples that are geometrically and topologically equivalent to the 2D exemplars.

To compactly characterize the large-scale microstructural features, Gaussian image pyramids with three levels are built for the 2D exemplars on orthogonal planes, as can be seen in Figure 25. Three sets of SINN models are separately trained to approximate the morphological statistics at multiple length scales, and corresponding hyper-parameters are listed in Table 1. Following the procedure described in Algorithm 1, a group of thirty 3D samples is stochastically reconstructed, and two representative results are shown in Figure 26. Visual inspection indicates that the high-level 3D reconstructed samples are analogous to the 2D exemplars in terms of morphological patterns.

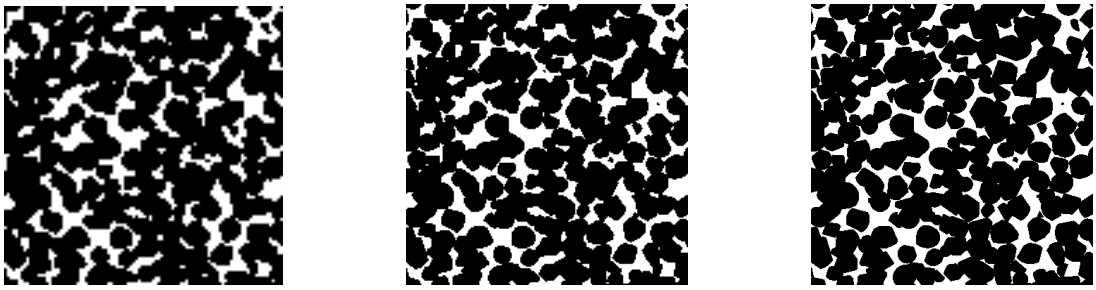

(a) Low level: xy-plane (a) Middle level: xy-plane (c) High level: xy-plane

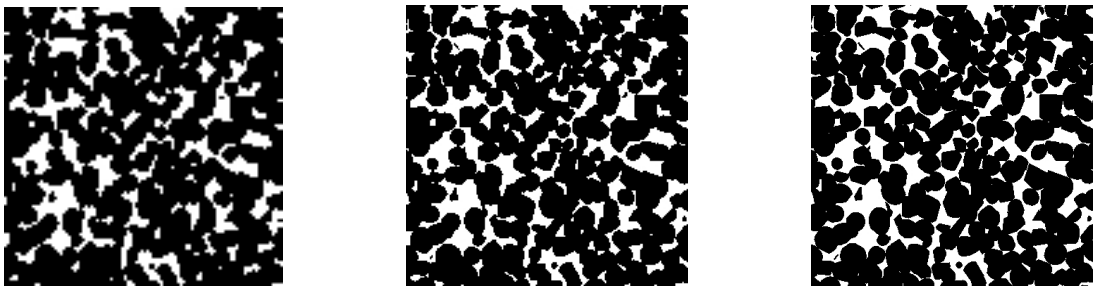

(d) Low level: yz-plane (e) Middle level: yz-plane (f) High level: yz-plane

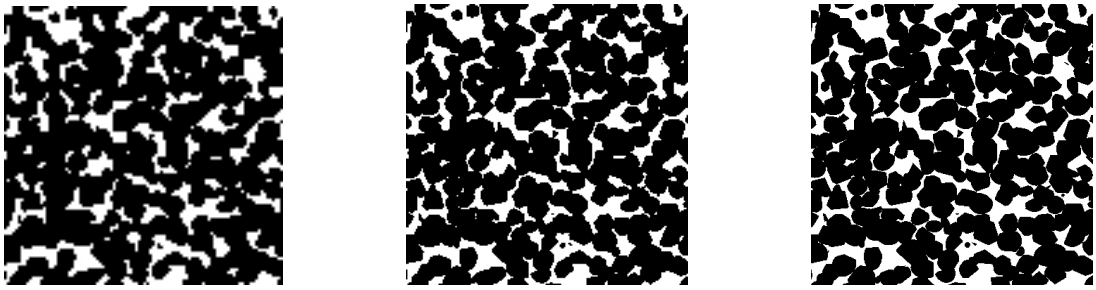

(g) Low level: zx-plane (h) Middle level: zx-plane (i) High level: zx-plane

Figure 25: Gaussian image pyramids with three levels: (a), (d) and (g) are the low-level images (100×100 pixels); (b), (e) and (h) are the middle-level images (200×200 pixels); (c), (f) and (i) are the high-level images (the original 2D exemplars with 400×400 pixels).

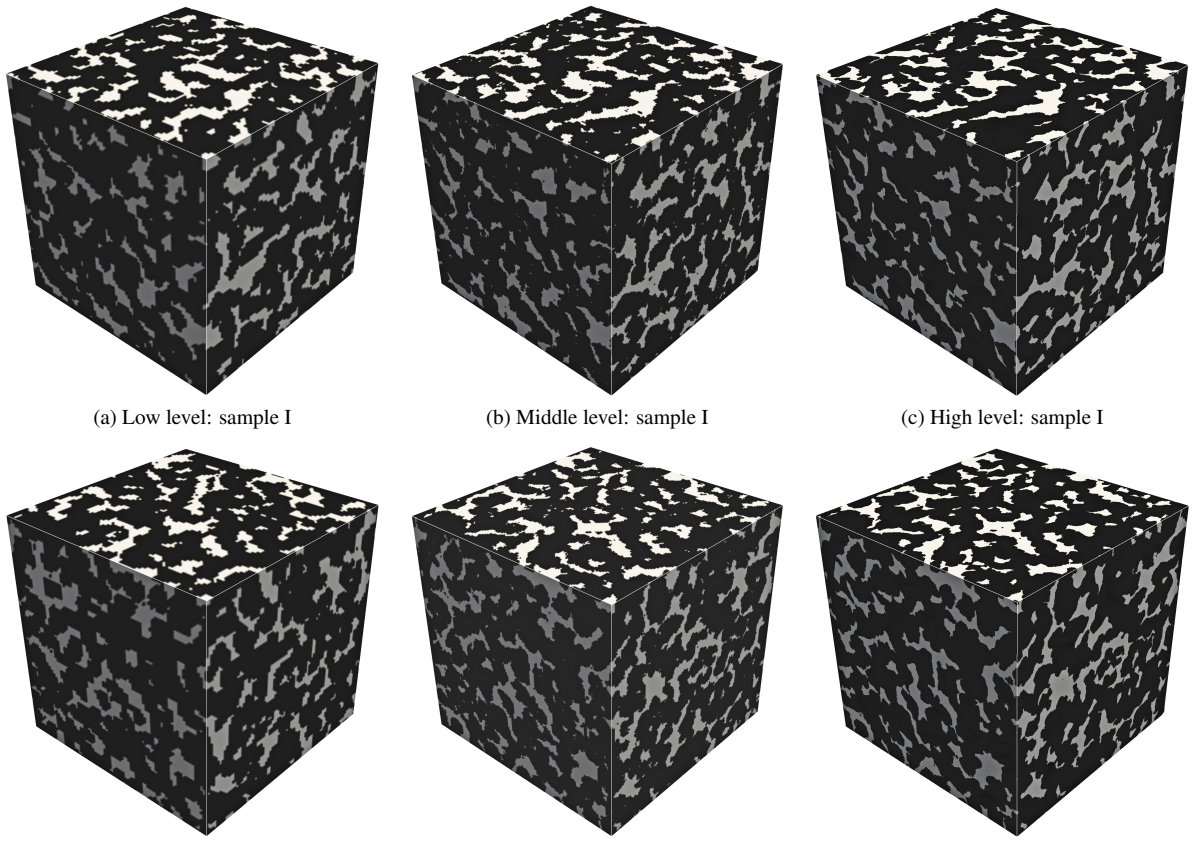

(a) Low level: sample I (b) Middle level: sample I (c) High level: sample I

(d) Low level: sample II (e) Middle level: sample II (f) High level: sample II

Figure 26: The SINN-based hierarchical microstructure reconstruction with three levels: (a) and (d) are the low-level reconstruction results (80×80×80 voxels); (b) and (e) are the middle-level reconstruction results (160×160×160 voxels); (c) and (d) are the high-level reconstruction results (the final 3D reconstructed samples with 320×320×320 voxels).

The reconstruction quality is assessed by comparing the morphological descriptors that are extracted from the reference and reconstructed microstructures. Here, geometrical tortuosity τ_g, pair connectivity function $H(d)$ and total fraction of percolating cells $T_3(L)$ are used to quantitatively characterize long-distance connectivity of pore channels, and the results are plotted in Figure 27. The descriptors extracted from reconstructed samples just slightly fluctuate around the reference values/curves, with the relative errors smaller than 3.20%. The small discrepancy between the reference and reconstructed microstructures indicates the equivalence between them, and it also confirms the effectiveness of the proposed 2D-to-3D reconstruction method in generating well-connected porous media.

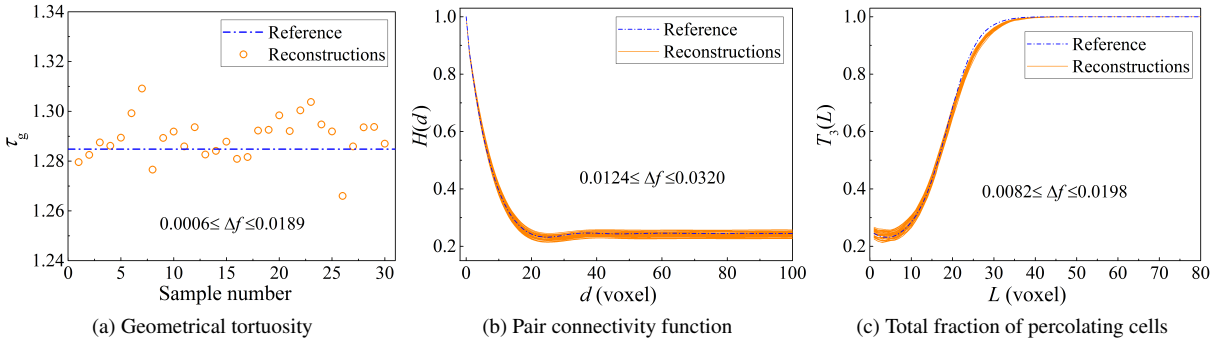

(a) Geometrical tortuosity (b) Pair connectivity function (c) Total fraction of percolating cells

Figure 27: Comparisons of morphological descriptors between the reference and the SINN-based reconstructed microstructures.

The GAN-based method [39] is also applied to generate 3D microstructure samples for this case, as shown in Figure 28. Here, only the high-level images in Figure 25 are used to train the GAN model. Obviously, the morpho-

logical patterns existing in the 2D exemplars are satisfyingly preserved by the reconstructed 3D microstructures. To quantitatively characterize the long-distance connectivity within the pore network system, three morphological descriptors including τ_g, $H(d)$ and $T_3(L)$ are extracted from both the reference and reconstructed microstructures, as plotted in Figure 29. In general, the GAN-based method shows excellent performance in generating well-connected porous microstructures, which can be demonstrated by the good matches between the reconstructed and real microstructures in terms of the three morphological descriptors. Compared with the proposed SINN-based method, it seems that the GAN-based method tends to generate microstructures with slightly larger errors (measured by Δf in Figure 27 and 29), which can be due to that the GAN-based reconstructed microstructures are smaller than the representative size.

(a) Reconstructed sample I (b) Reconstructed sample II (c) Reconstructed sample III

Figure 28: The GAN-based microstructure reconstruction (200×200×200 voxels).

As to the computational cost, the developed SINN-based method is directly compared with the GAN-based method by running them on the same desktop computer (CPU: Intel(R) Core(TM) i7-6700 3.41GHz; Memory: 64.0 GB). The time cost to train a GAN model is up to 2596.5 minutes, while the training process of SINN models can be completed within 51.5 minutes. The SINN-based method requires 780.2 seconds to generate a 3D microstructure sample with a size of $200 \times 200 \times 200$, and the GAN-based method can achieve this task in 19.3 seconds. Although both the trained SINN and GAN models can be stored for repeated usage, the SINN-based method is much more flexible to reproduce 3D microstructures of arbitrary sizes. Additionally, the GAN model is poorly interpretable, while the SIIN model can be considered as an implicit representation of morphological statistics.

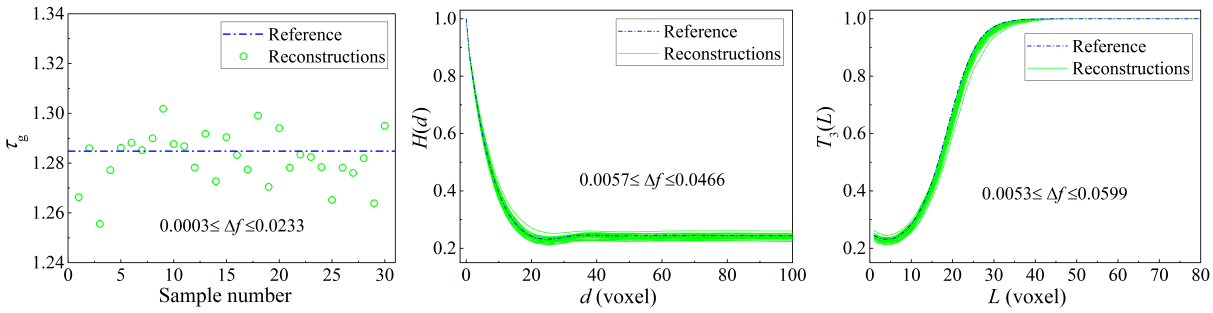

(a) Geometrical tortuosity (b) Pair connectivity function (c) Total fraction of percolating cells

Figure 29: Comparisons of morphological descriptors between the reference and the GAN-based reconstructed microstructures.

5. Transport properties

There are various types of transport phenomena occurring inside porous media, such as (multiphase) fluid permeation, mass diffusion, electrical conduction and heat transfer, and they are all intrinsically linked to microstructural characteristics [15]. Transport properties are known as functions of the geometry and topology of porous media [6]. Therefore, the assessment of microstructure reconstruction quality should also take account of physical properties, not just comparing morphology patterns. Here, different types of transport properties are numerically evaluated for the 3D reference and reconstructed microstructures used in Section 4, to further assess the statistical equivalence between them. The studied transport properties include absolute permeability, electrical conductance, thermal conductivity, effective diffusion coefficient and relative permeability.

5.1. Case 1: Electrical conductance

For testing case 1 in Section 4.1, electrical conduction occurring inside porous media is numerically resolved by using the voxel-based finite volume method (FVM) [57]. The solid phase is assumed to be homogeneous with electrical conductivity equal to $\sigma_0 = 0.0001$ S/m, while the pore space is saturated with air whose electrical conductivity is assumed to be $\frac{1}{100}\sigma_0$. A constant electrical potential difference is applied to the inlet and outlet faces of the cubic digital microstructure, while the other four faces are set as insulating walls [15]. Driven by the constant potential difference, electric charges are transmitted through the 3D digital microstructures, where image voxels are directly used as the volume elements for FVM simulation. When the steady state is achieved (as shown in Figure 30a and b), the effective electrical conductivity σ_{eff} can be computed according to Ohm's law.

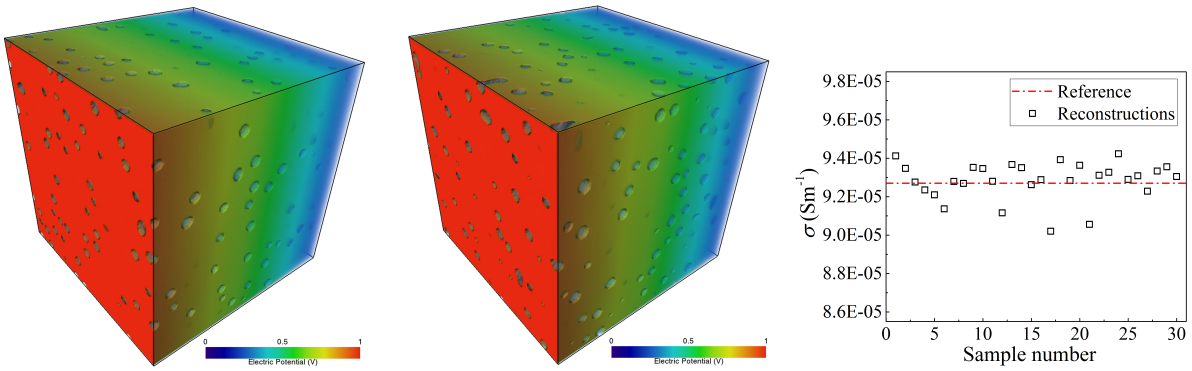

(a) Sample I: electric potential field (b) Sample II: electric potential field (c) Electrical conductivity

Figure 30: Numerical evaluation of electrical formation factor for the porous microstructures in Section 4.1: (a) and (b) are the electric potential fields at the steady state; (c) Electrical conductivity results.

For each porous medium sample, FVM simulations are separately carried out in three orthogonal directions, and the mean value is used as the final result of effective electrical conductivity σ_{eff}. As shown in Figure 30c, the effective electrical conductivity values of thirty reconstructed samples randomly scatter around the straight line that represents the reference value, and the average value of σ_{eff} computed from reconstructed samples is also very close to the reference value. It indicates that the 3D reconstructed microstructures are statistically equivalent to the real microstructure in terms of electrical conduction. The accurate maintenance of effective electrical conductivity further verifies the effectiveness of the proposed method in 2D-to-3D microstructure reconstruction.

5.2. Case 2: Thermal conductivity

With regards to testing case 2 in Section 4.2, thermal conductivity is numerically computed for the 3D reference and reconstructed microstructures through finite volume simulation of heat flow [57]. Heat transfer happening inside porous media is dominated by the solid phase, because the thermal conductivity of solid matrix is much higher than that of air in pore space [58, 15]. In our simulations, heat transfer only occurs in the solid phase with thermal conductivity $\lambda_0 = 1$ W/(m·K), and the pore space filled with air is assumed thermal insulating. A constant temperature difference is applied between the input face (298 K) and the output face (273 K) of the cubic porous media sample, and the other four faces are set as thermal insulating walls. It should be mentioned that the image voxels are directly used as the basic elements for FVM simulation. FVM simulation iteratively runs until the steady state is reached (as shown in Figure 31a-c), and then effective thermal conductivity λ_{eff} can be evaluated according to Fourier's law.

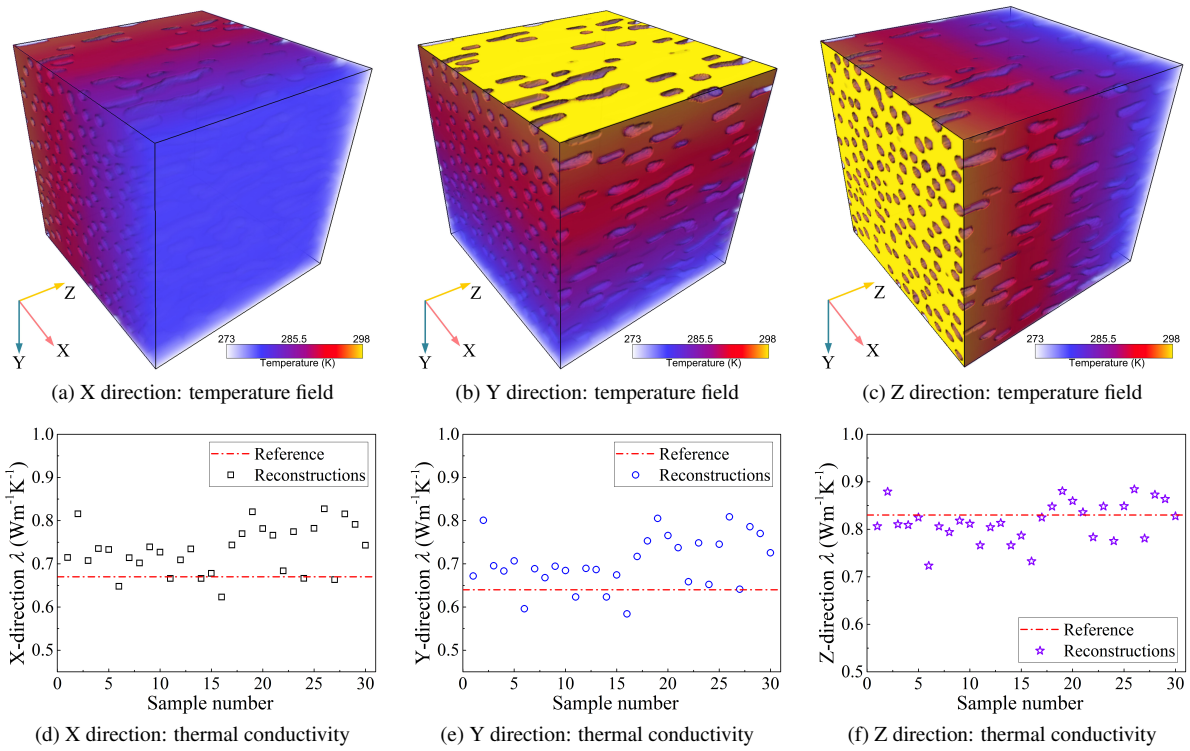

(a) X direction: temperature field (b) Y direction: temperature field (c) Z direction: temperature field

(d) X direction: thermal conductivity (e) Y direction: thermal conductivity (f) Z direction: thermal conductivity

Figure 31: Numerical evaluation of thermal conductivity for the porous microstructures in Section 4.2: (a), (b) and (c) are the temperature fields at the steady state; (d), (e) and (f) are the effective thermal conductivity values in different directions.

Effective thermal conductivities of these anisotropic porous microstructures are separately evaluated in three orthogonal directions, and the results are recorded in Figure 31d-f respectively. In X and Y directions, the λ_{eff} values computed from most of the reconstructed samples are slightly larger than the reference values; while in the Z direction, the opposite situation occurs. Such a discrepancy between the reconstructed and reference microstructures could be due to a number of reasons, such as 2D exemplar selection, data template size, and SINN model training. Compared to isotropic microstructure reconstruction, it is usually much more difficult to accurately generate anisotropic microstructures from 2D exemplars. But the remarkable thing is that the average values of λ_{eff} computed from thirty reconstructed samples are close to the reference values in three directions. In other words, the thermal conductivity and transport anisotropy of the real microstructure are primarily preserved by the reconstructed samples, which further demonstrates the physical equivalence between them.

5.3. Case 3: Relative permeability

For the 3rd testing case in Section 4.3, relative permeability is numerically evaluated for the 3D reference and reconstructed microstructures, where the lattice Boltzmann method (LBM) [59, 60] is used to simulate two-phase (oil-water) flow at the pore scale. The Shan–Chen LBM framework is adopted here by treating the image grid as the regular lattice, where two fluid phases are represented by two separate probability density functions. The contact angle is set to 24.60°, and the viscosity ratio, interfacial tension and density ratio between the two fluid phases are set to 1.360, 0.324 and 1.250 respectively. An external force is applied to both fluid phases along the flow direction, and periodic boundary conditions are added to the inlet and the outlet faces. The other four surfaces of the cubic digital microstructure are added with solid walls, and no-slip boundary conditions are used on the fluid-solid interfaces. Driven by the constant body force, the mixed fluid with the desired wetting saturation starts to pass through the porous microstructure from the inlet to the outlet. When the final steady state is reached, the relative permeabilities for the wetting and non-wetting phases can be computed following the adaption of Darcy's law [60], as illustrated in Figure 32a and b.

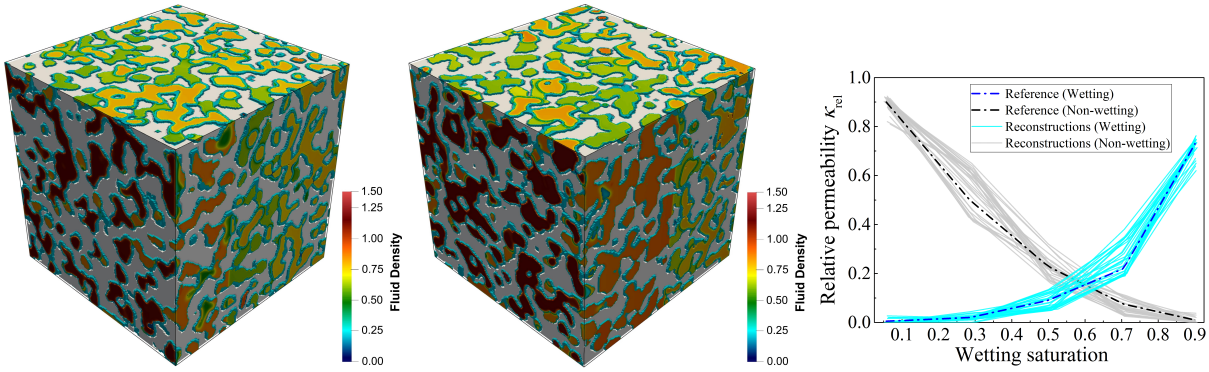

(a) Sample I: fluid density field (b) Sample II: fluid density field (c) Relative permeability

Figure 32: Numerical evaluation of relative permeability for the porous microstructures in Section 4.3: (a) The steady-state density fields of two-phase flow when the wetting saturation is 0.285; (b) The steady-state density fields of two-phase flow when the wetting saturation is 0.498; (c) The relative permeability results.

For multiphase flow in porous media, relative permeability is defined as the ratio of the effective permeability of the phase to the absolute permeability, which is a dimensionless measure. Relative permeability κ_{rel} is often expressed as a function of wetting saturation. As shown in Figure 35c, the relative permeability results corresponding to the 3D reconstructed and reference microstructures are plotted. The reference values of κ_{rel} are represented by two dot-dash curves for the wetting and non-wetting fluids, while the relative permeabilities of the reconstructed samples are represented by the solid curves. Clearly, the reference curves are completely located inside the variation ranges of the reconstruction curves, and they are also very close to the 'average curves' of the reconstruction curves. For stochastic reconstruction, it is reasonable that the reconstructed samples have transport properties fluctuating around the reference values but sharing an average characteristic. The good agreements between these curves not only indicate the statistical equivalence between the 3D reconstructed and reference microstructures in aspects of transport behaviors of two-phase flow, but also verify the effectiveness of the proposed method in generating 3D well-connected porous microstructures.

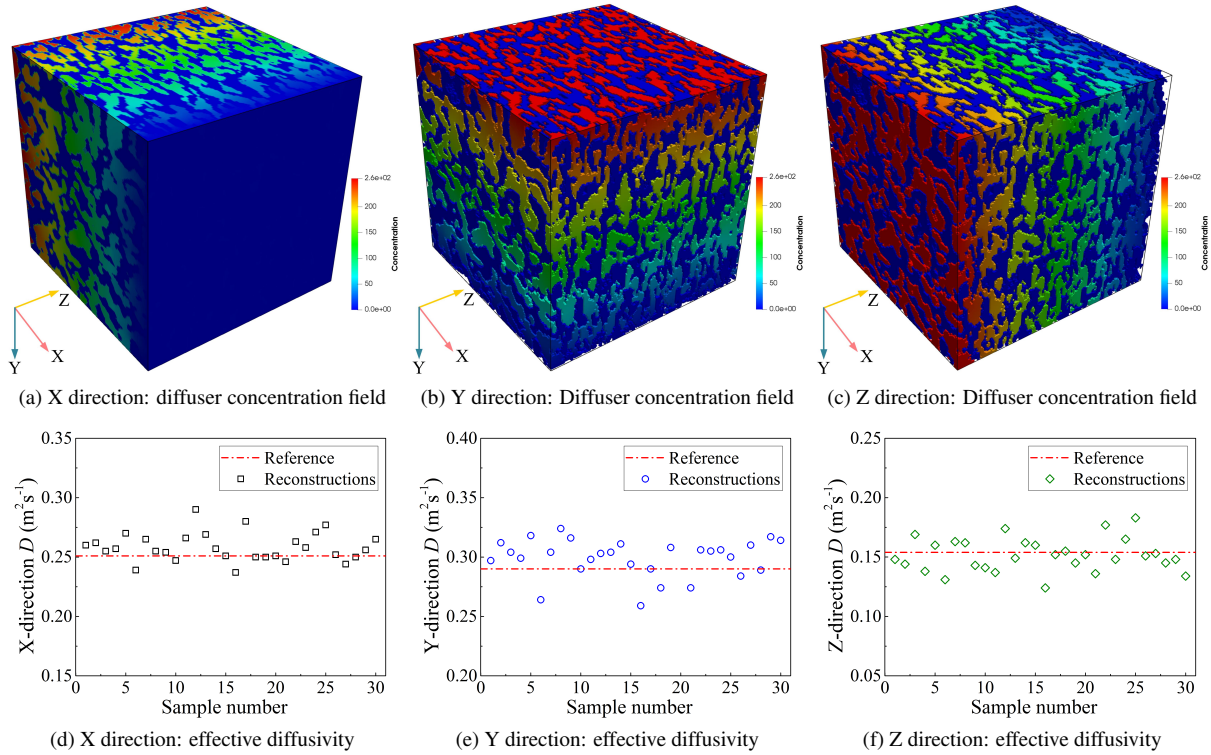

(a) X direction: diffuser concentration field (b) Y direction: Diffuser concentration field (c) Z direction: Diffuser concentration field

(d) X direction: effective diffusivity (e) Y direction: effective diffusivity (f) Z direction: effective diffusivity

Figure 33: Numerical evaluation of effective diffusivity for the porous microstructures generated by the SINN-based method in Section 4.4: (a), (b) and (c) are the concentration fields at the steady state; (d), (e) and (f) are the effective diffusivity values in different directions.

5.4. Case 4: Effective diffusivity

For testing case 4 in Section 4.4, effective diffusivity values of the 3D reference and reconstructed microstructures are numerically evaluated via finite difference method (FDM) [61, 62, 63]. A diffusing gas with diffusivity of $D_0 = 1.00\text{m}^2/\text{s}$ is typically used as the probe to mimic molecular diffusion inside the pore space of 3D digital microstructures, where the voxel grid is directly treated as the finite-difference grid. A constant concentration difference is applied between the inlet and outlet faces of cubic microstructures, while the other four faces parallel to the diffusional flow direction are set as solid walls for the isolation purpose. When the diffuser concentration field reaches its steady state (as shown in Figure 33a-c and Figure 34a-c), the effective diffusivity D_{eff} of a porous medium can be evaluated according to Fick's law.

Due to the anisotropic characteristics of this porous medium, FDM simulations of pore-scale diffusion are separately conducted in three principle directions for each digital microstructure. As shown in Figure 33d-f, directional D_{eff} values of thirty samples (that are generated by the proposed SINN-based method) just randomly scatter around the reference lines, and the overall average values are also very close to the reference values. Such good agreements demonstrated that the 3D virtual microstructures are statistically equivalent to the real microstructure in terms of effective diffusivity and anisotropic attributes. This test example further verifies the effectiveness of the proposed SINN-based method in generating 3D well-connected porous microstructures from 2D cross-sectional images.

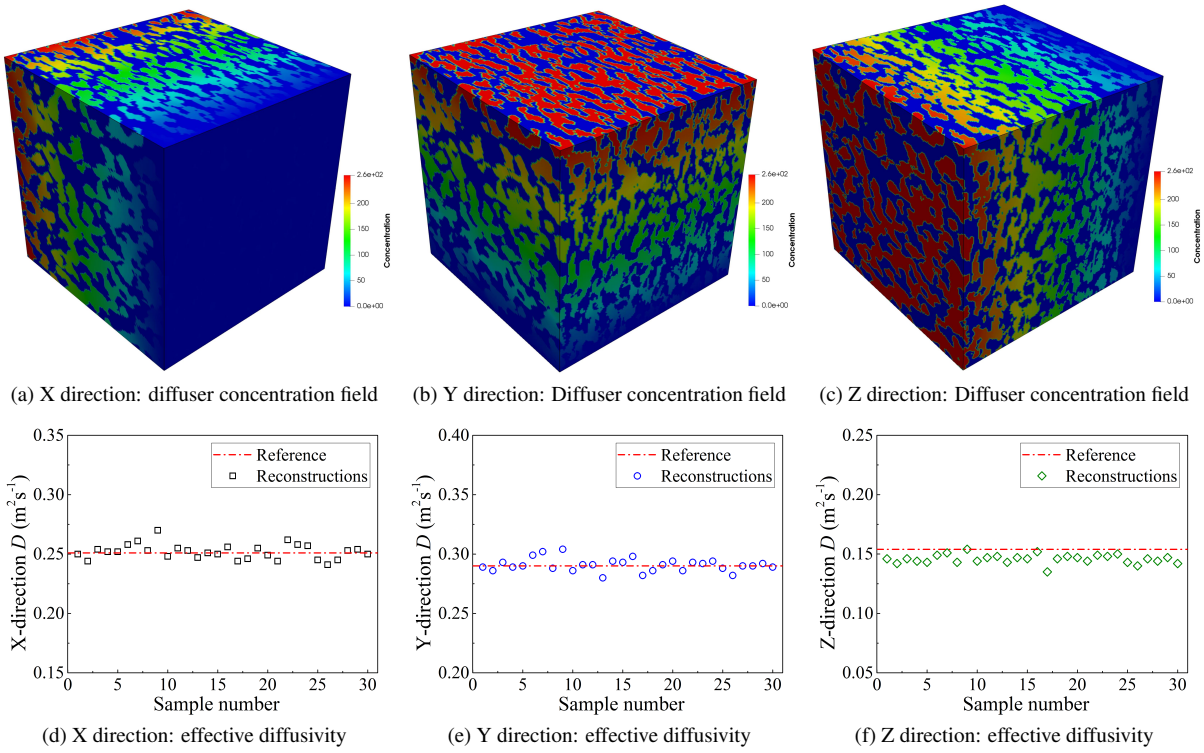

(a) X direction: diffuser concentration field (b) Y direction: Diffuser concentration field (c) Z direction: Diffuser concentration field

(d) X direction: effective diffusivity (e) Y direction: effective diffusivity (f) Z direction: effective diffusivity

Figure 34: Numerical evaluation of effective diffusivity for the porous microstructures generated by the GAN-based method in Section 4.4: (a), (b) and (c) are the concentration fields at the steady state; (d), (e) and (f) are the effective diffusivity values in different directions.

Besides, numerical evaluation of effective diffusivity is also carried out for the porous microstructures generated by the GAN-based method in Section 4.4, as shown in Figure 34d-f. Compared to the proposed SINN-based method, the GAN-based method tends to generate 3D samples with more stable values of effective diffusivity. In general, these 3D porous microstructures are physically equivalent to the real microstructure in terms of effective diffusivity, except for slightly small values of D_{eff} in the Z direction.

5.5. Case 5: Absolute permeability

The porous medium sample in Section 4.5 (Case 5) possesses a well-connected pore network system, therefore, we perform pore-scale simulations of single-phase flow to assess the transport equivalence between the 3D reference and reconstructed microstructures. Lattice Boltzmann method (LBM) [64, 5, 65] with the Bhatnagar-Gross-Krook collision term is adopted here to mimic fluid flow passing through cubic digital microstructures,

where the voxel grid directly serves as the regular lattice. A constant pressure difference is applied to the inlet and outlet surfaces, and solid walls are added to the other four faces for the isolation purpose. Besides, the no-slip boundary condition is set at the fluid-solid interface. Driven by the constant pressure gradient with a small value, fluid flow (with a low Reynolds number) steadily passes through porous media samples, as illustrated in Figure 35a and b. And absolute permeability κ can then be evaluated according to Darcy's law.

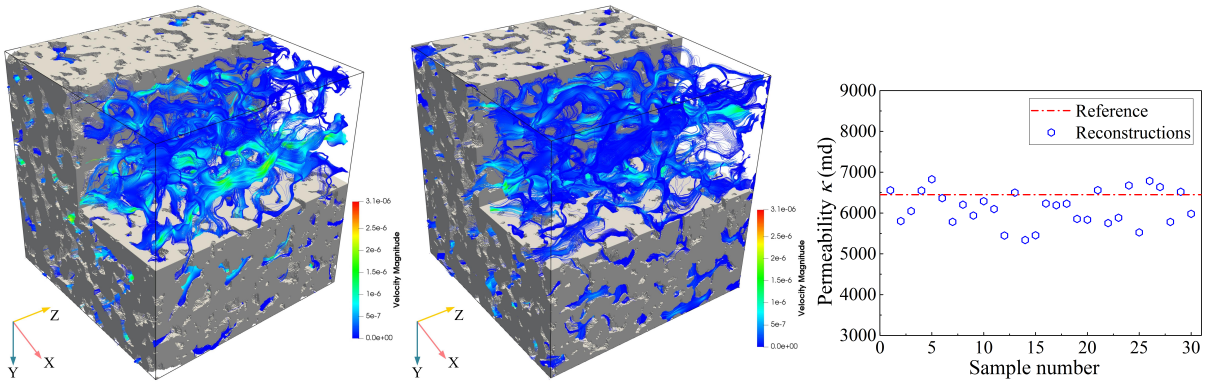

(a) Sample I: flow velocity field (b) Sample II: flow velocity field (c) Absolute permeability

Figure 35: Numerical evaluation of absolute permeability for the porous microstructures generated by the SINN-based method in Section 4.5: (a) and (b) are the steady-state velocity fields of single-phase flow; (c) The absolute permeability results.

For each porous microstructure, LBM simulations of single-phase flow are separately conducted in three principle directions, and the mean value of three directional permeabilities is referred to as the final result. Absolute permeability results of the 3D reference and reconstructed microstructures are numerically evaluated. As recorded in Figure 35c, the permeability values of thirty samples (that are generated by the proposed SINN-based method) just randomly fluctuate around the reference line, with the overall average value slightly smaller than the reference one. There are many factors responding to such reconstruction error, including 2D exemplar selection, data template size and SINN model training. But it should be highlighted that the hydrodynamic conductivity of the reference microstructure is primarily preserved by the reconstructed microstructures, which demonstrates the transport equivalence between them.

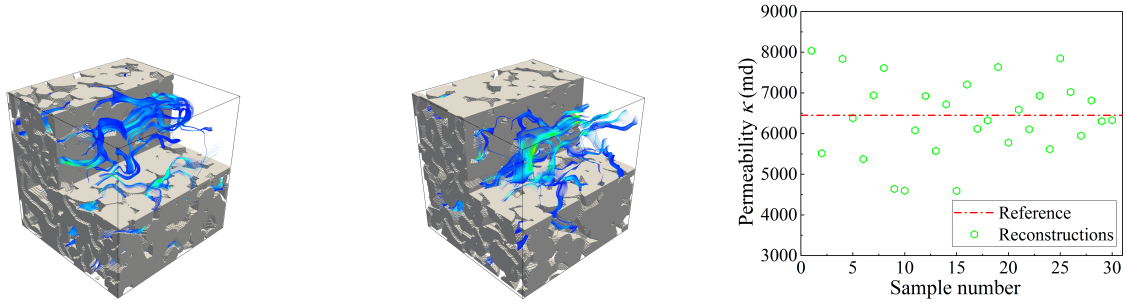

(a) Sample I: flow velocity field (b) Sample II: flow velocity field (c) Absolute permeability

Figure 36: Numerical evaluation of absolute permeability for the porous microstructures generated by the GAN-based method in Section 4.5: (a) and (b) are the steady-state velocity fields of single-phase flow; (c) The absolute permeability results.

As shown in Figure 36, numerical evaluation of absolute permeability is also carried out for the porous microstructures generated by the GAN-based method in Section 4.5. The permeability values recorded in Figure 36c fluctuate much stronger than that in Figure 35c, but the average permeability value is close to the reference value. Generally, the GAN-based method exhibits a satisfying performance in generating 3D well-connected porous microstructures by preserving absolute permeability.

6. Discussion and conclusions

6.1. Discussion

Machine/deep learning has been incorporated to reconstruct random microstructures in many studies, due to its powerful capacity in analyzing complex data and exploring hidden rules. We think an effective machine learning-based reconstruction method should wrestle with small data, accuracy, speed and interpretability. In this work, a hierarchical 2D-to-3D microstructure reconstruction method is developed by adhering to the above principles:

- **Small data:** A machine learning-based reconstruction method that requires large training data just goes against the reason for and the objective of stochastic microstructure reconstruction. The proposed method only requires one (isotropic) or several (anisotropic) 2D exemplar(s) with representative significance to serve as the training image(s). With the MRF assumption, the training images can be split into a large number of patches. Statistics-informed neural networks (SINN) are trained to learn morphological statistics from these patches. Such a modeling paradigm is to statistically characterize random media in a small-data regime.

- **Accuracy:** The existing machine learning-based reconstruction methods usually pay high attention to capturing the microstructural details, ignoring the importance of large-scale microstructural metrics to transport properties of porous media. The proposed method is biased toward the large-range correlations and long-distance connectivity of porous microstructures, by developing a hierarchical characterization approach and a multi-level reconstruction approach. Hierarchical characterization can separately embed the 2D morphological statistics at multiple scales into different SINN models, based on which multi-level reconstruction is able to reproduce 3D morphology patterns at different scales and successively add them into the same random field.

- **Speed:** If a stochastic reconstruction method cannot rapidly generate large numbers of microstructure samples, its practical value would be greatly discounted. The proposed method needs to train several sets of SINN models to statistically characterize 2D training images. The training processes of neural networks are very quick, and the obtained SINN models can be stored for repeated usage. The proposed method adopts the Gibbs sampler to generate new 3D microstructures of arbitrary sizes, and the reconstruction speed can be significantly accelerated by setting a large sampling ratio.

- **Interpretability:** Deep learning models usually work in a black-box manner. By contrast, the SINN models possess very good interpretability because they can be considered as the implicit representations of morphological statistics in the 2D training images at hierarchical levels. And the statistical equivalence between the 3D reconstructed microstructures and the 2D exemplars can also be clearly understood and explained.

Despite the above advantages, the hierarchical 2D-to-3D microstructure reconstruction method presented in this work is not flawless. Firstly, 2D slices are selected as the training images through a hand-picking procedure. How to identify the most representative 2D slices through a standard procedure is an important prerequisite for 3D microstructure reconstruction. Secondly, porous microstructures are assumed to be Markov random fields for statistical characterization, which may make the proposed method less effective for porous media with extremely strong heterogeneity. Thirdly, the 3D morphological statistics are inferred from the 2D CPDFs through a simple weighted average operation, which works well for isotropic microstructures. But for anisotropic microstructures, the weighting coefficients before the 2D CPDFs should be carefully determined. Finally, reconstruction efficiency can be dramatically lifted by setting a high sampling ratio but also greatly increasing the memory requirement for data processing, especially for reconstructing large-size 3D microstructures. Further investigations are required to solve the above problems, thereby improving the usability and effectiveness of the proposed method.

6.2. Conclusions

The main contribution of this work is to present a stochastic reconstruction method that can efficiently generate 3D well-connected porous microstructures of arbitrary sizes from one or several low-cost 2D exemplar(s) via *statistics-informed neural network (SINN)*. This work pays special attention to the large-range correlations and long- distance connectivity of porous microstructures by developing a hierarchical characterization approach and a multi-level reconstruction approach. The proposed method starts by constructing a Gaussian image pyramid for each 2D exemplar, aiming at compactly characterizing the large-scale microstructural metrics. Data events are collected from the Gaussian image pyramids, and then they serve as the training data to embed 2D morphological

statistics into feed-forward neural networks at multiple scales, which are referred to as SINNs in this study. A morphology integration scheme is specially used to infer the 3D morphological statistics from the pretrained SINN models at different length scales. Gibbs sampling is adopted to hierarchically reconstruct 3D microstructures by using multi-level 3D morphological statistics, where the large-scale, regional and local morphological patterns are statistically generated and successively added to the same 3D random field.

The new method is applied to a series of porous media with distinct morphology patterns, and the reconstruction quality is assessed by comparing the 3D reconstructed samples with the reference microstructures, in terms of morphological characteristics and transport properties. Various morphological descriptors are used to quantify the statistical informatics, geometrical metrics and topological attributes of porous microstructures; Transport phenomena, including electricity transmission, heat conduction, mass diffusion and fluid permeation, are numerically simulated to evaluate the transport properties of porous media. The comprehensive comparison shows excellent consistency, which confirms the statistical equivalence between the 3D reconstructed and the real microstructures. The proposed method is also efficient and flexible, and the balance between reconstruction speed and computation memory requirement can be adjusted by changing the sampling ratio. What's more, the proposed methods can be straightforwardly extended for the 2D-to-3D reconstruction of multi-phase porous microstructures.

Acknowledgements

The authors would like to acknowledge the support of the EPSRC grant: PURIFY ($EP/V000756/1$) and Swansea University Impact Fund, and we also would like to acknowledge the support of the Supercomputing Wales project, which is part-funded by the European Regional Development Fund (ERDF) via Welsh Government.

References

[1] Didier Bouvard, Jean-Marc Chaix, Rémi Dendievel, Arnaud Fazekas, JM Létang, G Peix, and Daniel Quenard. Characterization and simulation of microstructure and properties of eps lightweight concrete. *Cement and Concrete Research*, 37(12):1666–1673, 2007.

[2] Aly Ahmed. Compressive strength and microstructure of soft clay soil stabilized with recycled bassanite. *Applied Clay Science*, 104:27–35, 2015.

[3] Li Chen, Qinjun Kang, and Wenquan Tao. Pore-scale study of reactive transport processes in catalyst layer agglomerates of proton exchange membrane fuel cells. *Electrochimica Acta*, 306:454–465, 2019.

[4] Feihu Zhao, Johanna Melke, Keita Ito, Bert van Rietbergen, and Sandra Hofmann. A multiscale computational fluid dynamics approach to simulate the micro-fluidic environment within a tissue engineering scaffold with highly irregular pore geometry. *Biomechanics and Modeling in Mechanobiology*, 18(6):1965–1977, 2019.

[5] Jinlong Fu, Jiabin Dong, Yongliang Wang, Yang Ju, D Roger J Owen, and Chenfeng Li. Resolution effect: an error correction model for intrinsic permeability of porous media estimated from lattice boltzmann method. *Transport in Porous Media*, 132(3):627–656, 2020.

[6] Pierre Adler. *Porous media: geometry and transports*. Elsevier, 2013.

[7] Salvatore Torquato. *Random Heterogeneous Materials: Microstructure and Macroscopic Properties*, volume 16. Springer Science & Business Media, 2013.

[8] Carl Fredrik Berg. Permeability description by characteristic length, tortuosity, constriction and porosity. *Transport in Porous Media*, 103(3):381–400, 2014.

[9] Firat C Cetinbas, Rajesh K Ahluwalia, Nancy Kariuki, Vincent De Andrade, Dash Fongalland, Linda Smith, Jonathan Sharman, Paulo Ferreira, Somaye Rasouli, and Deborah J Myers. Hybrid approach combining multiple characterization techniques and simulations for microstructural analysis of proton exchange membrane fuel cell electrodes. *Journal of Power Sources*, 344:62–73, 2017.

[10] Yi Feng, Haiwu Zheng, Zhengang Zhu, and Fangqiou Zu. The microstructure and electrical conductivity of aluminum alloy foams. *Materials Chemistry and Physics*, 78(1):196–201, 2003.

[11] Giorgio Pia, Ludovica Casnedi, and Ulrico Sanna. Porous ceramic materials by pore-forming agent method: an intermingled fractal units analysis and procedure to predict thermal conductivity. *Ceramics International*, 41(5):6350–6357, 2015.

[12] Martin J Blunt, Branko Bijeljic, Hu Dong, Oussama Gharbi, Stefan Iglauer, Peyman Mostaghimi, Adriana Paluszny, and Christopher Pentland. Pore-scale imaging and modelling. *Advances in Water Resources*, 51:197–216, 2013.

[13] Bowen Liang, Anand Nagarajan, Hossein Ahmadian, and Soheil Soghrati. Analyzing effects of surface roughness, voids, and particle–matrix interfacial bonding on the failure response of a heterogeneous adhesive. *Computer Methods in Applied Mechanics and Engineering*, 346:410–439, 2019.

[14] Xiang Li, Zhanli Liu, Shaoqing Cui, Chengcheng Luo, Chenfeng Li, and Zhuo Zhuang. Predicting the effective mechanical property of heterogeneous materials by image based modeling and deep learning. *Computer Methods in Applied Mechanics and Engineering*, 347:735–753, 2019.

[15] Jinlong Fu, Hywel R Thomas, and Chenfeng Li. Tortuosity of porous media: Image analysis and physical simulation. *Earth-Science Reviews*, 212:103439, 2021.

[16] Yongfei Yang, Yingfang Zhou, Martin J Blunt, Jun Yao, and Jianchao Cai. Advances in multiscale numerical and experimental approaches for multiphysics problems in porous media. *Advances in Geo-Energy Research*, 5(3):233–238, 2021.

[17] Tianyu Huang, Zeliang Liu, CT Wu, and Wei Chen. Microstructure-guided deep material network for rapid nonlinear material modeling and uncertainty quantification. *Computer Methods in Applied Mechanics and Engineering*, 398:115197, 2022.

[18] Jinlong Fu, Shaoqing Cui, Song Cen, and Chenfeng Li. Statistical characterization and reconstruction of heterogeneous microstructures using deep neural network. *Computer Methods in Applied Mechanics and Engineering*, 373:113516, 2021.

[19] CLY Yeong and S Torquato. Reconstructing random media. ii. three-dimensional media from two-dimensional cuts. *Physical Review E*, 58(1):224, 1998.

[20] ZR Liang, CP Fernandes, FS Magnani, and PC Philippi. A reconstruction technique for three-dimensional porous media using image analysis and fourier transforms. *Journal of Petroleum Science and Engineering*, 21(3-4):273–283, 1998.

[21] Ramin Bostanabad, Anh Tuan Bui, Wei Xie, Daniel W Apley, and Wei Chen. Stochastic microstructure characterization and reconstruction via supervised learning. *Acta Materialia*, 103:89–102, 2016.

[22] Ramin Bostanabad, Wei Chen, and Daniel W Apley. Characterization and reconstruction of 3d stochastic microstructures via supervised learning. *Journal of Microscopy*, 264(3):282–297, 2016.

[23] Ruijin Cang, Hechao Li, Hope Yao, Yang Jiao, and Yi Ren. Improving direct physical properties prediction of heterogeneous materials from imaging data via convolutional neural network and a morphology-aware generative model. *Computational Materials Science*, 150:212–221, 2018.

[24] Jinlong Fu, Dunhui Xiao, Dongfeng Li, Hywel R Thomas, and Chenfeng Li. Stochastic reconstruction of 3d microstructures from 2d cross-sectional images using machine learning-based characterization. *Computer Methods in Applied Mechanics and Engineering*, 390:114532, 2022.

[25] Yang Ju, Jiangtao Zheng, Marcelo Epstein, Les Sudak, Jinbo Wang, and Xi Zhao. 3d numerical reconstruction of well-connected porous structure of rock using fractal algorithms. *Computer Methods in Applied Mechanics and Engineering*, 279:212–226, 2014.

[26] Wenliang Zhang, Lei Song, and Juanjuan Li. Efficient 3d reconstruction of random heterogeneous media via random process theory and stochastic reconstruction procedure. *Computer Methods in Applied Mechanics and Engineering*, 354:1–15, 2019.

[27] Jacques A Quiblier. A new three-dimensional modeling technique for studying porous media. *Journal of Colloid and Interface Science*, 98(1):84–102, 1984.

[28] Pål-Eric Øren and Stig Bakke. Process based reconstruction of sandstones and prediction of transport properties. *Transport in Porous Media*, 46(2):311–343, 2002.

[29] Hiroshi Okabe and Martin J Blunt. Prediction of permeability for porous media reconstructed using multiple-point statistics. *Physical Review E*, 70(6):066135, 2004.

[30] Alireza Hajizadeh, Aliakbar Safekordi, and Farhad A Farhadpour. A multiple-point statistics algorithm for 3d pore space reconstruction from 2d images. *Advances in Water Resources*, 34(10):1256–1267, 2011.

[31] Kejian Wu, Marinus IJ Van Dijke, Gary D Couples, Zeyun Jiang, Jingsheng Ma, Kenneth S Sorbie, John Crawford, Iain Young, and Xiaoxian Zhang. 3d stochastic modelling of heterogeneous porous media–applications to reservoir rocks. *Transport in Porous Media*, 65(3):443–467, 2006.

[32] Pejman Tahmasebi and Muhammad Sahimi. Reconstruction of three-dimensional porous media using a single thin section. *Physical Review E*, 85(6):066709, 2012.

[33] Xingchen Liu and Vadim Shapiro. Random heterogeneous materials via texture synthesis. *Computational Materials Science*, 99:177–189, 2015.

[34] Hongyi Xu, Dmitriy A Dikin, Craig Burkhart, and Wei Chen. Descriptor-based methodology for statistical characterization and 3d reconstruction of microstructural materials. *Computational Materials Science*, 85:206–216, 2014.

[35] Ming Yang, Anand Nagarajan, Bowen Liang, and Soheil Soghrati. New algorithms for virtual reconstruction of heterogeneous microstructures. *Computer Methods in Applied Mechanics and Engineering*, 338:275–298, 2018.

[36] Veeraraghavan Sundararaghavan and Nicholas Zabaras. Classification and reconstruction of three-dimensional microstructures using support vector machines. *Computational Materials Science*, 32(2):223–239, 2005.

[37] Yuzhu Wang, Christoph H Arns, Sheik S Rahman, and Ji-Youn Arns. Porous structure reconstruction using convolutional neural networks. *Mathematical Geosciences*, 50(7):781–799, 2018.

[38] Junxi Feng, Qizhi Teng, Bing Li, Xiaohai He, Honggang Chen, and Yang Li. An end-to-end three-dimensional reconstruction framework of porous media from a single two-dimensional image based on deep learning. *Computer Methods in Applied Mechanics and Engineering*, 368:113043, 2020.

[39] Steve Kench and Samuel J Cooper. Generating three-dimensional structures from a two-dimensional slice with generative adversarial network-based dimensionality expansion. *Nature Machine Intelligence*, 3(4):299–305, 2021.

[40] Ramin Bostanabad. Reconstruction of 3d microstructures from 2d images via transfer learning. *Computer-Aided Design*, 128:102906, 2020.

[41] Fan Zhang, Qizhi Teng, Honggang Chen, Xiaohai He, and Xiucheng Dong. Slice-to-voxel stochastic reconstructions on porous media with hybrid deep generative model. *Computational Materials Science*, 186:110018, 2021.

[42] Ting Zhang, Hongyan Tu, Pengfei Xia, and Yi Du. Reconstruction of porous media using an information variational auto-encoder. *Transport in Porous Media*, pages 1–25, 2022.

[43] Fan Zhang, Xiaohai He, Qizhi Teng, Xiaohong Wu, and Xiucheng Dong. 3d-pmrnn: Reconstructing three-dimensional porous media from the two-dimensional image with recurrent neural network. *Journal of Petroleum Science and Engineering*, 208:109652, 2022.

[44] Jiale Zhao, Mengdi Sun, Zhejun Pan, Bo Liu, Mehdi Ostadhassan, and Qinhong Hu. Effects of pore connectivity and water saturation on matrix permeability of deep gas shale. *Advances in Geo-Energy Research*, 6(1):54–68, 2022.

[45] Stan Z Li. *Markov random field modeling in image analysis*. Springer Science & Business Media, 2009.

[46] Sotiris B Kotsiantis, Ioannis Zaharakis, P Pintelas, et al. Supervised machine learning: A review of classification techniques. *Emerging artificial intelligence applications in computer engineering*, 160(1):3–24, 2007.

[47] Martin Fodslette Møller. A scaled conjugate gradient algorithm for fast supervised learning. *Neural Networks*, 6(4):525–533, 1993.

[48] Anders Krogh and Jesper Vedelsby. Neural network ensembles, cross validation, and active learning. *Advances in Neural Information Processing Systems*, 7, 1994.

[49] Daniel Svozil, Vladimir Kvasnicka, and Jiri Pospichal. Introduction to multi-layer feed-forward neural networks. *Chemometrics and Intelligent Laboratory Systems*, 39(1):43–62, 1997.

[50] Edward H Adelson, Charles H Anderson, James R Bergen, Peter J Burt, and Joan M Ogden. Pyramid methods in image processing. *RCA Engineer*, 29(6):33–41, 1984.

[51] Christopher M Bishop and Nasser M Nasrabadi. *Pattern recognition and machine learning*, volume 4. Springer, 2006.

[52] R Hilfer. Review on scale dependent characterization of the microstructure of porous media. *Transport in Porous Media*, 46(2):373–390, 2002.

[53] Shaoqing Cui, Jinlong Fu, Song Cen, Hywel R Thomas, and Chenfeng Li. The correlation between statistical descriptors of heterogeneous materials. *Computer Methods in Applied Mechanics and Engineering*, 384:113948, 2021.

[54] Tao Zeng, XianLin Dong, ChaoLiang Mao, ZhiYong Zhou, and Hong Yang. Effects of pore shape and porosity on the properties of porous pzt 95/5 ceramics. *Journal of the European Ceramic Society*, 27(4):2025–2029, 2007.

[55] Toshihiro Isobe, Takahiro Tomita, Yoshikazu Kameshima, Akira Nakajima, and Kiyoshi Okada. Preparation and properties of porous alumina ceramics with oriented cylindrical pores produced by an extrusion method. *Journal of the European Ceramic Society*, 26(6):957–960, 2006.

[56] Youngseuk Keehm, Tapan Mukerji, and Amos Nur. Permeability prediction from thin sections: 3d reconstruction and lattice-boltzmann flow simulation. *Geophysical Research Letters*, 31(4), 2004.

[57] Henk Kaarle Versteeg and Weeratunge Malalasekera. *An introduction to computational fluid dynamics: the finite volume method*. Pearson Education, 2007.

[58] Maasoud Kaviany. *Principles of heat transfer in porous media*. Springer Science & Business Media, 2012.

[59] Haibo Huang, Michael Sukop, and Xiyun Lu. Multiphase lattice boltzmann methods: Theory and application. 2015.

[60] Duo Zhang, K Papadikis, and Sai Gu. A lattice boltzmann study on the impact of the geometrical properties of porous media on the steady state relative permeabilities on two-phase immiscible flows. *Advances in Water Resources*, 95:61–79, 2016.

[61] Randall J LeVeque. *Finite difference methods for ordinary and partial differential equations: steady-state and time-dependent problems*. SIAM, 2007.

[62] Samuel J Cooper, Antonio Bertei, Paul R Shearing, JA Kilner, and Nigel P Brandon. Taufactor: An open-source application for calculating tortuosity factors from tomographic data. *SoftwareX*, 5:203–210, 2016.

[63] Jinlong Fu, Dunhui Xiao, Rui Fu, Chenfeng Li, Chuanhua Zhu, Rossella Arcucci, and Ionel M Navon. Physics-data combined machine learning for parametric reduced-order modelling of nonlinear dynamical systems in small-data regimes. *Computer Methods in Applied Mechanics and Engineering*, 404:115771, 2023.

[64] Hao Zhou, Guiyuan Mo, Feng Wu, Jiapei Zhao, Miao Rui, and Kefa Cen. Gpu implementation of lattice boltzmann method for flows with curved boundaries. *Computer Methods in Applied Mechanics and Engineering*, 225:65–73, 2012.

[65] Zhixiong Zeng, Jinlong Fu, YT Feng, and Min Wang. Revisiting the empirical particle-fluid coupling model used in dem-cfd by high-resolution dem-lbm-imb simulations: A 2d perspective. *International Journal for Numerical and Analytical Methods in Geomechanics*, 2023.